1999

Scanning tunneling microscopy studies of submonolayer and multilayer Ag films deposited on Ag(100)

Conrad Robert Stoldt
Iowa State University

INFORMATION TO USERS

This manuscript has been reproduced from the microfilm master. UMI films the text directly from the original or copy submitted. Thus, some thesis and dissertation copies are in typewriter face, while others may be from any type of computer printer.

The quality of this reproduction is dependent upon the quality of the copy submitted. Broken or indistinct print, colored or poor quality illustrations and photographs, print bleedthrough, substandard margins, and improper alignment can adversely affect reproduction.

In the unlikely event that the author did not send UMI a complete manuscript and there are missing pages, these will be noted. Also, if unauthorized copyright material had to be removed, a note will indicate the deletion.

Oversize materials (e.g., maps, drawings, charts) are reproduced by sectioning the original, beginning at the upper left-hand corner and continuing from left to right in equal sections with small overlaps.

Photographs included in the original manuscript have been reproduced xerographically in this copy. Higher quality 6" x 9" black and white photographic prints are available for any photographs or illustrations appearing in this copy for an additional charge. Contact UMI directly to order.

Bell & Howell Information and Learning
300 North Zeeb Road, Ann Arbor, MI 48106-1346 USA

UMI®
800-521-0600

Scanning tunneling microscopy studies of submonolayer and multilayer Ag films deposited on Ag(100)

by

Conrad Robert Stoldt

A dissertation submitted to the graduate faculty

in partial fulfillment of the requirements for the degree of

DOCTOR OF PHILOSOPHY

Major: Physical Chemistry

Major Professor: Patricia A. Thiel

Iowa State University

Ames, Iowa

1999

Bell & Howell Information and Learning Company
300 North Zeeb Road
P.O. Box 1346
Ann Arbor, MI 48106-1346

Graduate College

Iowa State University

This is to certify that the Doctoral dissertation of

Conrad Robert Stoldt

has met the dissertation requirements of Iowa State University

Signature was redacted for privacy.

Major Professor

Signature was redacted for privacy.

For the Major Program

Signature was redacted for privacy.

For the Graduate College

Dedicated to my family

TABLE OF CONTENTS

I. GENERAL INTRODUCTION

1. Thin films in current technology

The deposition, growth, and equilibration of thin films has been the subject of intense interest in recent decades [1]. This interest is motivated by the pivotal role that thin films play in current technology. Perhaps the most important industrial application of thin films is in integrated electronic circuits. Here, ordered silicon layers, insulating oxide layers, and metal contact layers are deposited, patterned, and etched sequentially, creating densely packed microelectronic devices, each smaller than 1 μm in size [2]. Thin films are also utilized in surface-catalyzed reactions. Thin film materials are inexpensive, compared to bulk materials, leading to their prevalence in industrial surface processes. For instance, the Union Carbide Corporation employs deposited thin Ag films, instead of bulk Ag, in the Ag-catalyzed epoxidation of ethylene [3]. Other industrially important applications for thin films include, but are not limited to, optical coatings, magnetic recording media, and corrosion preventative overlayers.

Recent advances in the control of thin film structures have fostered a great deal of interest in the fabrication of microdevices and nanostructures using epitaxial materials. With technology borrowed from the semiconductor industry, scientists are now able to manufacture micromachines with μm thickness and a lateral dimension of 10-500 μm [4]. Composed of deposited metal and semiconductor thin films, these electro-mechanical microdevices find use as sensors and actuators. Quantum dots [5] and nanowires [6] have also evolved from new advances in thin film growth methods. These nanostructures exhibit novel electronic and optical properties, but have proven difficult to consistently reproduce at

such small lateral sizes (~1-10 nm). Because this size regime is difficult to address with current lithography techniques, it is necessary to consider alternative fabrication methods. One such alternative is self-assembly from deposited metal and semiconductor atoms. This emerging field shows great potential, but requires a better understanding of film growth processes before becoming widely applicable.

The rapidly shrinking size of thin film devices places more stringent requirements on the quality and properties of epitaxial materials. As a consequence, device fabrication and stability must be controlled at the atomic level. During film growth, deposited atoms undergo fundamental interactions with each other and with the substrate. If one is to better understand the adhesion and growth of similar and dissimilar materials, these interactions must be of primary interest to the surface scientist. Elements of fabrication such as deposition flux, F, substrate temperature, T, and film thickness play crucial roles in determining film structure and associated film properties. Fortunately, these elements can be varied individually or simultaneously to allow the experimenter and theorist the opportunity to explore their impact on various thin film characteristics. As size decreases, stability becomes an important factor in determining the lifetime of both device shape and operation. Small structures inherently have high surface tension associated with the curvature of their edges [7,8]. Therefore, these "far-from-equilibrium" structures reshape in order to minimize the excess surface tension. The rate and extent of the equilibration process is pivotal in determining the structure's useful lifetime. By investigating the evolution of non-equilibrium structures produced by thin film deposition, surface scientists can gain fundamental insight into the kinetic processes governing atomic scale equilibration.

2. The Ag(100) surface

One can imagine that uncovering and cataloging the many kinetic processes active during film growth and equilibration could prove to be quite difficult, especially in heteroepitaxial systems. Therefore, a natural choice is to begin by investigating a less complex system, namely Ag(100) homoepitaxial thin films. We utilize the Ag(100) surface for many reasons: the Ag(100) surface does not reconstruct upon annealing to high T; Ag is relatively unreactive and remains contaminant free during sample preparation and analysis; and island diffusion and reshaping rates occur on time scales accessible with our experimental methods. The Ag(100) surface, as shown in Figure 1, has four-fold symmetry, with rows of atoms separated by rows of four-fold hollow (4FH) sites. In reality, a perfectly flat Ag(100) crystal is impossible to achieve. Instead, the Ag single crystal is slightly misaligned from the (100) direction, creating a series of monoatomic high steps separated by broad, flat terraces. Two step edge orientations predominate on this Ag(100) surface: the close-packed [011] orientation and the metastable [001] orientation. Both step edge orientations are illustrated in Figure 1.

3. Overview of submonolayer Ag/Ag(100) film growth and equilibration

The deposition, growth, and equilibration of submonolayer Ag films on Ag(100) can be described as follows. Film growth begins with the random deposition of Ag atoms onto the Ag(100) surface at a constant F (Figure 2a). Atoms impinge and irreversibly adsorb at the 4FH sites where atomic coordination is maximized with the substrate. At high T (> 200 K), adatoms diffuse or "hop" from one 4FH site to another (Figure 2b). Using Arrhenius Law, the hopping rate (h) for an adatom is defined as,

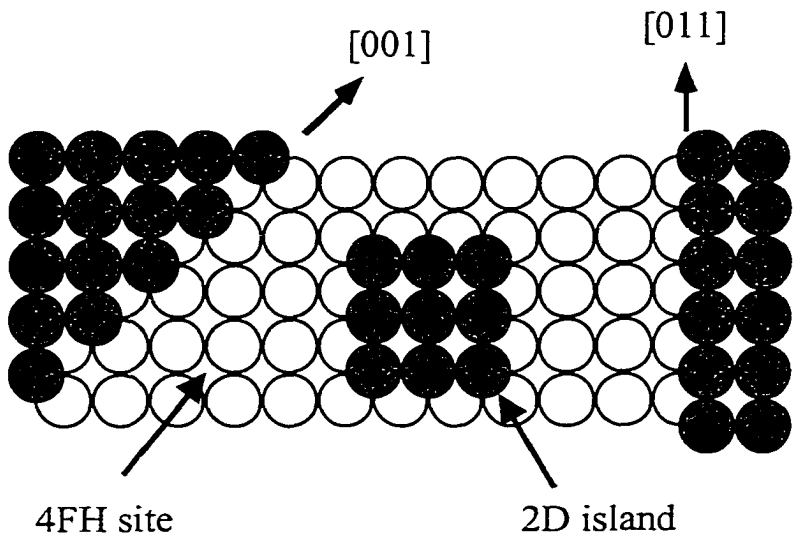

Figure 1. View of the (100) surface from above. Shaded circles are atoms in the upper layer. Non-shaded atoms lie in the lower layer. The close-packed [011] and metastable [001] step edge orientations are shown. Also illustrated is the square geometry of a small 2D island of adatoms.

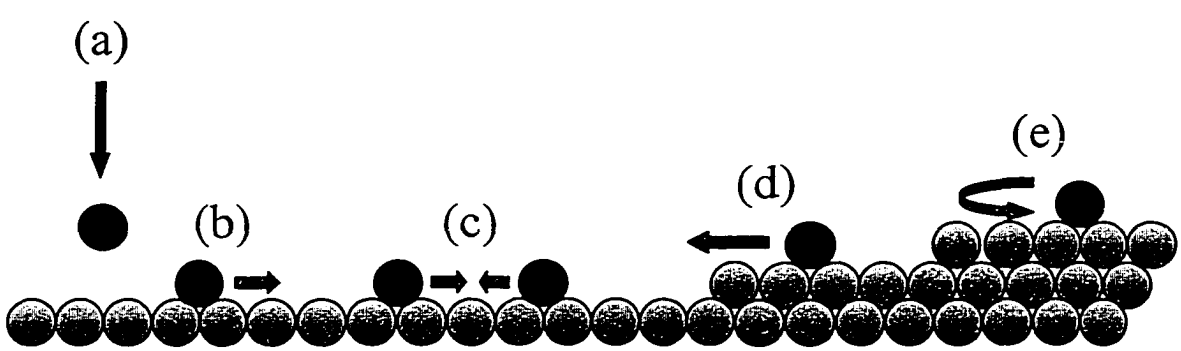

Figure 2. Adatom motion during deposition and growth on the (100) surface. Possible moves include: (a) deposition and adsorption at 4FH sites; (b) diffusion across terraces; (c) nucleation of 2D islands; (d) downward diffusion at step edges leading to smooth growth; and (e) reflection away from the downward step edge causing unstable, 3D growth.

$$h = \nu \cdot \exp(-\beta E_d), \qquad (1)$$

where ν is the vibrational attempt frequency, E_d is the adatom activation barrier to terrace diffusion, β is $(\kappa T)^{-1}$, and κ is Boltzmann's constant. Recent kinetic Monte Carlo (MC) simulations estimate that $h \sim 10^6\ s^{-1}$ at 295 K [9]. Experiments using high resolution low energy electron diffraction [10] and low energy ion scattering [11] yield $E_d \sim 0.40$ eV and $\nu \sim 10^{13}\ s^{-1}$.

Diffusing adatoms perform a random walk on the surface, interacting with surface atoms, with step edges, and with each other. Adatom-adatom collision results in the nucleation of two-dimensional (2D) islands at lower T (Figure 2c). At higher T, bond scission is operative and the rate of island nucleation is reduced. Early kinetic theories for submonolayer nucleation and growth [12,13] define a critical size, i, such that islands of i +1 atoms are stable. Simulations by Bartelt and Evans predict that for Ag/Ag(100), i = 1 below 380 K [14]. Therefore, dimers are stable and island nucleation is irreversible at $T \leq 380$ K.

The size distribution and density of islands created during deposition is dependent on a range of film growth processes [15-17], a key element of which is the rate of capture of diffusing adatoms by individual islands. In Chapter II, we present a brief analysis of the nature of diffusion-mediated capture of adatoms by near-square 2D islands during deposition on Ag(100). Larger islands have larger capture rates, which are quantified by performing MC simulations using experimental island distributions. For a more extensive discussion on this topic, see reference [18].

Small islands continue to grow in size as diffusing adatoms are incorporated at island edges. Because the Ag(100) surface has square symmetry, the equilibrium island shape is

also a square, as illustrated in Figure 1. This is verified by constructing a Wulff diagram for a square lattice [19]. The underlying substrate defines the equilibrium structure, and a Wulff diagram superimposed upon the lattice predicts the equilibrium crystal shape, or island shape, on the (100) surface. A 2D cut through a 3D Wulff plot for the (100) surface yields a square with edges oriented along the close-packed [011] direction at 0 K. 2D islands of Ag adatoms on Ag(100) do indeed assume a *near* square geometry above 0 K, as will be seen in subsequent chapters.

The average island density (N_{av}), which is experimentally measured after deposition, is defined as [12,13]

$$N_{av} \sim \left(\frac{F}{\nu}\right)^{\chi} \exp[\beta \cdot E], \tag{2}$$

where F is the deposition flux in monolayers (ML)/s and $\chi = \frac{i}{i+2}$. E is defined as

$$E = \chi\left(E_d + \frac{E_i}{i}\right), \tag{3}$$

where E_i is the binding energy of the critical cluster. E_i is equivalent to the number of pairs of atoms in an island multiplied by the Ag-Ag bond energy. In the following chapters, we consider only irreversible island formation, where i = 1. Therefore, equation (2) can now be simplified to yield

$$N_{av} \sim \left(\frac{F}{\nu}\right)^{1/3} \exp\left[\beta \frac{E_d}{3}\right] \sim \left(\frac{h}{F}\right)^{-1/3} \tag{4}$$

for irreversible island formation. Note that a choice of F and T determine the time it takes after deposition for N_{av} to be established. From N_{av}, we define an average island size, S_{av}, measured in atoms/island as

$$S_{av} = \left(\frac{\theta}{N_{av} \cdot a^2} \right), \qquad (5)$$

where θ is the film coverage in ML and a is the surface lattice constant for Ag (a = 2.89 Å). N_{av} is measured in islands/Å^2.

After deposition is complete, a nonequilibrium ensemble of 2D islands exists on the surface. The surface seeks to lower the overall surface tension by reducing the number of step edges present at the interface. This is achieved by decreasing the number of islands on the surface, commonly known as coarsening or ripening of the adlayer. Traditionally, it was believed that all homoepitaxial systems with 2D islands coarsen by a mechanism know as Ostwald Ripening [20]. In Ostwald Ripening, large islands grow at the expense of small ones. Small islands are unstable and evaporate; their atoms diffuse across terraces and are incorporated into larger islands. This mechanism results in coarsening, since the overall number of island edges on the surface is decreased. Recently, independent Scanning Tunneling Microscopy (STM) experiments have shown that both the Ag/Ag(100) and Cu/Cu(100) systems coarsen through an entirely different mechanism at 295 K [21-23]. Coarsening of the adlayer instead occurs through the diffusion and subsequent collision and coalescence of islands with other islands and step edges. This alternative coarsening mechanism, referred to as "Smoluchowski Ripening", is discussed extensively in Chapter III. Using STM, we investigate the post-deposition coarsening kinetics of distributions of Ag islands at 295 K. Coarsening behavior is analyzed with a mean-field rate equation, which reveals a strongly size dependent island diffusion coefficient.

Island coalescence plays an important role in the coarsening process as well. After a diffusing island collides with another island or step edge, a far-from-equilibrium

nanostructure is created on the surface. Vacancy islands are created by depositing between 0.7 and 0.9 ML of Ag [21]. Like adatom islands, vacancy islands have been shown to diffuse and coalesce with other vacancies and step edges on the surface. Often, 2D adatom and vacancy nanostructures have unusual geometries (see Figure 3). After collision, these nanostructures reshape in order to reduce the surface tension associated with their exposed edges. The rate at which reshaping occurs directly impacts the overall rate of coarsening after deposition. In Chapter IV, we analyze and quantify the reshaping rates of various initial nanostructure geometries using STM. Reshaping behavior is analyzed with lattice-gas model simulations to elucidate the underlying atomistic mass transport processes on the Ag(100) surface.

4. Overview of Ag/Ag(100) multilayer film growth

At equilibrium, homoepitaxial metal film growth is expected to proceed layer by layer since there is no mismatch between deposited atoms and substrate. In heteroepitaxial growth, where deposited material and substrate differ, 3D clustering of the deposited film usually occurs. Under realistic deposition conditions, multilayer film growth takes place far-from-equilibrium. Consequently, sequential filling of layers does not occur and "kinetic roughening" of the film results. The balance between F and T determines the degree of kinetic roughening during film growth. To simplify this picture, we fix the deposition flux and vary T. This allows us to investigate the T dependent morphologies that occur when kinetic processes become subdued or inactive during film growth.

On metal surfaces, an activation barrier to downward diffusion exists at step edges, often referred to as the Ehrlich-Schwoebel barrier [24,25]. On metal(111) surfaces, this

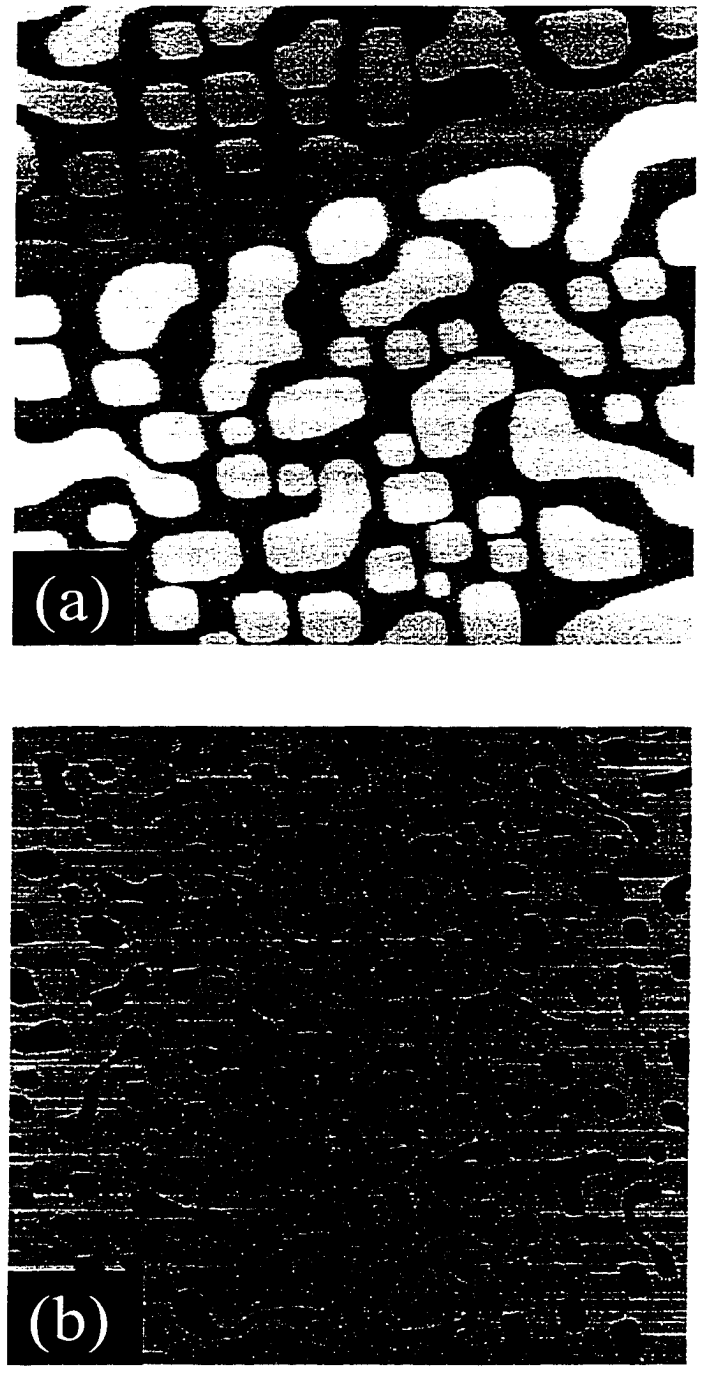

Figure 3. Large view STM images of (a) adatom nanostructures created by deposition 0.58 ML of Ag (image size = 2700 x 2700 Å); (b) vacancy nanostructures created by deposition of 0.77 ML of Ag (3000 x 3000 Å). The temperature is 298 K.

barrier is often high, resulting in inhibited downward transport of adatoms and rough Poisson-like growth for a broad range of T. Conversely, metal(100) surfaces generally have small step edge barriers, leading to relatively smooth multilayer growth. This is the case for Ag/Ag(100), which has a step edge barrier estimated to be 30 ± 5 meV [9]. Depending on the T, diffusing adatoms either have the energy to overcome the step edge barrier, travelling to a lower layer, or are reflected backwards, away from the step edge. Downward diffusion (Figure 2d) results in the filling of lower layers first and smooth film growth. Reflection away from the step edge leads (Figure 2e) to unstable growth and the formation of pyramidlike mounds exhibiting large roughness values. In Chapter V, we present the first STM images of mound formation in Ag/Ag(100) multilayer film growth.

Below 200 K, film roughness surprisingly decreases with decreasing T. The mechanism responsible for this phenomenon in metal(100) multilayer growth is referred to as "downward funneling". Our STM results confirm previous MC simulation results by Bartelt and Evans [26], and are the first experimental evidence of downward funneling in a metal(100) system. At T below 135 K, we show that downward funneling becomes inhibited, resulting in a dramatic increase in multilayer film roughness. In this T range, deposited atoms 'hit and stick' on the surface, a mechanism we call restricted downward funneling. With extremely limited adatom diffusion, voids are incorporated into the surface, enhancing kinetic roughening. In Chapter V, we present STM images of multilayer film growth below 135 K and approaching 0 K. To date, this represents the first detailed analysis of multilayer film growth at ultra-low T. The experimental results are analyzed and compared to our newly developed MC model for film growth in the diffusion limited regime.

Additionally, the results presented in Chapter V represent the first comprehensive STM investigation of multilayer film growth at multiple T.

Previous studies [27-33] have explored a number of universal scaling relationships in multilayer film growth. Relationships include film roughness, W, versus coverage having the form $W \sim \theta^{\beta}$, and the characteristic lateral length scale, L, versus time, t, having the form $L \sim t^{n}$. The exponents β and n are indicative of various growth mechanisms governing multilayer film morphology and evolution. The intent of developing such scaling laws is to find an exponent common to all multilayer film systems. In Chapter V, the values of β and n are determined at 230 K, the temperature where 25 ML Ag films grow the roughest.

5. The scanning tunneling microscope

In the aforementioned experiments, our principle surface analytical tool is the STM. Prior to the adoption of STM as an experimental tool, metal film growth has primarily been investigated using diffraction techniques such as low-energy electron diffraction (LEED), ion beam scattering, and reflection high-energy electron diffraction (RHEED). These techniques provide microscopic surface information that first must be derived and interpreted from reciprocal space diffraction patterns. STM images, on the other hand, can be directly examined, revealing real-space microscopic surface structures and growth characteristics. An excellent summary of STM operation and applications can be found in C. Julian Chen's book [34], "Introduction to Scanning Tunneling Microscopy."

We utilize the STM for many reasons. First, the STM (generally) provides better resolution than its nearest competitor, the atomic force microscope (AFM). Unlike AFM, STM requires electrical current flow between the substrate and microscope. Metal

substrates, being excellent conductors of electricity, are ideal for use with the STM. Second, the STM can operate in an ultra-high vacuum (2×10^{-10} to 4×10^{-11} Torr) environment, which is necessary when undertaking contaminant-free film growth experiments. Third, the STM produces 3D images of the surface's electron density contour. This yields information on vertical length scales, critical in characterizing multilayer film morphology. Finally, the STM provides sequential real-time images of surface dynamics, which is important when analyzing and modeling the mass transport processes of the adlayer.

It should be noted that the STM poses some experimental problems as well. STM resolution or sensitivity is highly dependent on the quality of the STM tip. In general, the exact structure of the STM tip is unknown. Therefore, the reproducibility of the STM tip is always a concern. Often, the tip structure changes from day to day, or during a single experiment. This makes it extremely difficult to perform reproducible experiments, and single experiments that last long periods of time. Typically, frequent calibration of the STM tip and tip preparation techniques, such as voltage and z-piezo pulses, are necessary to ensure accurate and reproducible results. Finally, when performing STM experiments below room T, the experimenter should be aware of additional complications with data acquisition. At reduced T, the metal substrate and STM tip contract, requiring both a finite time for equilibration and a recalibration of the vertical scale. Also, cold temperatures can adversely affect the tip-sample tunneling junction, causing drift and resolution loss in the scanning direction. Regardless of the many pitfalls of STM operation, nothing is more thought provoking than a good STM image.

6. Dissertation organization

This dissertation includes three published papers and a fourth that will be submitted for publication. The first paper: "Formation and relaxation of 2D island arrays in metal(100) homoepitaxy," appears in volume 59, issue 1-4 of *Progress in Surface Science* on pages 67-77, 1998. The second paper: "Smoluchowski ripening of Ag islands on Ag(100)," appears in volume 111, issue 11 of the *Journal of Chemical Physics* on pages 5157-5166, 1999. The third paper: "Evolution of far-from-equilibrium nanostructures formed by cluster-step and cluster-cluster coalescence in metal films" appears in volume 81, issue 14 of *Physical Review Letters* on pages 2950-2953, 1998. The fourth paper: "Complex temperature dependence in multilayer film growth," will be submitted to *Science*. Following the fourth paper are general conclusions and appendices that comprise a description of the experimental apparatus, the STM database, and other experimental results related to topics discussed in this dissertation.

References

1. See, e.g. Science, **273**, no. 5277 (1996).
2. C.R.M. Grovenor, *Microelectronic Materials*, 1 ed. (IOP Publishing Ltd., Bristol, 1989).
3. J.G. Serafin, A.C. Liu, and S.R. Seyedmonir, J. Molec. Catal. A **131**, 157 (1998).
4. R. Maboudian, Surf. Sci. Rep. **30**, 207 (1998).
5. See, e.g. MRS Bulletin, **23**, no. 2 (1998).
6. See, e.g. MRS Bulletin, **24**, no. 8 (1999).
7. J. Lapujoulade, Surf. Sci. Rep. **20**, 191 (1994).
8. E.D. Williams and N.C. Bartelt, *Handbook of Surface Science* **1**, 51 (1996).

9. C.-M. Zhang, M.C. Bartelt, J.-M. Wen, C.J. Jenks, J.W. Evans, and P.A. Thiel, J. Crys. Growth **174**, 851 (1997).

10. L. Bardotti, C.R. Stoldt, C.J. Jenks, M.C. Bartelt, J.W. Evans, and P.A. Thiel, Phys. Rev. B **57**, 12544 (1998).

11. M.H. Langelaar and D.O. Boerma, in *Surface Diffusion: Atomistic and Collective Processes*, Vol. **360**, edited by M.C. Tringedes (Plenum Press, New York, 1997), pp. 67-74.

12. J.A. Venables, Phil. Mag. **27**, 697 (1973).

13. R. Kaishev and S. Stoyanov, Curr. Topics Mater. Sci. **7**, 69 (1981).

14. M.C. Bartelt, L.S. Perkins, and J.W. Evans, Surf. Sci. **344**, L1193 (1995).

15. G. Rosenfeld, B. Poelsema, and G. Comsa, in *Growth and Properties of Ultrathin Epitaxial Layers*, Vol. **8**, edited by D.A. King and D.P. Woodruff (Elsevier, Amsterdam, 1998), Chap. 3.

16. R.Q. Hwang and M.C. Bartelt, Chem. Rev. **97**, 1063 (1997).

17. H. Brune, Surf. Sci. Rep. **31**, 121 (1998).

18. M.C. Bartelt, C.R. Stoldt, C.J. Jenks, P.A. Thiel, and J.W. Evans, Phys. Rev. B **59**, 3125 (1999).

19. E.D. Williams and N.C. Bartelt, Ultramicroscopy **31**, 36 (1989).

20. M. Zinke-Allmang, L.C. Feldman, and M.H. Grabow, Surf. Sci. Rep. **16**, 377 (1992).

21. J.-M. Wen, J.W. Evans, M.C. Bartelt, J.W. Burnett, and P.A. Thiel, Phys. Rev. Lett. **76**, 652 (1996).

22. W.W. Pai, A.K. Swan, Z. Zhang, and J.F. Wendelken, Phys. Rev. Lett. **79**, 3210 (1997).

23. J.-M. Wen, S.-L. Chang, J.W. Burnett, J.W. Evans, and P.A. Thiel, Phys. Rev. Lett. **73**, 2591 (1994).

24. G. Ehrlich and F.G. Hudda, J. Chem. Phys. **44**, 1039 (1966).

25. R.L. Schwoebel and E.J. Shipsey, J. Appl. Phys. **37**, 3682 (1966).

26. M.C. Bartelt and J.W. Evans, Surf. Sci. **423**, 189 (1999).

27. J.A. Stroscio, D.T. Pierce, M.D. Stiles, and A. Zangwill, Phys. Rev. Lett. **75**, 4246 (1995).

28. M.C. Bartelt and J.W. Evans, Phys. Rev. Lett. **75**, 4250 (1995).

29. W.C. Elliot, P.F. Miceli, T. Tse, and P.W. Stephens, Phys. Rev. B **54**, 17938 (1996).

30. K. Thurmer, R. Koch, M. Weber, and K.H. Rieder, Phys. Rev. Lett. **75**, 1767 (1995).

31. F. Tsui, J. Wellman, C. Uher, and R. Clarke, Phys. Rev. Lett. **76**, 3164 (1996).

32. J.E. Van Nostrand, S.J. Chey, M.-A. Hasan, D.G. Cahill, and J.E. Greene, Phys. Rev. Lett. **74**, 1127 (1995).

33. J.-K. Zuo and J.F. Wendelken, Phys. Rev. Lett. **78**, 2791 (1997).

34. C.J. Chen, *Introducion to Scanning Tunneling Microscopy*, 1 ed. (Oxford University Press, New York, 1993).

II. FORMATION AND RELAXATION OF 2D ISLAND ARRAYS IN METAL(100) HOMOEPITAXY

A paper published in Progress in Surface Science

C.R. Stoldt, A.M. Cadilhe, M.C. Bartelt, C.J. Jenks, P.A. Thiel, and J.W. Evans

Abstract

We present a comprehensive analysis of both the formation of near-square islands during deposition in submonolayer metal(100) homoepitaxy, as well as the subsequent post-deposition relaxation of these island arrays. We highlight recent fundamental advances in our understanding of the nucleation and growth of islands, as well as of the kinetic pathways controlling the relaxation of island arrays (including a study of the "collision" and coalescence of diffusing islands). Extensive Scanning Tunneling Microscopy results are presented for the Ag/Ag(100) system at 295K, and these are analyzed utilizing kinetic Monte Carlo simulations of appropriate lattice-gas models.

1. Introduction

The nucleation and growth of islands during submonolayer deposition is of broad technological importance [1]. Experimental data has been traditionally interpreted with mean-field rate equation theories which successfully describe the dependence of the mean island density, N_{av}, on deposition conditions, at least for low substrate temperature (T) where island formation is irreversible. However, it is now recognized that such theories fail to describe the characteristic shape of the island size distribution [2,3], or to correctly predict the transition to reversible island formation, with increasing T [3,4]. These and other recent fundamental insights and advances have often come from examining "simple" metal homoepitaxial growth systems, combining Scanning Tunneling Microscopy (STM) experiments [4,5] with kinetic Monte Carlo simulation studies of realistic nucleation models [3,6,7].

Another basic issue of interest is the post-deposition coarsening or equilibration of the adlayer, starting from the far-from-equilibrium island distribution created during deposition. The traditional expectation, at least for two-dimensional (2D) island distributions in homoepitaxial systems, is that coarsening is controlled by Ostwald ripening involving a diffusion-mediated transfer of adatoms from smaller to larger islands [8]. However, in some homoepitaxial systems, it has been observed instead that coarsening is dominated by the diffusion and subsequent coalescence of large islands [9,10]. This unexpected cluster diffusion [11,12] has prompted recent interest not just in its role in coarsening [9,10,13], but also in film smoothening [14], and in related issues of nanostructure evolution [15].

In this paper, we present an STM analysis of the nucleation and growth of near-square islands during submonolayer deposition in Ag/Ag(100) homoepitaxy at 295K (see

Sec.3). Accurate values for mean island densities at 295K (where island formation is irreversible) are utilized to extract a refined estimate of the terrace self-diffusion barrier for Ag on Ag(100). We also present an analysis of the diffusion-mediated capture of deposited adatoms by islands. We find a dramatic non-mean-field nature to the island size dependence of capture, which derives from a strong correlation between the size and separation of islands. This feature is related to the observed form of the island size distribution. In Sec.4, we also present STM studies of the post-deposition coarsening of Ag/Ag(100) adlayers with coverages between 0.06ML and 0.2ML at 295K. This coarsening process is dominated by diffusion and coalescence of large islands, and a suitably tailored and comprehensive study of its kinetics provides considerable insight into the size-dependence of island diffusion. Finally, we analyze in detail the process of restructuring of island shape following "collision" of pairs of islands, which is a key component of the coarsening process. A summary of our findings is provided in Sec.5.

2. Experimental details

Silver was deposited on a Ag(100) crystal from a resistively heated liquid-nitrogen-shrouded source in an ultra-high vacuum chamber with a base pressure of $6x10^{-11}$ to $2x10^{-10}$ Torr. The chamber is equipped with an Omicron room temperature STM system. The STM images of island distributions used in our analyses were obtained on broad terraces (at least 2000Å wide). Images were obtained under conditions of low resolution, since we were primarily interested in determining the number, positions, and sizes of large islands over broad terrace regions, rather than examining atomic-scale structure. We also deliberately sacrificed resolution in our studies of cluster diffusion, coalescence, and coarsening, so as to

minimize the interaction between the STM tip and the islands. The first STM image was obtained typically 20 to 50 minutes after deposition, after which we monitored the subsequent time-evolution of the island motion or island distributions every 10 to 15 minutes.

3. Nucleation and growth of islands during deposition

Below, θ denotes the coverage (in ML), $h=\nu\exp[-E_d/(k_BT)]$ denotes the rate for adatom hopping across the terrace to each adjacent site, and F denotes the deposition rate (in ML per unit time), so $\theta=Ft$. The density (per adsorption site on the fcc(100) surface) of diffusing adatoms is denoted by N_1, and of islands of s atoms is denoted by N_s. The rate of aggregation of diffusing atoms with islands of size s is denoted by $R_{agg}(s)=h\sigma_sN_1N_s$, where σ_s denotes the "capture number" for islands of size s. The rate of "direct capture" by deposition on top of or directly adjacent to an island of size s equals $F\kappa_sN_s$, where $\kappa_s\approx s+4\sqrt{s}$ for near-square islands. Then, for irreversible island formation, one has [1-3]

$$dN_1/dt \approx F(1-\theta)-2R_{agg}(1)-\sum_{s>1}R_{agg}(s), \text{ and } dN_s/dt \approx F(\kappa_{s-1}N_{s-1}-\kappa_sN_s)+R_{agg}(s-1)-R_{agg}(s), \quad (3.1)$$

with additional terms being required when island formation becomes reversible. Since most emphasis has been placed on the behavior of the mean island density, $N_{av}=\sum_{s>1}N_s$, usually (3.1) are reduced to

$$dN_1/dt \approx F(1-\theta)-h\sigma_{av}N_1N_{av}, \text{ and } dN_{av}/dt \approx h\sigma_1(N_1)^2, \text{ where } \sigma_{av}=\sum_{s>1}\sigma_sN_s/\sum_{s>1}N_s. \quad (3.2)$$

However, the island size distribution, N_s, which contains far more information than N_{av}, is also of great interest. If $s_{av} \approx \theta/N_{av}$ denotes the average island size, and if one assumes that the capture numbers have the scaling form $\sigma_s/\sigma_{av} \approx C(s/s_{av})$, independent of θ, then it follows that [2]

$$N_s \approx \theta(s_{av})^{-2} f(s/s_{av}), \text{ where } f(x) = f(0) \exp\{\int_0^x dy\, [(2\varpi-1)-dC(y)/dy]/[C(y)-\varpi y]\}, \qquad (3.3)$$

and $\varpi = d(\ln s_{av})/d(\ln t)$ is assumed constant. The key message to be obtained from (3.3) is that the form of the island size distribution is *controlled* by the dependence of adatom capture on island size.

A. Mean island density behavior for Ag/Ag(100) at 295 K

Data from previous STM studies [4] indicated that $N_{av} \approx 1.9\times10^{-3} F^{\chi}$ /site, with F between 0.002 and 0.1 ML/s (for a mean θ-value around 0.1ML). The scaling exponent, $\chi \approx 0.31$, describing variation of N_{av} with F, is slightly below the classic asymptotic value of 1/3 obtained from integration of (3.2) for irreversible island formation. Simulations for irreversible formation of square islands [7] reveal that $N_{av} \sim (F/h)^{\chi}$, with similar χ, and with a fairly weak dependence on θ around 0.1ML. Detailed comparison with experiment implies that $h \approx 3\times10^6$/s at 295K, so $E_d \approx 0.38$eV using $\nu \approx 10^{13}$/s [4]. However, the STM data included several cases with low θ around 0.03ML, where there can be significant coarsening of the adlayer before STM imaging (see Sec.4A), and with high θ of 0.2ML or above, a significant fraction of adjacent islands could have merged as a result of growth, and then restructured to

form a single islands before STM imaging (see Sec.4B). Both these effects (which we attempted to account for in previous analyses) can lead to underestimation of N_{av}.

Extensive new data (involving a total of about 650 islands) with F between 0.005 and 0.01 ML/s, and with coverages chosen closer to 0.1ML (see Figure 1) to minimize the above effects, suggests a slightly higher $N_{av} \approx 2.4\times10^{-3}$ F^{χ}/site, using $\chi\approx0.31$. This leads to a revised estimate of $E_d \approx 0.40$eV, using $\nu\approx10^{13}$/s. This can be compared with predictions from a recent high-resolution LEED study of island separation versus T [16], and a low-energy ion scattering study of the onset of diffusion [17].

B. Adatom capture and the island size distribution for Ag/Ag(100) at 295 K

As noted above, the dependence of diffusion-mediated adatom capture on island size controls the form of the island size distribution. We analyze this dependence for experimental island distributions of the type shown in Figure1 with $\theta\approx0.1$ ML. This is achieved by performing Monte Carlo simulations, using the *experimental* island distribution, of the random deposition of atoms, and of their subsequent surface diffusion and irreversible capture by islands [18]. From such simulations, we can quantify the rate at which various islands capture atoms, and thus obtain σ_s/σ_{av} versus s/s_{av} (Figure 2a). Results are roughly consistent with the form of the island size distribution in Figure1b (where some smaller islands were lost due to coarsening). The quasi-linear increase of σ_s with s for larger sizes is *qualitatively distinct* from the much slower increase predicted by mean-field theories (MFT), and derives from the feature ignored in MFT that larger islands have larger surrounding areas free of other islands [2,18]. This is confirmed by performing a standard Voronoi tessellation of the surface based on the island centers, i.e., points within a Voronoi cell (VC) associated

with a given island are closer to the center of that island than to the centers of other islands. If A_s is the area of the VC *not* covered by an island of size s, then Figure 2b shows that A_s/A_{av} versus s/s_{av} has a similar form to that for σ_s/σ_{av} (cf. Ref.18).

Of course, being a purely geometric construction, the VC's cannot precisely describe adatom capture. A somewhat better Voronoi-type tessellation would be based on the distance from island edges (rather than centers). However, an exact description necessarily incorporates the physics of diffusion-mediated capture by analyzing the equation $\partial/\partial t\, N_1 \approx F + D_{terr}\nabla^2 N_1 \approx 0$, for the quasi-steady-state density of deposited adatoms which diffuse to and are irreversibly captured at island edges (where one imposes the boundary condition $N_1=0$) [18]. Here, $D_{terr}=a^2h$ is the terrace diffusion coefficient, where a=2.89Å is the surface lattice constant. From the solution of this steady-state diffusion equation, each point on the surface is uniquely assigned to a specific island by following the flux lines from that point to an island. In this way, one can construct a tessellation of the surface into "diffusion cells" (DC's), the areas of which are in *exact proportion* to the capture rates for islands (from Gauss' theorem). Such a tessellation is shown in Fig.3 for a small portion of the experimental island distribution, and is compared with the corresponding Voronoi tessellation. Note, however, that diffusion-mediated capture is stochastic: the probability that an atom is captured by an island is not unity inside its DC and zero outside, but rather decreases smoothly to zero away from the island [18].

4. Post-Deposition Coarsening and Relaxation Processes

A. Coarsening via cluster diffusion and coalescence in Ag/Ag(100) adlayers at 295K

Previous studies have demonstrated that coarsening in Ag/Ag(100) adlayers at 295K for coverages between 0.05 and 0.35ML is typically dominated by diffusion and subsequent coalescence of 2D islands [9,10]. Island diffusion coefficients have been shown to decrease with size at least below $s \approx 350$ like $D(s) \approx D_0 s^{-\alpha}$, with $\alpha \approx 1.15$ [10]. Thus, the rate of coarsening should depend strongly on the mean island size, which controls the mean island diffusion coefficient, $D_{av} \approx D(s_{av})$, as well as on the coverage, which controls the typical distance, L_{edge}, between island edges (i.e., the distance islands must diffuse before coalescing). One has that $L_{edge} \approx (1-\theta^{1/2})L_{av}$, where $L_{av}=a(N_{av})^{-1/2}$ is the typical distance between island centers. Thus, the lifetime, τ, of a typical island corresponds to the time to diffuse a distance L_{edge}, so it follows from Einstein's relation that $(L_{edge})^2 \approx 2\times 4 D_{av}\tau$, the factor of two arising since the "target" island is also diffusing. Then, the mean-field rate equation for N_{av} becomes

$$dN_{av}/dt \approx -N_{av}/\tau \approx -8a^{-2} D_0 \theta^{-\alpha}(1-\theta^{1/2})^{-2} (N_{av})^{2+\alpha}, \quad \text{so } N_{av} \approx [(N_0)^{-1-\alpha} + (1+\alpha)At]^{-1/(1+\alpha)}, \quad (4.1)$$

where $A=8a^{-2} D_0 \theta^{-\alpha}(1-\theta^{1/2})^{-2}$, and N_0 is the initial island density [9]. The latter result in (4.1) recovers the relation obtained in Ref. 13 for the exponent for asymptotic temporal scaling in terms of α.

An effective method to assess the size dependence of cluster diffusivity is to perform tailored studies of coarsening with varying initial island size for roughly fixed separation

(i.e., deposit various coverages at roughly fixed F) [19]. Such data for the coarsening kinetics is shown in Figure 4 for three coverages, 0.06, 0.16, and 0.21ML, corresponding to initial island sizes of 140, 340, and 495 atoms, respectively. The kinetics slows dramatically with increasing island size, indicating that the effect on coarsening of the reduction of the island diffusion coefficient dominates the opposite effect of closer island edges. In fact, the experimental data can be reasonably fit choosing $\alpha \approx 1.5$ and $D_0 \approx 1.75$ Å^2/s. A more detailed analysis is postponed for a simulation study, where we can account for spatial correlations in the island distribution [1,7] which are ignored in the above mean-field treatment.

B. Coalescence dynamics for individual pairs of "colliding" clusters in Ag/Ag(100) at 295 K

We consider the dynamics of coalescence of pairs of islands which collide either corner-to-corner (see Figure 5a) or side-to-side (see Figure 5b). These 2D sintering processes are of interest not only as an integral component of the overall coarsening process, but also for at least two other reasons. First, the restructuring of such far-from-equilibrium nanostructures can provide considerable insight into the underlying mass transport processes at step edges [15]. Second, islands also collide as a result of their growth during deposition, and the restructuring of these configurations influences the subsequent multilayer growth process if it is significant on the time-scale of deposition [20]. We analyze this behavior with simulations of a "perimeter diffusion" model, wherein restructuring occurs as a result of atoms hopping along the step edge without detaching with various energy barriers shown in Figure 6a.

For two roughly equal sized clusters colliding corner-to-corner (Figure 5a), we consider the growth of the width of the connecting meniscus-like neck. Simulations reveal a rapid initial increase, followed by a more sustained quasi-linear growth (Figure 6b,c), with rate varying inversely with combined island area (Figure 6d). Experimental behavior is matched by simulations with a barrier for diffusion along straight [110] step edges of E_e=0.20eV, and an effective nearest-neighbor interaction of J_{eff}=0.275eV.

5. Summary

We have presented analyses of both the formation and relaxation of arrays of 2D islands created by deposition of Ag on the Ag(100) surface at 295K. Our application of a combination of STM experiments, together with kinetic Monte Carlo simulations, leads to fundamental advances in our understanding of these processes, together with a determination of key system parameters. The basic phenomena and concepts discussed here will certainly apply more generally to metal(100) homoepitaxy, and often be relevant for a variety of other thin film systems.

Acknowledgements

This work was supported by NSF Grant CHE-9700592 (CRS, AMC, CJJ, PAT, JWE), and performed in part at Ames Laboratory, which is operated for the USDOE by Iowa State University under Contract No. W-7405-Eng-82. It was also supported by the Office of Basic Energy Sciences, Division of Materials Sciences, of the USDOE under Contract No. DE-AC04-94AL85000 (MCB).

References

1. S. Stoyanov and K. Kashchiev, Curr. Topics Mater. Sci. 7, 69 (1981); J.A. Venables, Philos. Mag. **27**, 697 (1973).
2. M.C. Bartelt and J.W. Evans, Phys. Rev. **B 54**, R17359 (1996); MRS Proc. 440, 247 (1997).
3. J.W. Evans and M.C. Bartelt, in *Morphological Organization in Epitaxial Growth and Removal*, Z. Zhang and M.G. Lagally, (Eds.), World Scientific, Singapore (1998).
4. C.-M. Zhang, M.C. Bartelt, J.-M. Wen, C.J. Jenks, J.W. Evans, and P.A. Thiel, Surf. Sci. **406**, 178 (1998); J. Crystal Growth 174, 851 (1997).
5. H. Brune, Surf. Sci. Rep. **31**, 121 (1998).
6. J.W. Evans and M.C. Bartelt, J. Vac. Sci. Technol. **A 12**, 1800 (1994); C. Ratsch, A. Zangwill, P. Smilauer, and D.D. Vvedensky, Phys. Rev. Lett. **72**, 3194 (1994); J. Amar and F. Family, Phys. Rev. Lett. **74**, 2066 (1995).
7. M.C. Bartelt and J.W. Evans, Surf. Sci. **298**, 421 (1993); MRS Proc. **312**, 255 (1993).
8. M. Zinke-Allmang, L.C. Feldman, and M.H. Grabow, Surf. Sci. Rep. **16**, 377 (1992).
9. J.-M. Wen, J.W. Evans, M.C. Bartelt, J.W. Burnett, and P.A. Thiel, Phys. Rev. Lett. **76**, 652 (1996).
10. W.W. Pai, A.K. Swan, Z. Zhang, and J.F. Wendelken, Phys. Rev. Lett. **79**, 3210 (1997).
11. J.-M. Wen, S.-L. Chang, J.W. Burnett, J.W. Evans, and P.A. Thiel, Phys. Rev. Lett. **73**, 2591 (1994).
12. K. Morgenstern, G. Rosenfeld, B. Poelsema, and G. Comsa, Phys. Rev. Lett. **74**, 2058 (1995).
13. D.S. Sholl and R.T. Skodje, Physica A **231**, 631 (1996); P. Meakin, *ibid*, **165**, 1 (1990).

14. M. Giesen, G. Schulze Icking-Konert, and H. Ibach, Phys. Rev. Lett. **80**, 552 (1998).

15. C.R. Stoldt, A.M. Cadilhe, C.J. Jenks, J.-M. Wen, J.W. Evans, and P.A. Thiel, Phys. Rev. Lett., submitted (1998); P.A. Thiel and J.W. Evans, in *Morphological Organization in Epitaxial Growth and Removal*, Z. Zhang and M.G. Lagally, (Eds.), World Scientific, Singapore (1998).

16. L. Bardotti, C.R. Stoldt, C.J. Jenks, M.C. Bartelt, J.W. Evans, and P.A. Thiel, Phys. Rev. **B 57**, 12544 (1998).

17. M.H. Langelaar, M. Breeman, and D.O. Boerma, Surf. Sci. **352/354**, 597 (1996).

18. M.C. Bartelt, A.K. Schmid, J.W. Evans, and R.Q. Hwang, Phys. Rev. Lett., in press (1998); M.C. Bartelt, J.W. Evans, A.K. Schmid, and R.Q. Hwang, MRS Proc. **528** (1998).

19. L. Bardotti, M.C. Bartelt, C.J. Jenks, C.R. Stoldt, J.-M. Wen, C.-M. Zhang, P.A. Thiel, and J.W. Evans, Langmuir **14**, 1487 (1998).

20. M.C. Bartelt and J.W. Evans, Phys. Rev. Lett. **75**, 4250 (1995).

Figure Captions

1. (a) 2D Ag island array (θ=0.12ML, F=0.005ML/s); (b) normalized island size distribution, f.
2. (a) σ_s/σ_{av} versus s/s_{av}; (b) A_s/A_{av} versus s/s_{av}, for the experimental island arrays (symbols). Solid lines are obtained from simulations of a canonical model for irreversible island formation (cf. Ref.7).
3. Contours of equal adatom density from solution of the steady-state equation for deposition, diffusion, and capture (thin lines); diffusion cells (thick lines); Voronoi cells (dashed lines).
4. N_{av}/N_0 vs. t for θ = 0.06, 0.16, 0.21ML, and N_0=4.2×10^{-4}, 4.7×10^{-4}, 4.2×10^{-4}/site, respectively.
5. (a) Corner-to-corner; (b) side-to-side coalescence of clusters. Image size is always 35×35 nm^2.
6. (a) Edge hopping processes and associated activation barriers; (b) simulated configurations for corner-to-corner coalescence of two 20×20 clusters; (c) time-dependence of the neck width for various cluster sizes; (d) rate of growth of the neck width vs. inverse area of the combined cluster.

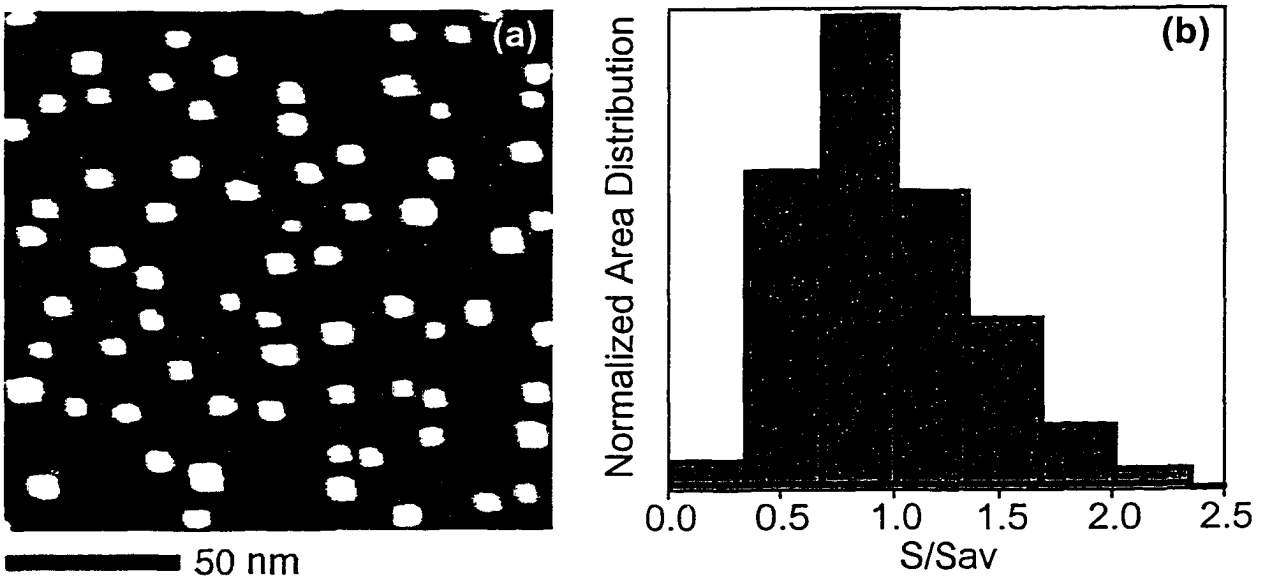

Figure 1

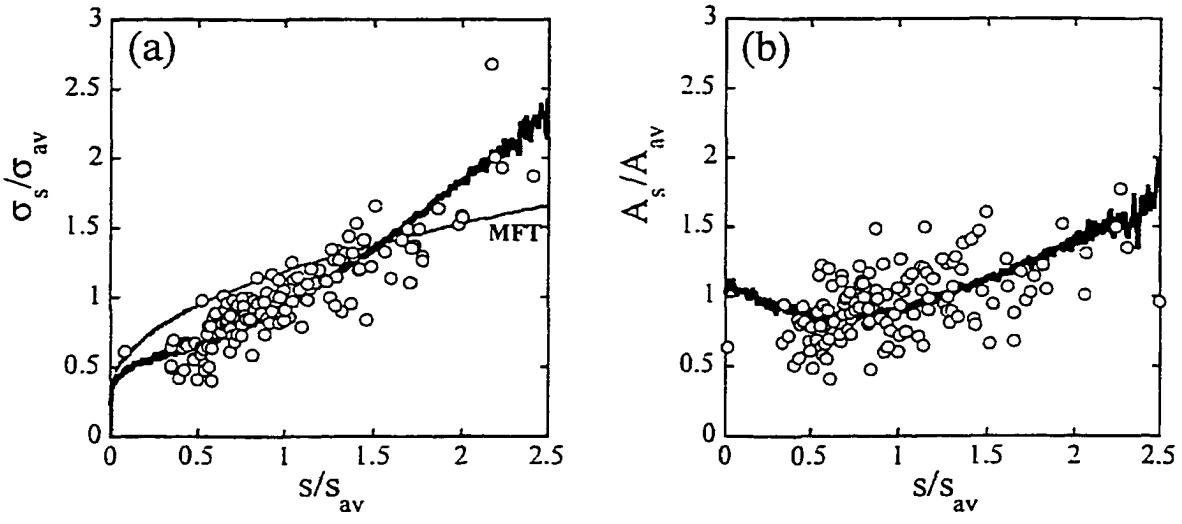

Figure 2

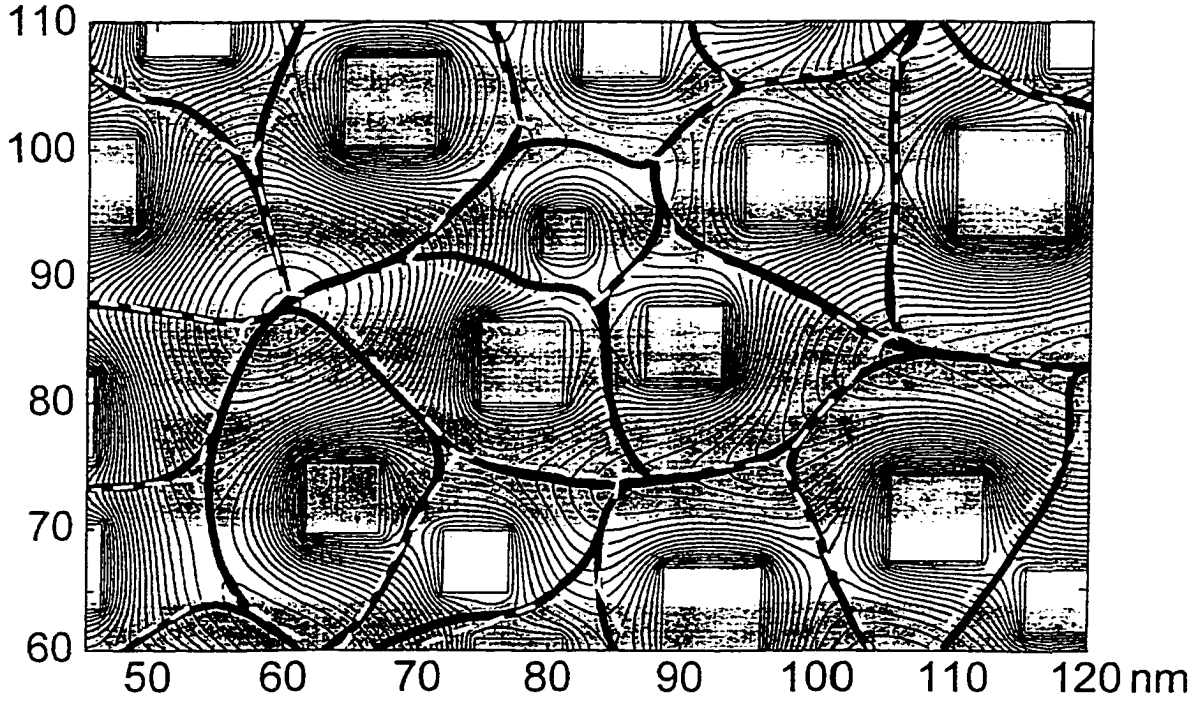

Figure 3

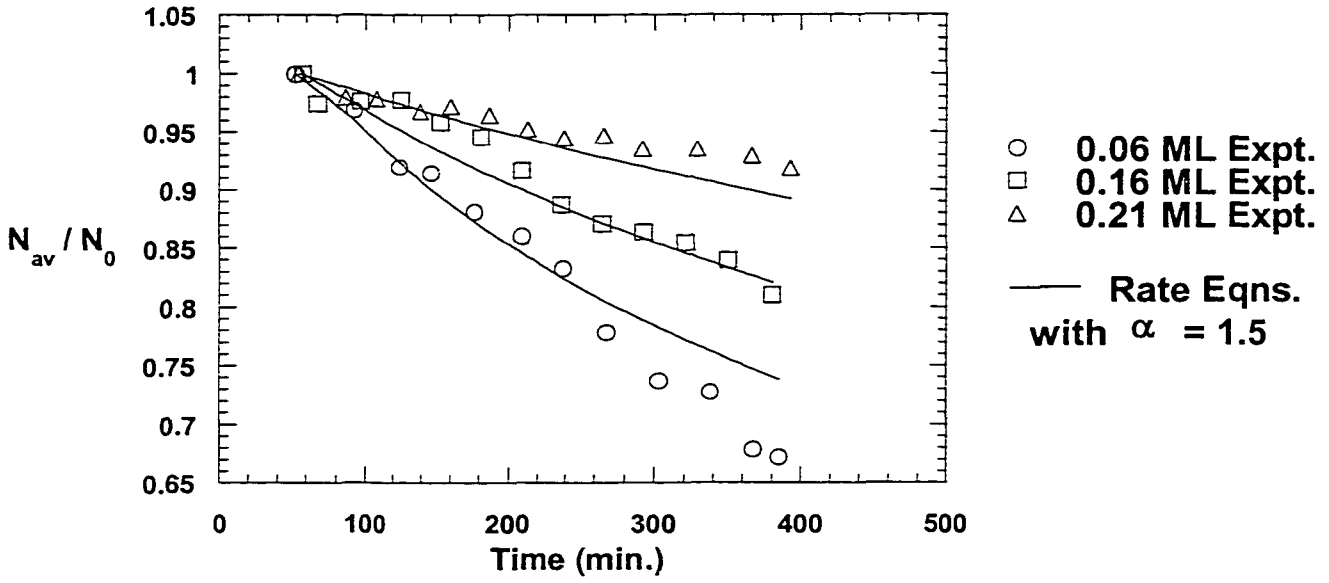
1.05
1
0.95
0.9
0.85
0.8
0.75
0.7
0.65
N_av / N_0
0
100
200
300
400
500
Time (min.)
0.06 ML Expt.
0.16 ML Expt.
0.21 ML Expt.
Rate Eqns.
with α = 1.5

Figure 4

(a)

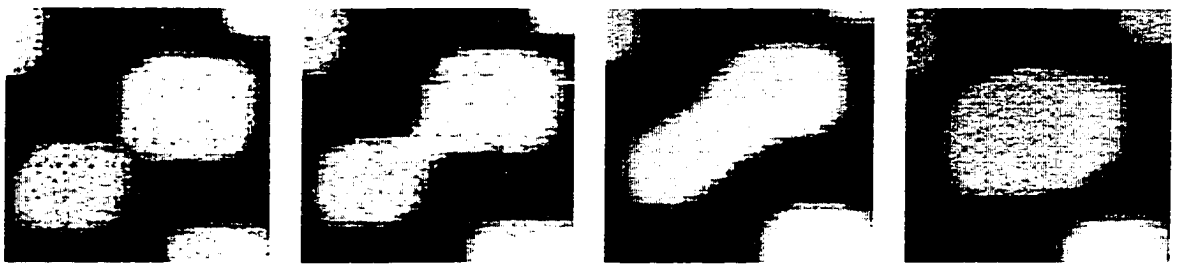

0 min. 2 min. 29 min. 150 min.

(b)

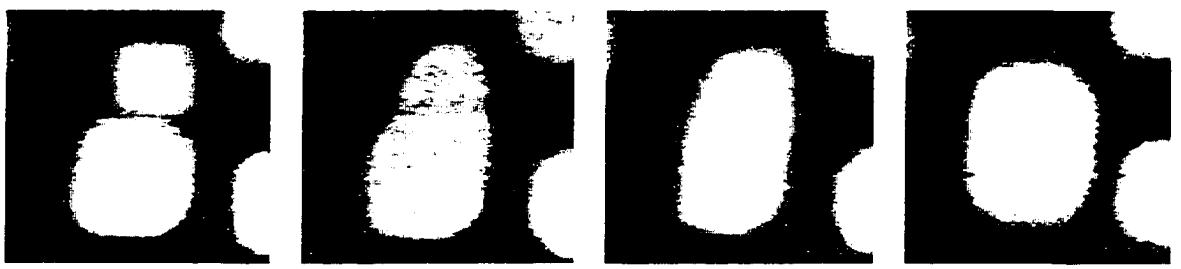

0 min. 5 min. 22 min. 127 min.

Figure 5

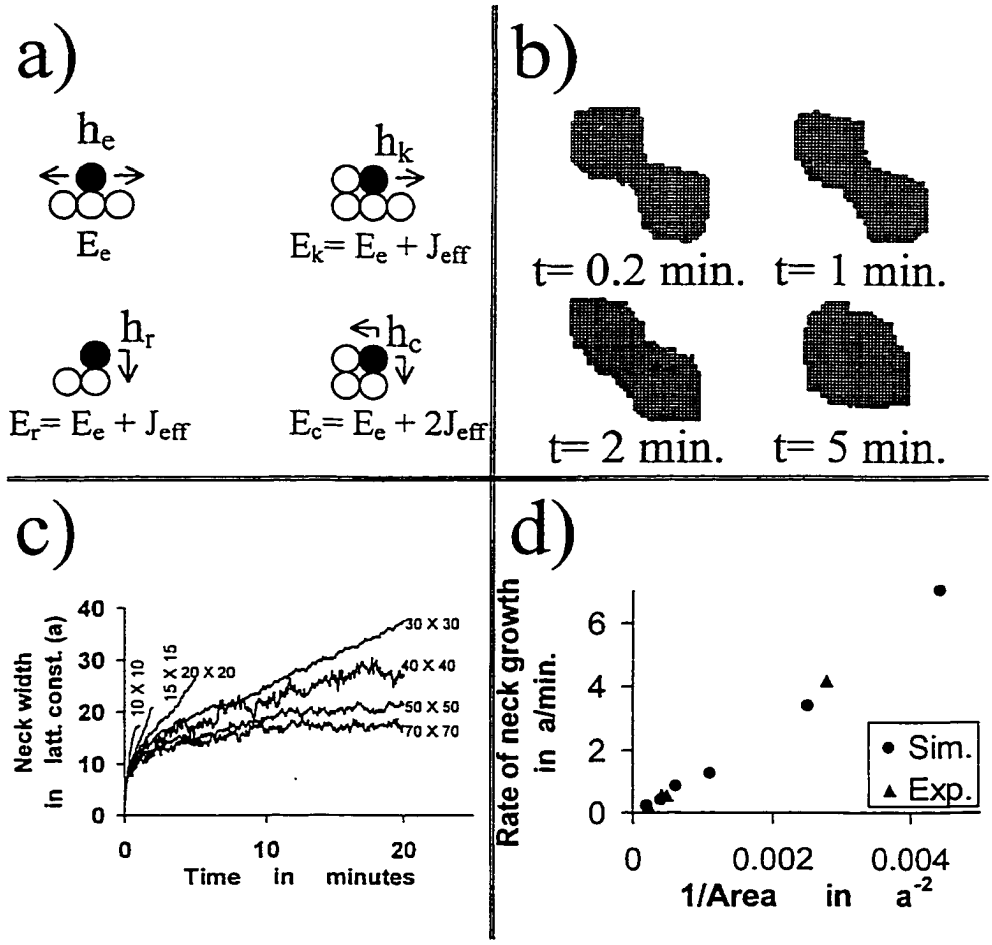
a)
h_e
E_e
h_k
$E_k = E_e + J_{eff}$
h_r
$E_r = E_e + J_{eff}$
h_c
$E_c = E_e + 2J_{eff}$
b)
t= 0.2 min.
t= 1 min.
t= 2 min.
t= 5 min.
c)
Neck width in latt. const. (a)
Time in minutes
10 X 10
15 X 15
20 X 20
30 X 30
40 X 40
50 X 50
70 X 70
d)
Rate of neck growth in a/min.
1/Area in a^{-2}
Sim.
Exp.

Figure 6

III. SMOLUCHOWSKI RIPENING OF Ag ISLANDS ON Ag(100)

A paper reprinted with permission from THE JOURNAL OF CHEMICAL PHYSICS

C.R. Stoldt, A.M. Cadilhe, C.J. Jenks, J.W. Evans, and P.A. Thiel

PACS Numbers: 68.35.Fx, 82.20.Mj, 61.16.Ch

Abstract

Using scanning tunneling microscopy, we study the post-deposition coarsening of distributions of large, two-dimensional Ag islands on a perfect Ag(100) surface at 295K. The coarsening process is dominated by diffusion, and subsequent collision and coalescence of these islands. To obtain a comprehensive characterization of the coarsening kinetics, we perform tailored families of experiments, systematically varying the initial value of the average island size by adjusting the amount of Ag deposited (up to 0.25 ML). Results unambiguously indicate a strong decrease in island diffusivity with increasing island size. An estimate of the size scaling exponent follows from a mean-field Smoluchowski rate equation analysis of experimental data. These rate equations also predict a rapid depletion in the initial population of smaller islands. This leads to narrowing of the size distribution scaling function from its initial form, which is determined by the process of island nucleation and growth during deposition. However, for later times, a steady increase in the width of this scaling function is predicted, consistent with observed behavior. Finally, we examine the evolution

of Ag adlayers on a strained Ag(100) surface, and find significantly enhanced rates for island diffusion and coarsening.

1. Introduction

The number of applications for epitaxial materials continues to increase, and with this increase has come more stringent requirements on the quality and properties of these materials. As a result, atomic-level control in the fabrication of nanostructures, and assessment of their stability, is becoming crucial. Surface science continues to confront this issue through studies of fundamental processes in the growth and equilibration of epitaxial films [1]. To gain the most complete picture of these processes, a common strategy is to begin by investigating less complex systems, one particularly simple example of which is metal(100) homoepitaxial thin films.

In the submonolayer regime, the key processes controlling homoepitaxial film growth and equilibration can be described as follows. During film growth, atoms adsorb irreversibly on the surface, then rapidly diffuse, colliding with each other to nucleate two-dimensional (2d) islands. Islands continue to grow in size as additional adatoms are incorporated. The ensemble of islands thus created on the surface constitutes a far-from-equilibrium state of the adlayer [2]. This state then undergoes post-deposition equilibration, during which the excess surface free energy associated with island edges is reduced by decreasing the number or density of islands, and thus increasing their mean size (that is by coarsening or "ripening" of the island distribution).

Traditionally, "Ostwald ripening" was believed to constitute the dominant kinetic pathway or mechanism for adlayer coarsening in homoepitaxial systems with 2d islands [3].

During Ostwald ripening, diffusion-mediated mass transport of adatoms (or vacancies) across terraces between 2d islands allows for the growth of large islands at the expense of small ones. Scanning Tunneling Microscopy (STM) studies have revealed that indeed Ostwald ripening dominates the coarsening of island distributions for Ag/Ag(111) at 295K [4], for Cu/Cu(111) between 300K and 355K [5], and for Cu/Cu(100) at 343K [6]. In constrast, for Ag/Ag(100) and Cu/Cu(100) at 295K, STM studies revealed that adlayer coarsening is typically dominated by the diffusion, and subsequent collision and coalescence of "large" 2d islands [7,8]. It is natural to describe this alternative coarsening mechanism as "Smoluchowski ripening", recalling the long-established and extensive use of Smoluchowski rate equations [9] to analyze various other diffusion-mediated coagulation processes.

The latter observations of Smoluchowski ripening on metal surfaces have motivated considerable interest in the process of diffusion of large 2d islands or clusters in its own right. Most studies to date have explored scaling relationships for the island diffusion coefficient, D(s), versus island size, s, of the form $D(s) \approx D^* s^{-\alpha}$ (for sufficiently large s). Here, 's' denotes the number of atoms in the island, and D* is a temperature-dependent prefactor which reflects the magnitude of the diffusion coefficient for islands of a few atoms. An early mean-field-type theoretical treatment [10] provided a direct (but over simplistic) relationship between the exponent, 'α', and the dominant atomistic mechanism underlying diffusion: $\alpha=3/2$ for "perimeter diffusion" (PD) involving hopping of atoms along the island periphery; $\alpha=1$ for "terrace diffusion" (TD) involving correlated detachment and reattachment of atoms from the island perimeter (or diffusion of vacancies through the island); and $\alpha=1/2$ for "evaporation and condensation" (EC) involving uncorrelated detachment and attachment of atoms. However, pioneering simulation studies by Voter [11],

as well as more recent and extensive simulation studies [12, 13], and also recent theoretical [14] and experimental [8] investigations, have shown that these simple fractional values for α are not always realized. Nonetheless, it seems that larger exponent values still indicate that PD is dominant.

There is also a long history of analyses of processes involving coarsening of distributions of clusters on surfaces. Most have focussed on Ostwald ripening [3], although there were a number of studies particularly in the 1970's of Smoluchowski ripening for three-dimensional (3d) islands [15-17]. The latter, which are more closely related to this study, included analysis of not just mean island size, but also the evolution of the island size distribution including such features as its dispersion [15,16]. Related theoretical analyses employed mean-field Smoluchowski rate equations. More recent theoretical studies of Smoluchowski ripening have focused on arrays of 2d islands (motivated by the experimental studies mentioned above [7,8]), often employing kinetic Monte Carlo simulation to analyze suitable models, and thus avoiding the limitations of mean-field treatments [18-20]. The most sophisticated such studies [20] incorporate simulation results for island diffusivity, and have been generalized to allow for a competing Ostwald ripening pathway. One particularly simple but important relationship for Smoluchowski ripening follows from the mean-field analysis (and is confirmed in simulation studies): the temporal scaling exponent, β, for the mean island size, $s_{av} \sim t^{\beta}$, is related to the size-scaling exponent, α, for cluster diffusivity by $\beta = 1/(1+\alpha)$ [19]. Here, s_{av} is measured in numbers of atoms, and the temporal scaling applies only for "long" times.

In this paper, we consider exclusively coarsening of 2d islands in the Ag/Ag(100) system at 295K combining STM experiments with theoretical modeling. As noted above,

diffusion of large 2d near-square clusters has been observed in this system, and coarsening is dominated by Smoluchowski ripening [7]. A comprehensive analysis of cluster diffusion, monitoring the relative position of roughly equal sized pairs of clusters, yielded an estimate of α=1.14 with a chi-squared uncertainty of $\pm$0.05 [8]. However, there is considerable scatter in the experimental data, an intrinsically large uncertainty in values for diffusivity, and additional uncertainty in island sizes. Thus, the uncertainty in α may be larger, and values up to at least 1.3 plausibly fit the data. Interestingly, observation of a single coarsening run over an extended period of about 28 hours yielded an estimate of $\beta \approx 0.466$ [8], consistent with α=1.14. In this study, the rate of evaporation of adatoms from island edges was estimated independently and found to be sufficiently small that associated TD and EC mechanisms must be inoperative [8]. Thus, cluster diffusion was assumed to be dominated by PD in this system.

Another possibility was suggested in a recent simulation study of the diffusion of large 2d Cu clusters on Cu(100), which revealed a crossover with increasing island size from PD to TD mediated by vacancy diffusion through the cluster [13]. It was suggested that this behavior may be generally applicable for other metal(100) homoepitaxial systems, including Ag/Ag(100) [13]. However, it has been noted that the relative dominance of PD versus vacancy TD will be strongly sensitive to the magnitude of rate for vacancy diffusion relative to the various PD rates, as well as to the cluster size [21]. From this perspective, the study in Ref.[13] might be somewhat biased towards vacancy TD, as it incorporates a relatively low choice of activation barrier for vacancy diffusion [22-25]. Thus, there is still some uncertainty as to the mechanism for diffusion of large Ag clusters on Ag(100).

A key experimental challenge in coalescence studies is to obtain sufficiently good statistics for a detailed quantitative analysis. Difficulty arises due to the intrinsically high fluctuations or "noise" in the underlying cluster diffusion and coalescence processes. (In this respect, Monte Carlo studies have an advantage in that noise is more easily assessed and reduced by extensive simulation trials.) One typically neglected problem in experimental studies of the coarsening kinetics is that there are strong temporal correlations, i.e., the number of islands always strictly decreases with time. A smooth decrease in island density with time hides the fact that a quite different behavior could result from repeating the experiment from the same initial island distribution (so, e.g., it is difficult to assess the uncertainty in β from a single run). Another problems is that despite the recent interest in island diffusion and coarsening in metal homoepitaxial systems, only limited and selective studies of coarsening kinetics have been performed. Consequently, in this study, we address these shortcomings by performing tailored families of experiments, wherein we systematically varying the initial value of the average island size by adjusting the amount of Ag deposited (up to 0.25 ML). The entire family of curves for average coarsening kinetics should vary smoothly (in fact, analytically), so deviations in experimental data from this trend reflect noise. Also, there is sufficient information in the variation of entire family of curves that one can directly assess size dependence of diffusivity. We also make use of a Smoluchowski rate equation to quantitatively relate the decrease in the mean island density to island diffusivity.

Analysis of island size distribution, and its evolution, is of course much more statistically demanding than analysis of just the mean size. The most extensive previous studies for Smoluchowski ripening have been for 3d islands, and have typically identified the

natural increase in the mean size and associated broadening of the distribution during coarsening [3]. Related theoretical studies invariably focus on the asymptotic evolution and shape selection [26]. However, little effort has been made to assess the evolution in the intrinsic shape of island size distribution, as characterized by the appropriate scaling function. This transient behavior is of particular experimental relevance, as the asymptotic regime may not be accessible, and as it allows assessment of the extent of the early changes occurring before first STM observation. The latter is crucial in order to correctly surmise the "initial" post-deposition form of the size distribution for appropriate comparison with predictions of nucleation theory. (In fact, the form produced by the nucleation and growth process has only been understood very recently [27-29].) Thus, we characterize the initial shape evolution in this paper. To this end, we find it instructive to consider the variance of the scaling function (as opposed to the dispersion of the size distribution considered previously [15,16], the behavior of which is driven by the increase in the mean island size). Reasonably accurate experimental determination of this variance is viable, in contrast to the full shape of the size distribution.

Finally, we report experimental data revealing that surface strain can have a strong influence on island diffusion and thus Smoluchowski ripening on large terraces. This observation implies that some care should be taken in interpreting data for nominally unstrained surfaces.

2. Experimental details

Scanning Tunneling Microscopy has become the technique of choice for performing studies of island diffusion and adlayer coarsening in homoepitaxial metal adlayers. Its

inherent ability to image the metal surface with unparalleled resolution, and to record real-time changes in ensembles of 2d islands, makes it the ideal tool for investigating such processes. Our experimental data are acquired using an Omicron room temperature STM housed in an ultra-high vacuum chamber with a base pressure of 6×10^{-11} to 2×10^{-10} Torr. The Ag(100) substrate is prepared through cycles of Ar ion sputtering and annealing to 700 K. Contamination is minimal, based inspection of STM images and Auger spectroscopy. Silver is deposited on the substrate from a home-built, liquid-nitrogen-shrouded source, with the substrate temperature always held at 295 K. However, the deposition flux and deposition time can be adjusted to yield various coverages, and initial values for the mean island density or size.

After deposition, the first STM image is typically obtained within 25-50 minutes. It should be noted that the island density can be significantly reduced (by 5-15%) due to coarsening before this image is taken [30, 31]. The subsequent time evolution of the system, discussed in detail in the following sections, is monitored at a rate of 2-3 min/frame. The tunneling parameters employed (voltage = 0.7-1.5 V, current = 0.3-0.5 nA) have been determined previously to minimize the STM tip-surface interaction [7, 31]. The island density and size distribution data in our analysis are obtained from the central portions of terraces wider than 1500 Å in order to minimize the effects of step edges on island distributions.

3. Experimental results and discussion

In the following discussion, a=2.89Å denotes the surface lattice constant for Ag(100). Also, θ denotes the time-invariant post-deposition coverage (measured in monolayers), N_{av}

denotes the mean island density (measured in units of islands per adsorption site), L_{av} denotes the mean separation of island centers (measured in units of distance), and s_{av} denotes the mean island size (measured in units of atoms). These quantities are simply related by

$$L_{av}=a(N_{av})^{-1/2} \text{ and } s_{av}=\theta/N_{av}. \quad (1)$$

Thus, N_{av} will decrease in time during coarsening, and both L_{av} and s_{av} will increase in time, from their "initial" post-deposition values, which we denote by N_{av}^0, L_{av}^0, and s_{av}^0, respectively.

Typical sequences of STM images from two coarsening experiments are shown in Figs. 1a and 1b for initial values, s_{av}^0, of the mean island sizes of 60 and 510 atoms, respectively. Both the general nature of evolution in these images, and the specific feature that ripening is more rapid in the case with smaller s_{av}^0, are consistent with the traditional perception that Ostwald ripening should dominate coarsening in metal homoepitaxial systems [3]. However, a detailed examination of the coarsening process, utilizing all of the experimental images, reveals that the contribution from Ostwald ripening is negligible, lying within the experimental noise. Instead, island diffusion, and subsequent collision and coalescence (or Smoluchowski ripening) produce essentially all of the coarsening [7]. This conclusion is supported by independent studies for Ag/Ag(100) and Cu/Cu(100) at 295K [8].

In order to most effectively assess whether island diffusion rates are size-dependent, it is natural to create initial island distributions with roughly fixed island separations, L_{av}^0, and varying mean island sizes, s_{av}^0. This is readily achieved noting a basic result from nucleation theory that the mean island density, N_{av}^0, is largely independent of coverage between 0.05 and

0.25ML [2]. More specifically, for irreversible island formation at fixed temperature, one has [2]

$$N_{av}^0 \sim F^{1/3}, \text{ so } L_{av}^0 \sim a\, F^{-1/6}, \text{ and } s_{av}^0 \sim \theta\, F^{-1/3}. \quad (2)$$

This regime applies for Ag deposition on Ag(100) below about 310K, and thus at 295K [31]. Thus, by depositing various amounts of Ag, at approximately constant flux, F, we maintain a roughly constant N_{av}^0 and L_{av}^0, but can control the initial value of the mean island size, s_{av}^0. Specifically, s_{av}^0 varies roughly linearly with submonolayer coverage, θ, which in turn varies linearly with deposition time (for fixed F). In fact, by depositing between 0.01 ML and 0.25 ML, we can readily access a broad range of initial values for s_{av}^0.

Each ensemble of islands thus created was then monitored at roughly periodic intervals to determine the decrease of island density, N_{av}, with time, thus generating a coarsening curve characteristic of a specific value of s_{av}^0 (and of L_{av}^0). We plot families of such coarsening curves for varying s_{av}^0 (and roughly fixed L_{av}^0). In fact, Fig.2 shows three such families of curves (each family corresponding to a different value of F or L_{av}^0). The values of s_{av}^0, θ, N_{av}^0, and the actual initial number of islands observed, are summarized in Table 1.

Based on the trends within each family of coarsening curves in Fig. 2, we can immediately assess the variation of cluster diffusion coefficient, D(s), with size, s. By increasing s_{av}^0 (or θ), with fixed island center-center separation, L_{av}^0, the average separation between island edges is reduced, shortening the distance for islands to diffuse before coalescing. Thus, if D(s) were completely independent of s, the rate of coarsening should

actually increase with increasing s_{av}^0 (or θ), due to this shorter distance. In contrast, the opposite behavior is observed in Fig.2, where the coarsening rate decreases strongly with increasing s_{av}^0 (or θ). This can only be ascribed to a strong decrease in D(s) with increasing s. A more detailed analysis is presented in Sec. 4.

Finally, we mention one significant issue pertinent for modeling data particularly for smaller island sizes or coverages. STM tip scans may have a tendency to disproportionately magnify small features [32]. This can result in an overestimation of θ (and thus s_{av}^0), so it is important to try to correct for this effect before detailed comparison between theory and experiment. Of course, the inherently low resolution in STM caused by scanning large surface areas also produces larger uncertainty in θ and s_{av}^0 values for small adlayer coverages.

4. Theoretical analysis of evolution of the mean island density

The Smoluchowski rate equation approach [9], first advanced over 80 years ago, has been employed widely to describe the kinetics of coagulation, aggregation, reaction, and coarsening. As noted in Sec.1, this approach has been applied extensively to analyze the Smoluchowski ripening of 3d clusters on surfaces [15-17], but relatively little work has been done for 2d clusters. Thus, in this section, we present these standard mean-field rate equations, together with a minor refinement, in order to analyze the coarsening data of Sec.3.

Extending the notation introduced in Sec.3, we let N_s denote the density (per adsorption site) of islands of s atoms. Then, the mean-field Smoluchowski rate equations for these island densities have the generic form [9,15-19]

$$d/dt\ N_s = \tfrac{1}{2} \Sigma_{s'+s''=s} K(s',s'')N_{s'}N_{s''} - \Sigma_{s'} K(s,s')N_sN_{s'}, \qquad (3)$$

where K(s,s′) describes the rate of collisions between islands of size s and s′. Assuming that this rate has the form K(s,s′)=k(s)+k(s′), these equations can be contracted to an equation for the mean island density (per adsorption site), $N_{av}=\sum_s N_s$, of the form

$$d/dt\ N_{av} = -N_{av}/\tau, \text{ where } 1/\tau=\sum_s k(s)N_s=k_{av}N_{av}. \quad (4)$$

Here, τ corresponds to the typical lifetime of a diffusing island, and we have defined $k_{av}=\sum_s k(s)N_s/N_{av}$. The equation (4) is not closed (without further approximation), but rather represents the first in a hierarchy of equations for various moments of N_s (see Appendix A). Usually, k(s) is related to the diffusion coefficient for islands of size s, often invoking a detailed analysis of diffusion-mediated aggregation [9,33]. Then τ is inversely proportional to some mean diffusivity. Given the limitations of even sophisticated mean-field treatments of capture (see below), we prefer a simpler treatment which accounts for the often neglected (but important) feature that the linear dimension of coalescing islands is often a significant fraction of their separation. By so doing, we directly reveal the strong dependence of τ on θ, in addition to its dependence on the mean island diffusivity.

First, we observe that for 2d near-square islands, the mean separation between island edges (see Fig. 3) has the form $L_{edge}=(1-c\theta^{1/2})L_{av}$, where the geometrical factor, *c*, is determined by the details of the island distribution. It will be approximated by unity in our analysis below. Then, for a diffusing island to reach another island, we note that it typically

needs only travel a net distance L_{edge}, rather than the longer distance L_{av}. Thus, according to the Einstein relation, one has [7, 34, 35]

$$(L_{edge})^2 \approx 2(4D_{av})\tau. \tag{5}$$

Here, D_{av} denotes the mean island diffusivity, and the factor of two outside the parentheses arises since both islands involved the coalescence event are mobile. Solving this equation for the lifetime, τ, and substituting into (4), reveals that [34]

$$d/dt\ N_{av} = -8a^{-2}\ D_{av}(1-c\theta^{1/2})^{-2}\ (N_{av})^2. \tag{6}$$

A simple correspondence with the Smoluchowski equations (3) can be made by assigning $k(s) = 8D(s)\ (1-c\theta^{1/2})^{-2}$. However, a more precise form for k(s) would be based on an estimate the typical separation between the edge of an island size s and other those of islands (rather than just on the average, L_{edge}). Below, we adopt the further approximation

$$D_{av} = \Sigma_s D(s) N_s/N_{av} \approx D(s_{av}), \text{ where } s_{av}=\Sigma_s s N_s/N_{av}=\theta/N_{av}, \tag{7}$$

which becomes precise for narrow island size distributions. See Appendix A. From the assumed form, $D(s)\approx D^* s^{-\alpha}$, one obtains $D_{av}\approx D^*\theta^{\alpha}(N_{av})^{-\alpha}$. Then, substitution into (6) and integration yields

$$N_{av} \approx [(N_{av}^0)^{-1/\beta} + (1+\alpha)At]^{-\beta}, \text{ where } \beta=1/(1+\alpha), \quad (8)$$

and where $A=8(a)^{-2} D^*\theta^{-\alpha}(1-\theta^{1/2})^{-2}$, and again N_{av}^0 is the initial island density.

The experimental coarsening data presented in Sec. 3 can be reasonably fit by choosing $\alpha \approx 1.5$, with a corresponding $D^* \approx 50$ Å^2/s. The coarsening curves generated from (8) for these parameters are shown as solid lines in Figs. 2a-2c. Fig. 4 provides some assessment of the sensitivity of the fit by showing rate equation curves with α-values of 1.0, 1.25, 1.5, and 1.75, for one family of experimental coarsening curves. Fits for α=1.5 and 1.75 are comparable, but the smaller value of 1.25 seems to produce too weak a s-dependence to D(s) to describe the dramatic increase in coarsening rates upon decreasing s_{av}^0 to 40 atoms. However, the uncertainties in estimates of θ and s_{av}^0 are greatest for small cluster sizes. Also, as noted in Sec.1, the magnitude of the noise or uncertainty in the experimental data is hidden by strong temporal correlations in N_{av} in each coarsening experiment. Thus, the uncertainty in our estimate of $\alpha \approx 1.5$ is substantial, perhaps ± 0.25. This α-value is larger than the previously reported value of α=1.14 (and a corresponding D^*=18.5 Å^2/s) [8], but there is no clear inconsistency given the substantial uncertainties (see also Sec.1). We plan a subsequent analysis of these coarsening processes using Monte Carlo simulation, which will elucidate the intrinsic noise in the coarsening process, and thus allow better assessment of uncertainties in α-estimates. These simulations will also account for spatial correlations in the island distribution, which are ignored in the rate equation approach.

Finally, we comment briefly on our previous modeling of coarsening data. In Ref.[7], we neglected the size dependence of island diffusivity, but accounted for coverage

dependence of the lifetime τ. A reasonable fit to coarsening data was obtained because we only compared situations with similar mean island size (and thus D_{av}), but differing mean island separations.

5. Evolution of the shape of the island size distribution

It is common to express the island densities, N_s, in the scaled form [27,28]

$$N_s \approx \theta(s_{av})^{-2} f(s/s_{av}, t), \text{ for large } s_{av}. \quad (9)$$

Then, the scaling function 'f' describing the shape of the island size distribution satisfies

$$\int_0^\infty f(x, t)dx = \int_0^\infty x f(x, t)dx = 1, \text{ and } \int_0^\infty (x-1)^2 f(x, t)dx = \sigma(t)^2, \quad (10)$$

where $\sigma(t)$ denotes the standard deviation or width of the scaling function. The first two normalization conditions follow from the constraints $\Sigma_s N_s = N_{av}$, and $\Sigma_s s N_s = \theta$. In (10), we also use $x = s/s_{av}$ to denote the natural scaled island size variable.

There have been extensive studies [2] of the "initial" shape of the size distribution, $f(x,0)=f_0(x)$, produced by the nucleation and growth process, although its form was only recently understood [28,29]. Such distributions have a significant population of small islands (compared with the average size) [27], particularly for irreversible island formation, which applies for the Ag/Ag(100) system at room temperature [31]. Separate theoretical studies of coarsening have demonstrated that a distinct shape, determined by the details of the coarsening process, is selected for long times [3, 19, 26]. In particular, for Smoluchowski

ripening, this selected shape is determined by the size-dependence of cluster diffusivity. See Ref.s [19], [26], and Appendix B. Here, we are naturally interested in the evolution of f(x,t) from the form $f_0(x)$ induced by cluster diffusion and coalescence with the observed strongly size-dependent cluster diffusivity. Intuitively, one expects a rapid initial depletion of these smaller islands, due to their higher mobility, and thus an associated rapid and significant change in shape of f(x,t).

From the experimental perspective, there are two key challenges with analyzing the island size distribution. First, as noted in Sec.2, a significant period of time elapses after deposition ceases and before the first STM image is acquired, so any rapid changes may not be seen. Second, as noted in Sec.1, typically one cannot obtain sufficient data to reduce the intrinsic statistical noise to the extent needed to allow accurate determination of the shape of the island size distribution (or its evolution). Because of the latter, our experimental analysis focused on evolution of the width, $\sigma(t)$, of the scaling function.

To quantify the evolution of the island size distribution, and of $\sigma(t)$ in particular, we integrate the Smoluchowski equations (3) for the island densities, N_s, and from the results extract f(x,t). For a more direct analysis of the evolution of f(x, t), see Appendix B. We assign cluster collision rates consistent with cluster diffusivity $D(s)=D^*s^{-\alpha}$, choosing $\alpha=1.5$ and $D^*=50$ Å^2/s, and select an initial size distribution based on nucleation theory, as now discussed in more detail. For Ag/Ag(100), experimental data suggests that the formation of near-square islands is effectively irreversibly at 295K, and that cluster diffusion does not play a significant role during this process [31]. Simulations appropriate for this scenario show that $f_0(x)$ has the characteristic monomodal form: it has a maximum value at $x=x_{max}\approx1.1$ of $f_0(x_{max})\approx0.78$, decreasing to a minimum of about 0.30 as x decreases to $x\approx0.02$ (before

increasing slightly at x=0), and a variance of $\sigma^2 \approx 0.24$ [29]. With this initial distribution, we find that the variance, $\sigma(t)^2$, at first decreases slightly (to just below 0.2) before slowly increasing. However, we shall see below that experimentally observed minimum values for σ^2 are around 0.1, but with a large uncertainty (cf. Appendix C). This suggests some modification of the above choice of initial size distribution is appropriate. Previous studies have shown that some mobility of dimers and other small clusters during deposition can significantly modify this distribution, without affecting the scaling of N_{av} [36]. Specifically, small cluster mobility reduces $f_0(0)$, increases $f_0(x_{max})$, and produces more rapid decay of f(x) for x above x_{max}, thus reducing σ^2. (The onset of reversibility during island nucleation has the same effect [31, 37].) Such a modified choice of $f_0(x)$ with $\sigma^2 \approx 0.18$ is used below.

Fig.5a shows the results for the evolution of f(x,t), choosing an initial $f_0(x)$ as described above, and choosing θ=0.16ML and $N_{av}^0 = 5.1 \times 10^{-4}$/site (so $s_{av}^0 \approx 315$ atoms). We find significant evolution of f(x,t) from the initial form $f_0(x)$ in the first several minutes, with a somewhat narrower form depleted of small islands being achieved after only about ½-¾ hour. This latter form (highlighted in Fig.6a at 50 min.) is consistent with experimental data in Fig.5b obtained from analysis of STM images of island distributions (with 420 islands) on broad terraces with the same θ and N_{av}^0 obtained about 50 min. after deposition. An important conclusion from this study is that caution is necessary when comparing experimental island distributions measured "just after" deposition with theoretical predictions from nucleation theory [31]. Even in the "short" time required to obtain the first STM image, there can be significant evolution of the size distribution away from its "initial" post-deposition form.

Finally, in Fig.6, we compare experimental observations and corresponding rate equation predictions for the evolution of $\sigma(t)^2$ for three cases with F=0.003ML/s and θ=0.02, 0.05, and 0.08 ML (see Table Ic). The initial values for s_{av}^0 in the rate equation analysis are chosen as 55, 138, 268 atoms to recover reported experimental values at the initial observation time (of around 50 min.) of 60, 140, and 270 atoms, respectively. The rate equation predictions reveal an initial decrease from our chosen initial value of σ^2=0.18 to about 0.16, followed by a much slower increase. Given the substantial experimental uncertainties in estimating σ^2-values (see Appendix C), overall behavior is consistent with experimental observations (where an initial decrease presumably occurs before the first data point). The consistent slow increase in σ^2 for longer times reflects the gradual development of a "slowly decaying tail" on the distribution for larger x. This feature is characteristic of the asymptotic long-time form, $f_\infty(x)$, which has a substantially larger value of σ^2 than does $f_0(x)$. See Appendix B.

6. Surface strain and its influence on island diffusion and coarsening

The effect of surface strain on adsorbate diffusion and crystal growth continues to attract interest. Long ago, Bauer developed thermodynamic criteria for near-equilibrium heteroepitaxial film configurations, where strain occurs due to lattice mismatch [38]. However, more recent studies have considered situations where heteroepitaxial growth is dominated by kinetics [39]. In homoepitaxial systems, one inevitably encounters surface strain induced by defects and dislocations. Can the resulting stresses affect the kinetics of surface processes? In Fig.7, an STM image is shown following the deposition of 0.18 ML of

Ag on Ag(100) producing a distribution of large islands with $s_{av}^0 \approx 490$ atoms. In the center of the image is a strained, oblong-shaped region, with a maximum height of approximately 0.7 Å above the unstrained portion of the surface. The origin of the strain is undetermined. The coarsening kinetics for islands around this region is displayed in Fig.8. The central observation is that the coarsening is much faster than predicted by mean-field rate equations of Sec.3 with $\alpha=1.5$ and $D^*=50$ Å^2/s (dashed line in Fig.8). The observed coarsening can be reasonably described by rate equations using $D^*=250$ Å^2/s, keeping $\alpha=1.5$ (solid line in Fig.8). This five-fold increase in D^* produces a corresponding increase in the coarsening rate of roughly five times. Note that the choice $\alpha=1.5$ is maintained for simplicity, but a different size dependence from unstrained adlayers is quite plausible (see below). One conclusion from these observations is that undetected strain could "corrupt" experimental estimation of D(s) versus s for nominally unstrained surfaces.

To elucidate our observations, we apply some ideas developed in recent analyses of the role of surface strain in heteroepitaxial film growth. In studies of the formation of strained islands, it was proposed that the barrier for adatom detachment or dissociation from island edges, E_{DISS}, should be reduced by the strain energy per adatom of the island [40]. This strain energy/atom increases with island size. We relate these observations to PD-mediated cluster diffusion as follows. Barriers for detachment, E_{DISS}, are roughly given by the sum of the terrace diffusion barrier, E_d, plus a multiple of an effective nearest-neighbor interaction, J; those for perimeter diffusion, E_{PD}, are the sum of the barrier for diffusion along close-packed <110> edges, $E_e \approx E_d/2$, plus a multiple of J [22, 23]. A strain-induced reduction of E_{DISS} suggests a reduction in J, and thus a reduction in E_{PD} (although other behavior is possible [41]). As a result, rates for cluster diffusion via the PD mechanism should be

enhanced by strain, the effect being greater for large islands as in Fig.7 where $s_{av}^{0} \approx 490$ atoms. Considering the possibility that cluster diffusion is mediated by TD of vacancies, tensile strain (as expected here) tends to raise barriers for adatom diffusion [41,42]. However, it might lower barriers for vacancy diffusion, which would be needed for consistency with observed behavior.

The general scenario of strain-enhanced cluster diffusion is also supported by a study of the motion of large vacancy clusters on Cu(111) surfaces, which found enhanced cluster diffusion upon addition of submonolayer amounts of Co [43]. This effect was attributed to the creation of local strain fields resulting from the substitution of Co with the top layer of Cu. Finally, we note that other novel mechanisms have been proposed to mediate the diffusion of strained heteroepitaxial islands, e.g., the formation of misfit dislocations separating portions of islands with adatoms occupying fcc and hcp sites on (111) surfaces [44]. Novel mechanisms may also operate for strained island diffusion on (100) surfaces.

7. Conclusions

In summary, we have performed tailored experiments of the coarsening of 2d Ag island distributions on Ag(100). Coarsening is dominated by cluster diffusion and coalescence at 295 K. The coarsening kinetics show that the island diffusion coefficients must decrease strongly with size for clusters with tens to hundreds of atoms. Analyzing experimental data with an appropriate mean-field rate equation suggests a size scaling exponent of $\alpha \approx 1.5$. Given this characterization of cluster diffusivity, we also use mean-field rate equations to assess the rapid initial evolution in the shape of the island size distribution, and the evolution over longer times of the width of the scaling function for the size

distribution. Since these rate equations do not account for spatial correlations in the island distribution, or elucidate the intrinsic noise or uncertainty in the experimental data for coarsening of finite ensembles of a few hundred (or less) islands, we plan to assess these issues in a future kinetic Monte Carlo simulation study. Finally, we analyzed coarsening behavior on a strained surface, showing that surface stresses can result in significantly increased cluster diffusion and coarsening rates.

Acknowledgements

We would like to thank Maria Bartelt for useful discussions. This work was supported by NSF Grant CHE-9700592, and by the Institute of Physical Research and Technology (IPRT) at Iowa State University. It was performed at Ames Laboratory, which is operated for the US Department of Energy by Iowa State University under Contract No. W-7405-Eng-82.

Appendix A: Evolution of the moments of the island size distribution

Statistical limitations often preclude reliable experimental determination of the island size distribution, $N_s \approx \theta(s_{av})^2 f(s/s_{av}, t)$ versus s. Thus, it is natural to instead consider the moments

$$M_j = \Sigma_s s^j N_s \approx N_{av}(s_{av})^j \int_0^\infty dx\, x^j f(x,t), \qquad (11)$$

or related quantities. For example, one has $N_{av}=M_0$, $\theta=M_1$, and $\sigma^2 = M_2 M_0 (M_1)^{-2} - 1$. For this reason, we note that a direct description of the evolution of the M_j is possible. Assuming that $K(s,s')=k(s)+k(s')$ and defining $K_j=\Sigma_s s^j k(s) N_s$, from the Smoluchowski equations (3) one has

$$d/dt\ M_0 = -K_0M_0,\quad d/dt\ M_1 = 0,\quad d/dt\ M_2 = 2K_1M_1,$$

$$d/dt\ M_3 = 4K_3M_1+6K_2M_2+4K_1M_3,\ldots \qquad (12)$$

An analysis might proceed by expressing the K_j in terms of the moments, M_j, or in terms of related quantities. To this end, a Taylor expansion, $k(s)=k(s_{av})+(s-s_{av})k'(s_{av})+$, can be utilized to obtain, e.g., $k_{av} = K_0/M_0 = k(s_{av}) + \frac{1}{2}(s_{av})^2\,\sigma^2\,k''(s_{av}) +\ldots$ See Ref.[16] for a different approach.

In the lowest-order approximation, $k_{av}\approx k(s_{av})$ [cf. (8)], one obtains $d/dt\ M_0 \approx -k(s_{av})(M_0)^2$. One can readily develop more accurate higher-order approximations for narrow island size distributions (with $\sigma<<1$), but this task is more difficult for broader distributions. For the choice $k(s) \propto s^{-\alpha}$, the error in the lowest-order approximation for large s_{av} can be assessed from the relation $k_{av}=R(t)\cdot k(s_{av})$, where $R(t) = \int_0^\infty x^{-\alpha} f(x, t)dx$. In the notation of Sec.4, this corresponds to $D_{av}=R(t)\cdot D(s_{av})$, and an approximation is used in (8) and (9) replacing R by unity.

Appendix B: Evolution of the Shape of the Island Size Distribution

In the regime of large s_{av}, one can reasonably replace the discrete variable, s, by a continuous variable, and rewrite the Smoluchowski equations with $K(s,s')=k(s)+k(s')$ as

$$d/dt\ N_s \approx \tfrac{1}{2}\int_0^s ds'[k(s')+k(s-s')]N_{s'}N_{s-s'} - \int_0^\infty ds'[k(s)+k(s')]N_sN_{s'}. \qquad (13)$$

We assume that $k(s) \propto s^{-\alpha}$, and thus can write $k(s)=k(s_{av})(s/s_{av})^{-\alpha}$. Using $N_s \approx \theta(s_{av})^2 f(s/s_{av}, t)$, we extract from (13) an equation for f in terms of the variable $x=s/s_{av}$. The LHS of (13) becomes

$$d/dt\, N_s = \theta\, (s_{av})^{-2}[(d/dt(\ln s_{av})(-2f - x \cdot f_x) + f_t\,], \tag{14}$$

and we note that

$$d/dt(\ln s_{av}) = -d/dt(\ln N_{av}) = R \cdot k(s_{av}) N_{av} = 1/\tau. \tag{15}$$

Similar analysis of the RHS of (13) yields an integro-partial differential equation for evolution of f(x, t) which has the form

$$\tau\, \partial/\partial t\, f\ - x\, \partial/\partial x\, f - 2f = R^{-1}\{\tfrac{1}{2} \int_0^x dx'[(x')^{-\alpha} + (x-x')^{-\alpha}] f(x',t) f(x-x',t) - \int_0^\infty dx'[(x)^{-\alpha} + (x')^{-\alpha}] f(x,t) f(x',t)\}, \tag{16}$$

where $R = \int_0^\infty x^{-\alpha} f(x, t)dx$, as in Appendix A. Evolution via (16) ensures that both $\int_0^\infty dx f(x,t)$ and $\int_0^\infty dx\, x f(x,t)$ are time-invariant (and thus remain equal to their initial values of unity).

Note that an analogous equation is available for the initial form, $f_0(x)$, of f(x, t) [28]. Also, the time-invariant version of (16) was obtained by Kandel [26] (apart from a typographical error). It is clear from (16) that the long-time limit, $f_\infty(x)$, of f(x, t) is

determined by α. An often quoted asymptotic estimate is [19] $f_\infty(x) \sim x^\alpha \exp[-(\alpha+1)x]$, for which $\sigma^2=0.4$ when $\alpha=1.5$.

Appendix C: Uncertainty in experimental estimation of size distribution properties

In analyzing experimental data, we estimate properties of the island size distribution from finite samples of M islands, where M≈100-300. Thus, it is appropriate to assess the expected values and likely error in these estimates. Below we let E[X] denote the expected value of some measured quantity X , and V[X] its mean-square uncertainty or variance. The "standard error" in the estimate is just the square root of this variance. Here, we neglect spatial correlations in the island distribution. Of obvious interest is the estimate, $s_{av}(M)$, from the sample of M islands of the exact average size, $s_{av}(\infty)=s_{av}$. Then, one finds that

$$E[s_{av}(M)]=s_{av}, \text{ and } V[s_{av}(M)]=A(s_{av})^2/M, \text{ where } A = \sigma^2 = \int_0^\infty (x-1)^2 f(x, t)dx. \qquad (17)$$

Thus, for typical $\sigma^2=0.1$-0.2 and M=100, the standard error in $s_{av}(M)$ is only 3-4% of s_{av}. Also of interest in this paper is the estimate, $\sigma^2(M)$, from a sample of M islands of the variance, $\sigma^2(\infty)=\sigma^2$, of the distribution f. One has that

$$E[\sigma^2(M)]=\sigma^2(M-1)/M, \text{ and } V[\sigma^2(M)]=B/M, \text{ where } B=\int_0^\infty x^4 f(x, t)dx - [\int_0^\infty x^2 f(x, t)dx]^2. \qquad (18)$$

For typical f where σ^2=0.1-0.2, one finds that B=0.4-1. Thus, for M=100, the standard error in $\sigma^2(M)$ is around 50% of σ^2 !

References

1. *Morphological Organization in Epitaxial Growth and Removal*, World Scientific Series in "Directions in Condensed Matter Physics," Vol. 13, edited by Z. Zhang and M.G. Legally (World Scientific, Singapore, 1998).
2. J.A. Venables, Philos. Mag. 27, 697 (1973); S. Stoyanov and K. Kashchiev, Curr. Top. Mater. Sci. **7**, 69 (1981); J.W. Evans and M.C. Bartelt, in Ref. 1.
3. M. Zinke-Allmang, L.C. Feldman, and M.H. Grabow, Surf. Sci. Rep. **16**, 377 (1992).
4. K. Morgenstern, G. Rosenfeld, and G. Comsa, Phys. Rev. Lett. **76**, 2113 (1996).
5. G. Schulze Icking-Konert, M. Giesen, and H. Ibach, Surf. Sci. **398**, 37 (1998).
6. J.B. Hannon, C. Klunker, M. Giesen, H. Ibach, N.C. Bartelt, and J.C. Hamilton, Phys. Rev. Lett. **79**, 2506 (1998).
7. J.-M. Wen, J.W. Evans, M.C. Bartelt, J.W. Burnett, and P.A. Thiel, Phys. Rev. Lett. **76**, 652 (1996); J.-M. Wen, S.-L. Chang, J.W. Burnett, J.W. Evans, and P.A. Thiel *ibid* **73**, 2591 (1994).
8. W.W. Pai, A.K. Swan, Z. Zhang, and J.F. Wendelken, Phys. Rev. Lett. **79**, 3210 (1997).
9. M. von Smoluchowski, Phys. Z **17**, 585 (1916).
10. K. Binder and M.H. Kalos, J. Stat. Phys. **22**, 363 (1980).
11. A.F. Voter, Soc. Photo-Opt. Inst. Eng. **821**, 214 (1987).
12. A. Bogicevic, S. Liu, J. Jacobsen, B. Lundqvist, and H. Metiu, Phys. Rev. B **57**, R9459 (1998); D.S. Scholl and R.T. Skodje, Phys. Rev. Lett. **75**, 3158 (1995); C.D. Van Siclen

ibid **75**, 1574 (1995); J.M. Soler, Phys Rev. B **50**, 5578 (1994); H.C. Kang, P.A. Thiel, and J.W. Evans, J. Chem. Phys. **93**, 9018 (1990).

13. J. Heinon, I. Koponen, J. Merikoski, and T. Ala-Nissila, Phys. Rev. Lett. **82**, 2733 (1999).
14. S.V. Khare and T.L. Einstein, Phys. Rev. B **57**, 4782 (1998); **54**, 11752 (1996); S.V. Khare, N.C. Bartelt, and T.L. Einstein, Phys. Rev. Lett. **75**, 2148 (1995).
15. R. Kern, G. LeLay, and J.J. Metois, in *Current Topics in Materials Science*, edited by E. Kaldis (North Holland, Amsterdam, 1979), Ch. 3.
16. W.B. Phillips, E.A. Deslodge, and J.G. Skofronick, J. Appl. Phys. **19**, 3210 (1968).
17. E. Ruckenstein and B. Pulvermacher, J. Catal. **29**, 224 (1973).
18. P. Meakin, Physica A **165**, 1 (1990).
19. D.S. Sholl and R.T. Skodje, Physica A **231**, 631 (1996).
20. H. Metiu, T.R. Mattsson, and G. Mills, in *Mechanisms and Principles of Epitaxial Growth in Metallic Systems*, MRS Proc. **528**, 133 (1998), edited by L.T. Wille, C.P. Burmester, K. Terakura, G. Comsa, and E.D. Williams (MRS, Pittsburgh, 1998); T.R. Mattsson, G. Mills, and H. Metiu, preprint (1999).
21. J.R. Sanchez and J.W. Evans, Phys. Rev. B. **59**, 3224 (1999).
22. Activation barriers for key PD processes [11,13,23] are roughly given by the sum of the barrier, E_e, for diffusion along <110> edges, and some multiple of an effective nearest-neighbor interaction. The terrace diffusion barrier satisfies $E_d \approx 2E_e$. The vacancy diffusion barrier, E_v, is set equal to E_e in Ref.[13], but it is likely higher. For Cu/Cu(100), one has E_v=0.44, E_e=0.25, E_d=0.43 (EMT [24]); E_v=0.42, E_d=0.52 (GGA [25]). For

Ag/Ag(100), one has E_v=0.42, E_e=0.25, E_d=0.37 (EMT [24]); E_v=0.46, E_e=0.26, E_d=0.49 (EAM [11]). All energies are in eV.

23. C.R. Stoldt, A.M. Cadilhe, C.J. Jenks, J.-M. Wen, J.W. Evans, P.A. Thiel, Phys. Rev. Lett. **81**, 2950 (1998).

24. P. Stoltze, J. Phys. Cond. Matter **6**, 9495 (1994).

25. G. Boisvert and L.J. Lewis, Phys. Rev. B **56**, 7643 (1997).

26. D. Kandel, Phys. Rev. Lett. **79**, 4238 (1997).

27. M.C. Bartelt and J.W. Evans, Surf. Sci. **298**, 421 (1993); Phys. Rev. B **46**, 12675 (1992).

28. M.C. Bartelt and J.W. Evans, Phys. Rev. B **54**, R17359 (1996).

29. M.C. Bartelt, C.R. Stoldt, C.J. Jenks, P.A. Thiel, and J.W. Evans, Phys. Rev. B **59**, 3125 (1999).

30. L. Bardotti, M.C. Bartelt, C.J. Jenks, C.R. Stoldt, J.-M. Wen, C.-M. Zhang, P.A. Thiel and J.W. Evans, Langmuir **14**, 1487 (1998).

31. C.-M. Zhang, M.C. Bartelt, J.-M. Wen, C.J. Jenks, J.W. Evans and P.A. Thiel, Surf. Sci. **406**, 178 (1998).

32. D.W. McComb, B.A. Collings, R.A. Wolkow, D.J. Moffatt, C.D. MacPherson, D.M. Rayner, P.A. Hackett, and J.E. Hulse, Chem. Phys. Lett. **251**, 8 (1996); T. Michely and G. Comsa, in Ref.[1].

33. G. Oshanin, M. Moreau, and S. Burlatsky, Adv. Colloid Interface Sci. **49**, 1 (1994).

34. C.R. Stoldt, A.M. Cadilhe, M.C. Bartelt, C.J.Jenks, P.A. Thiel and J.W. Evans, Prog. Surf. Sci. **59**, 67 (1998).

35. In Ref.7, the estimate of τ was based on the number of hops required for an atom (random walker) to visit of the order of $(L_{edge})^2$ sites. However, not all these sites need be visited for a cluster to collide with another cluster, since clusters are extended objects.

36. M.C. Bartelt, S. Gunther, E. Kopatzki, R.J. Behm, and J.W. Evans, Phys. Rev. B **53**, 4099 (1996).

37. C. Ratsch, A. Zangwill, P. Smilauer, and D.D. Vvedensky, Surf. Sci. **329**, L599 (1995).

38. E. Bauer, Z. Kristallogr. **110**, 372 (1958).

39. H. Roeder, K. Bromann, H. Brune, and K. Kern, Surf. Sci. **376**, 13 (1997).

40. C. Ratsch, A. Zangwill, and P. Smilauer, Surf. Sci. **314**, L937 (1994). For near-square islands, the strain energy is reasonable estimated from a 1d Frenkel-Kontorova theory treating the island as a composite of non-interacting 1d adatom chains.

41. M. Schroeder and D.E. Wolf, Surf. Sci. **375**, 129 (1997).

42. C. Ratsch, P. Ruggerone, and M. Scheffler, in Ref.[1].

43. J.de la Figuera, J.E. Prieto, C. Ocal and R. Miranda, Solid State Comm. **89**, 815 (1994).

44. J.C. Hamilton, Phys. Rev. Lett. **77**, 885 (1996).

Figure Captions

1. Sequences of STM images of the ripening of Ag island distributions on Ag(100) for two coverages: (a) θ=0.02 ML, with s_{av}^0 =60 atoms; (b) θ=0.21 ML with s_{av}^0 =510 atoms. All images are 150 nm × 100 nm.
2. Families of data illustrating the coarsening kinetics for three different fluxes: (a) F=0.011 ML/s; (b) F=0.006 ML/s; (c) F=0.003 ML/s. Data points for each STM experiment are shown as various solid symbols labeled by s_{av}^0-values. Corresponding behavior predicted from equation (8) with α=1.5 and D_0=50 Å^2/s is shown as solid curves.
3. Schematic showing the key linear dimensions for a typical island distribution: the mean separation between island centers, $L_{av}=(N_{av})^{-1/2}$; the mean island edge length, $R_{av}=\theta^{1/2}L_{av}$; and the mean separation between island edges, $L_{edge}=L_{av}-cR_{av}=(1-c\theta^{1/2})L_{av}$, where c is of order unity.
4. Best fits to the family of data for the experimental coarsening kinetics with F=0.003 ML/s [part (c) in Fig.2] from the rate equations with various α = 1.0 (a); 1.25 (b); 1.5 (c); 1.75 (d). Solid symbols show experimental data, and solid curves show predictions from equation (8).
5. (a) Rate equation prediction for the evolution of the shape, f(x, t), of the island size distribution using an initial form, $f_0(x)$, with a variance of 0.18 as described in the text. We set θ=0.16 ML and s_{av}^0=315 atoms. Curves show the form for the following times measured after deposition: 0 min. (the initial form), 5 min., 15 min., 50 min. (darker curve), 120 min, 240 min, and 400 min. As time increases, the left shoulder on the curve decreases, the peak increases, the right flank moves toward the left, and the large-x tail

increases. (b) The experimental size distribution from images containing a total of 420 islands [with s_{av}^0=315 atoms as in (a)] obtained about 50 min. after deposition of $\theta \approx 0.16$ ML of Ag at 295K with a flux $F \approx 0.006$ ML/s.

6. Evolution of the variance, σ^2, for three cases corresponding to experiments with F=0.003 ML/s and coverages of 0.02ML, 0.05 ML, 0.08 ML. (a) Estimates from experimental data (symbols), where dashed lines are shown as a guide to the general trend. (b) Rate equation predictions using an initial shape for the island size distribution, $f_0(x)$, with a variance of 0.18, as described in the text, and using θ- and s_{av}^0-values consistent with experiment.
7. Top: STM image of a 250 nm × 250 nm region showing 0.18 ML of Ag deposited on Ag(100). Bottom: Cross-sectional height profile taken horizontally through the center of the image (at a level indicated by the arrows), and spanning the oblong-shaped central protrusion.
8. Experimental data (solid symbols) for the coarsening kinetics for the region displayed in Fig.7. Rate equations with the modified choice of parameters D_0=250 $Å^2$/s and α=1.5 (solid curve) fit observed behavior, in contrast to those with the previous choice D_0=50 $Å^2$/s and α=1.5 (dashed curve).

Table Caption

I. Summary of initial conditions for the three families of data for coarsening kinetics shown in Fig.2. Shown are values for s_{av}^0, θ, N_{av}^0, and the initial value of the total number of islands in the region analyzed.

(a) Flux = 0.011 ML/s

S_{av}^0 (atoms/island)	θ (% ML)	$N_{av}^0 \times 10^{-5}$ (Å^{-2})	Number of Islands
530	25	5.7	230
205	14	8.1	165
65	4	7.3	145

(b) Flux = 0.006 ML/s

S_{av}^0 (atoms/island)	θ (% ML)	$N_{av}^0 \times 10^{-5}$ (Å^{-2})	Number of Islands
510	21	4.9	278
310	16	6.2	296
115	5	5.2	248

(c) Flux = 0.003 ML/s

S_{av}^0 (atoms/island)	θ (% ML)	$N_{av}^0 \times 10^{-5}$ (Å^{-2})	Number of Islands
270	8	3.5	123
140	5	4.2	150
60	2	4.0	109
40	1	3.1	140

Table I

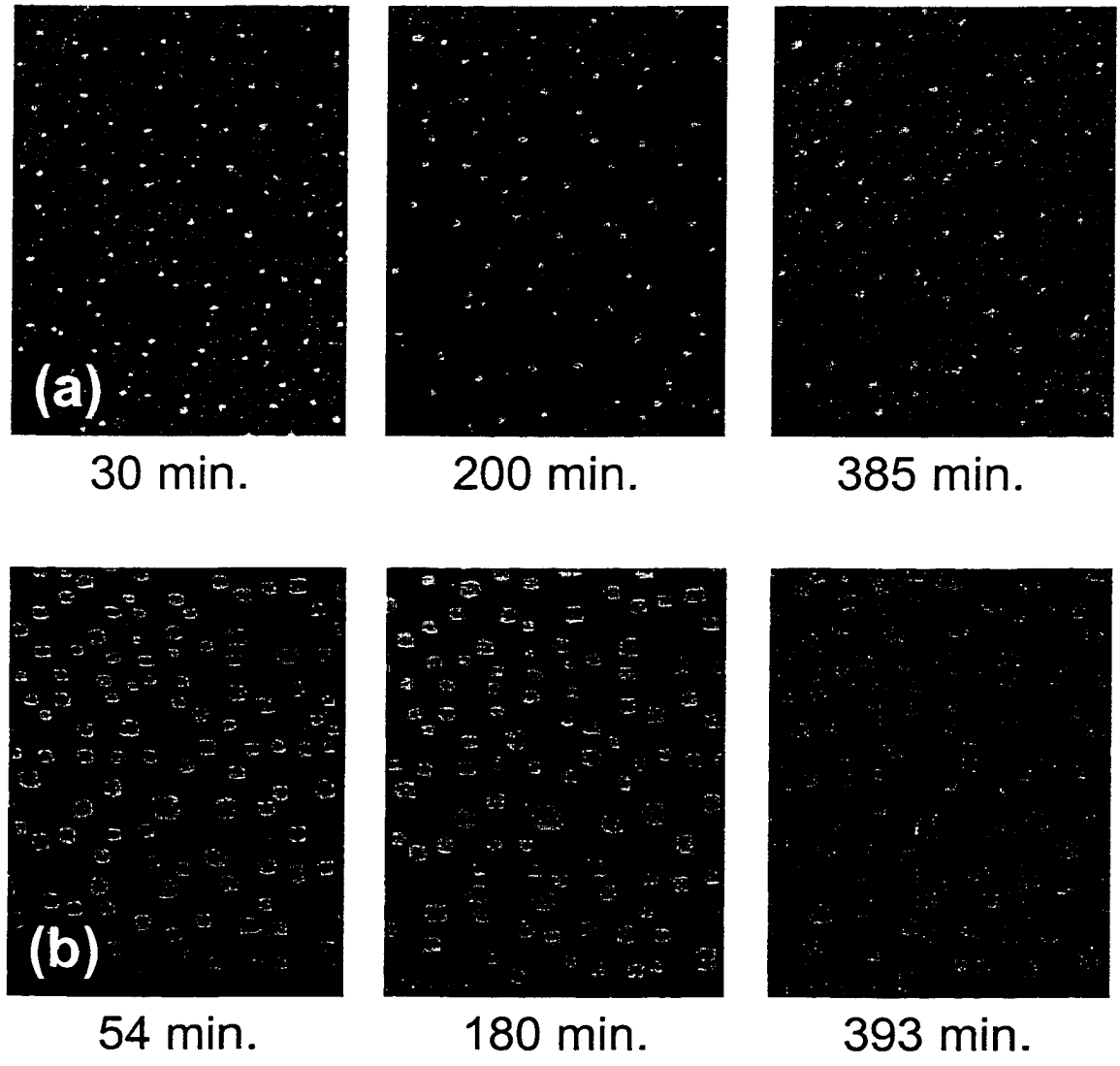

Figure 1

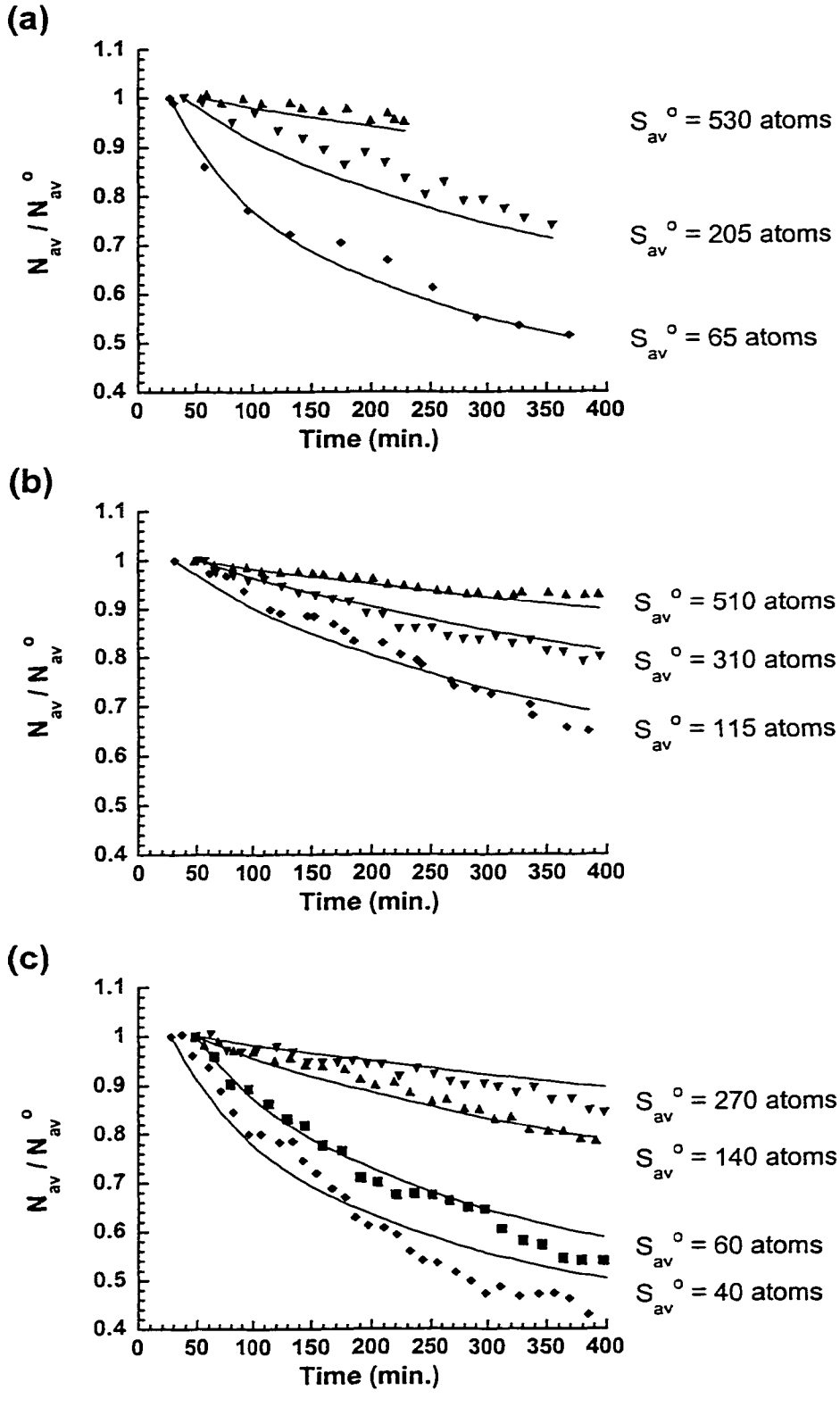
(a)
1.1
1
0.9
0.8
0.7
0.6
0.5
0.4
N_{av} / N_{av}^{o}
0 50 100 150 200 250 300 350 400
Time (min.)
S_{av}^{o} = 530 atoms
S_{av}^{o} = 205 atoms
S_{av}^{o} = 65 atoms
(b)
1.1
1
0.9
0.8
0.7
0.6
0.5
0.4
N_{av} / N_{av}^{o}
0 50 100 150 200 250 300 350 400
Time (min.)
S_{av}^{o} = 510 atoms
S_{av}^{o} = 310 atoms
S_{av}^{o} = 115 atoms
(c)
1.1
1
0.9
0.8
0.7
0.6
0.5
0.4
N_{av} / N_{av}^{o}
0 50 100 150 200 250 300 350 400
Time (min.)
S_{av}^{o} = 270 atoms
S_{av}^{o} = 140 atoms
S_{av}^{o} = 60 atoms
S_{av}^{o} = 40 atoms

Figure 2

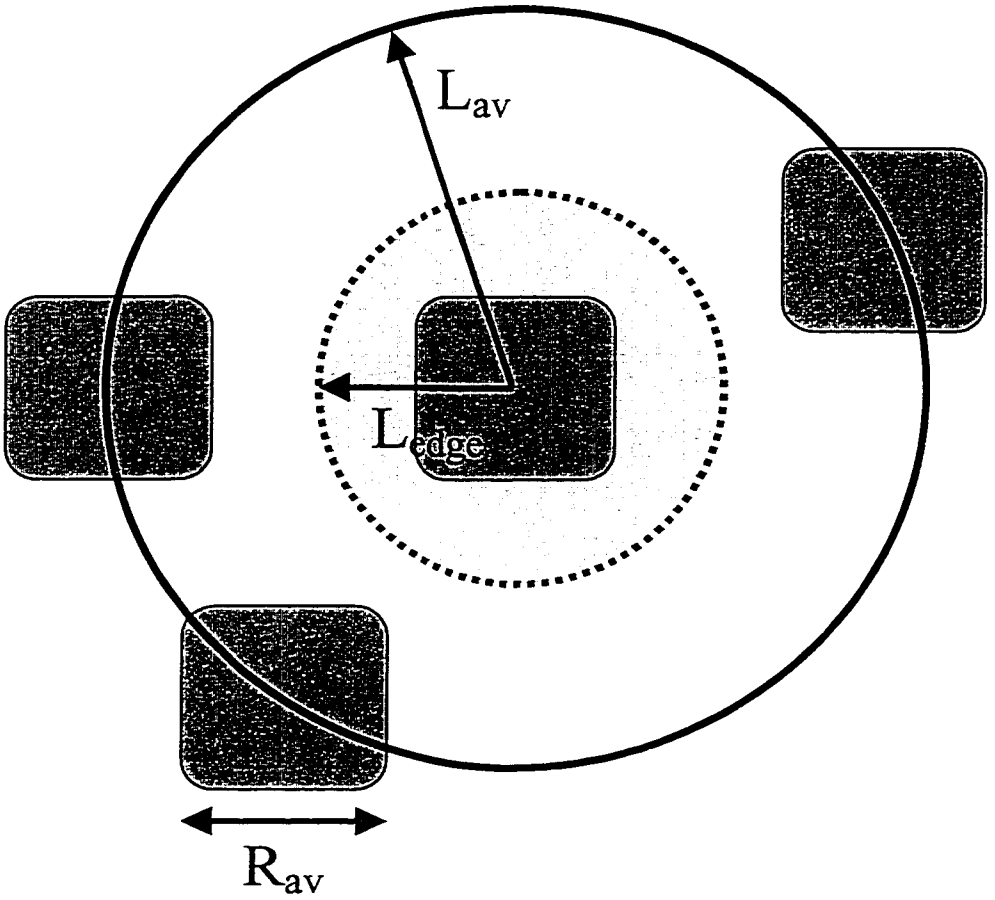

Figure 3

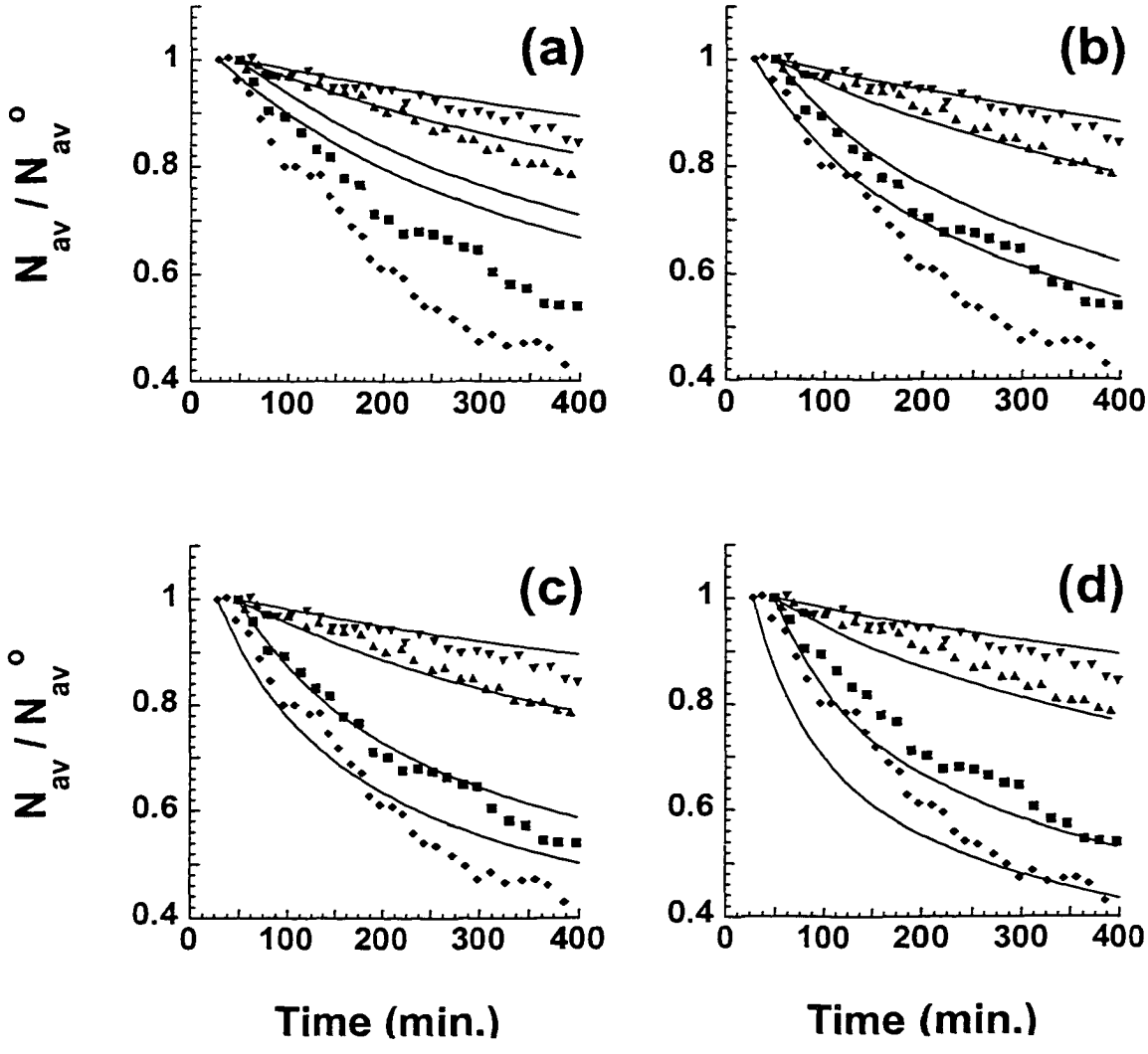

Figure 4

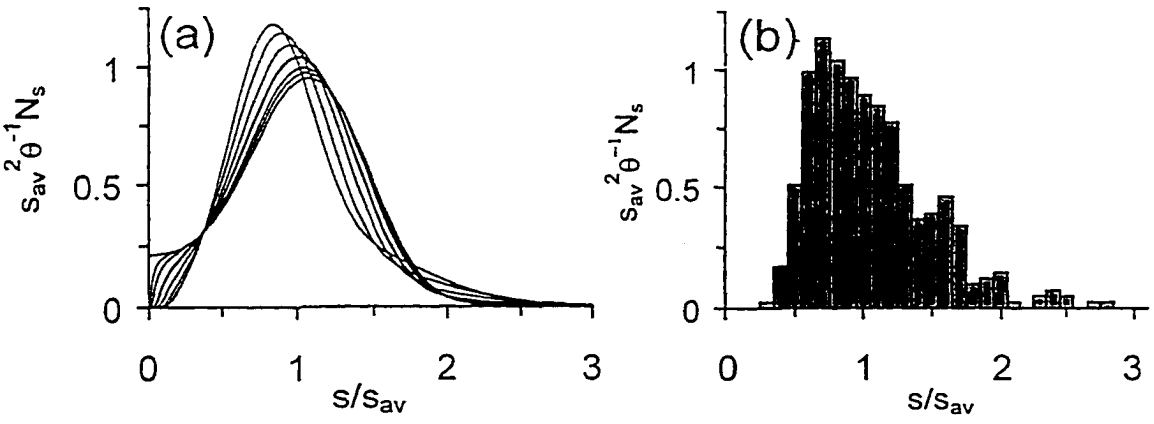

Figure 5

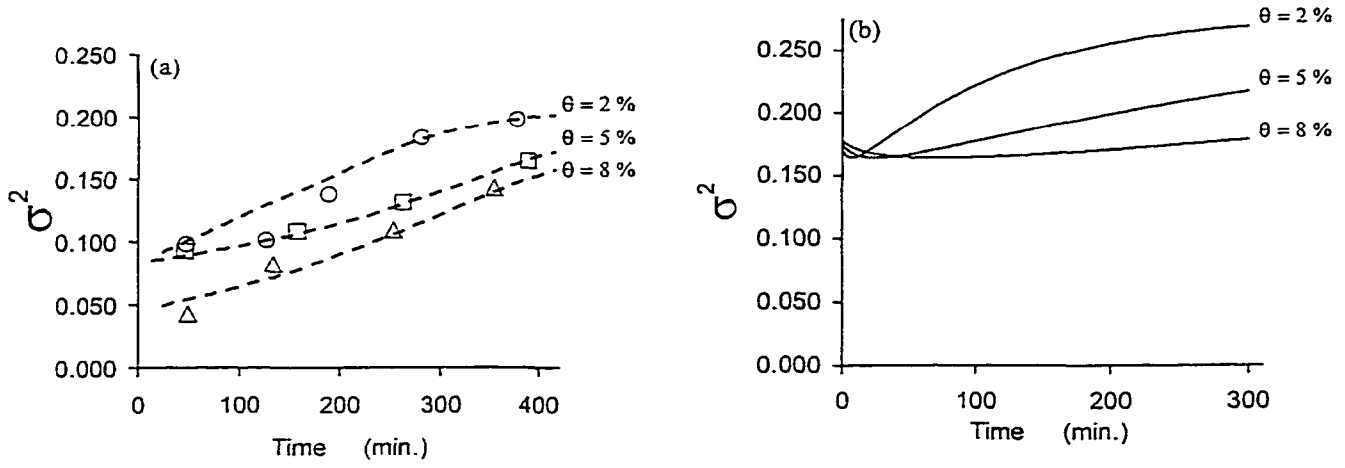
(a)
0.250
0.200
0.150
0.100
0.050
0.000
σ²
0
100
200
300
400
Time (min.)
θ = 2 %
θ = 5 %
θ = 8 %
(b)
0.250
0.200
0.150
0.100
0.050
0.000
σ²
0
100
200
300
Time (min.)
θ = 2 %
θ = 5 %
θ = 8 %

Figure 6

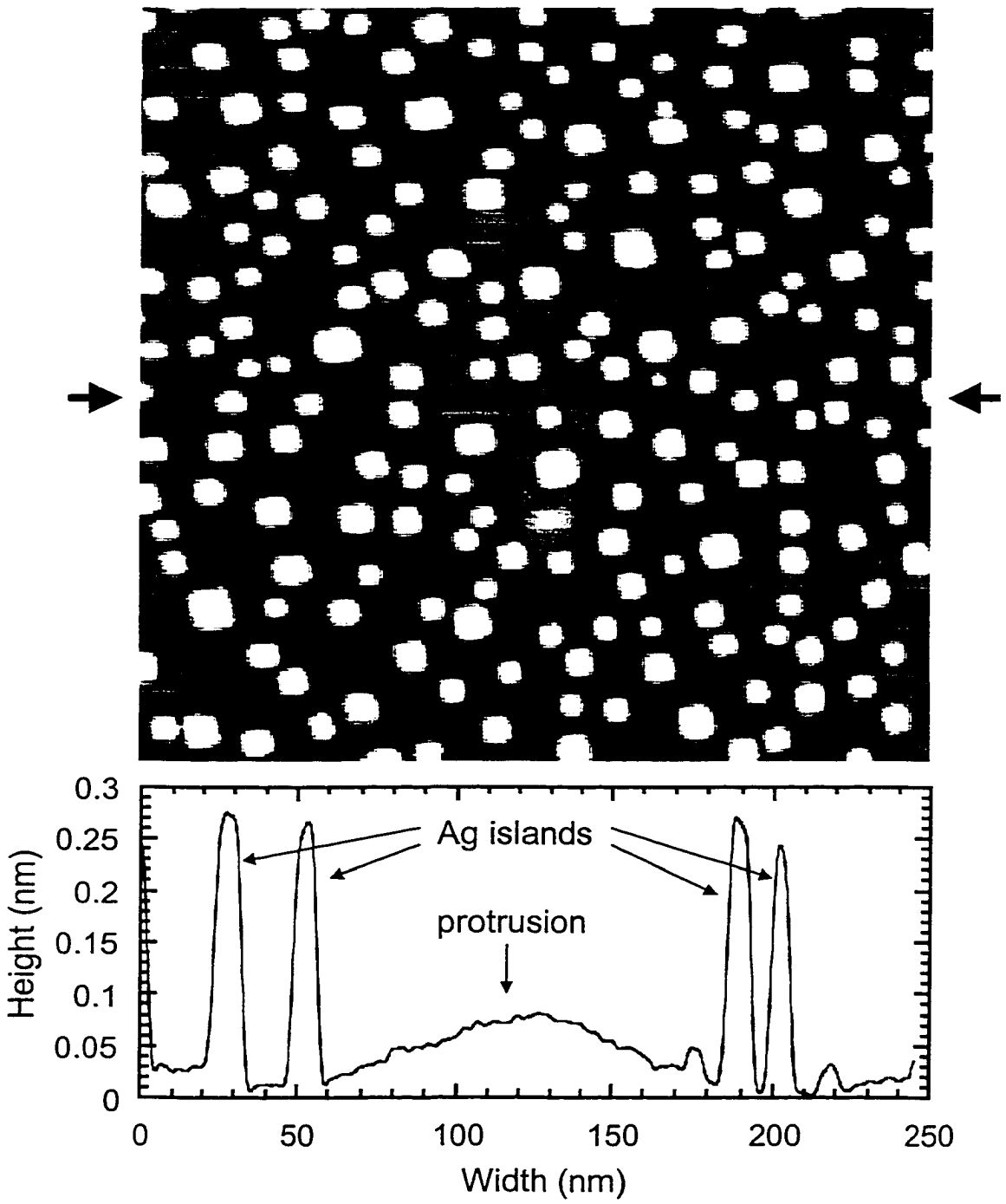
Ag islands
protrusion
Height (nm)
0.3
0.25
0.2
0.15
0.1
0.05
0
0
50
100
150
200
250
Width (nm)

Figure 7

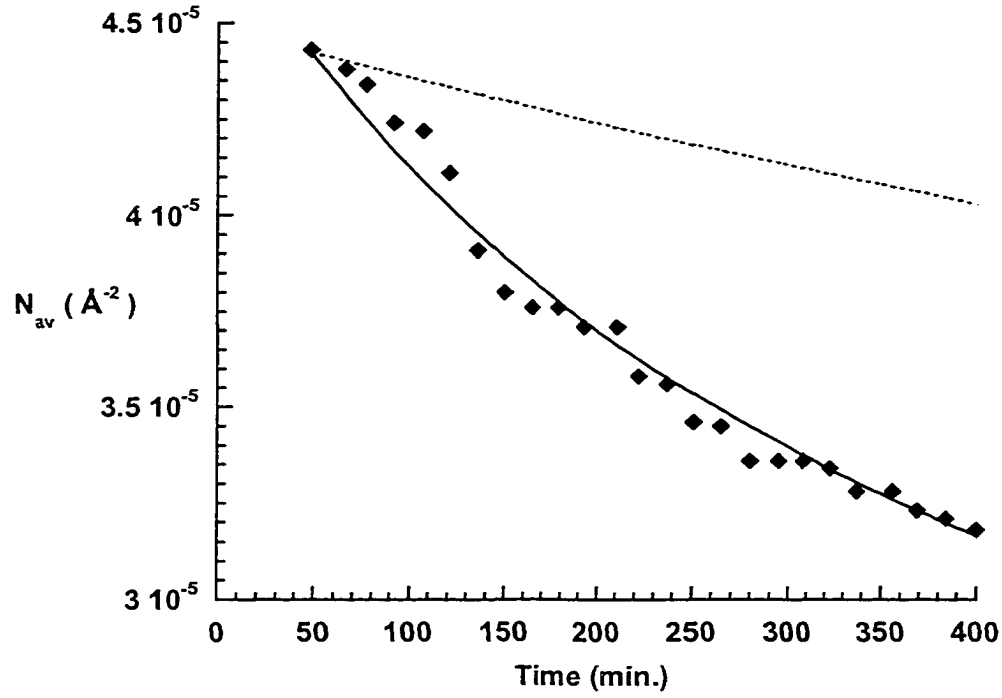
4.5 10-5
4 10-5
3.5 10-5
3 10-5
Nav (Å-2)
0
50
100
150
200
250
300
350
400
Time (min.)

Figure 8

IV. EVOLUTION OF FAR-FROM-EQUILIBRIUM NANOSTRUCTURES FORMED BY CLUSTER-STEP AND CLUSTER-CLUSTER COALESCENCE IN METAL FILMS

A paper published in Physical Review Letters

C.R. Stoldt, A.M. Cadilhe, C.J. Jenks, J.-M. Wen, J.W. Evans, and P.A. Thiel

PACS Numbers: 68.35.Bs, 68.35.Fx, 82.65.Dp

Abstract

Scanning Tunneling Microscopy experiments reveal the formation of a variety of geometrically exotic nanostructures following submonolayer deposition of Ag on Ag(100). These result from the diffusion of large Ag clusters, and their subsequent "collision" and coalescence with extended step edges, and with other clusters. Relaxation of these far-from-equilibrium step-edge configurations is monitored to determine rates for restructuring versus local geometry and feature size. This behavior is analyzed with lattice-gas model simulations to elucidate the underlying atomistic mass transport processes.

To obtain the most insight into the dynamics of erosion from observations over a limited time span, one would naturally examine the evolution of rugged landscapes rather than smooth terrains. Analogous observations apply to systems studied in physics. The response to slight perturbations or spontaneous fluctuations from equilibrium determines macroscopic transport coefficients [1], but the relaxation of systems far from equilibrium may provide more insight into underlying transport processes. Such relaxation can reflect a competition between various kinetic pathways, controlled by activation barriers for specific microscopic processes. In this paper, we study the relaxation of far-from-equilibrium two-dimensional (2D) step edge nanostructures or "landscapes" on metal surfaces to gain fundamental insight into the atomic-scale processes mediating the approach to equilibrium. This type of study is of relevance to recent intensive efforts to engineer nanostructures [2], which are often surface structures susceptible to rearrangement, in that it constitutes a step towards predicting, and even controlling, their useful lifetime.

One of the more surprising findings of recent Scanning Tunneling Microscopy (STM) studies is that metal surfaces near room temperature, which one might expect to be static, can actually be in a state of flux. This is evidenced by the observed equilibrium fluctuations or "frizziness" of monoatomic step edges on Cu, Au, and Ag surfaces [3]. Evolution of non-equilibrium structures created either by deposition [4], or by mechanically using the STM tip [5,6], is also observed. Large 2D clusters created by submonolayer deposition of metal(100) homoepitaxial films display unexpected diffusive mobility [7,8]. Cluster diffusion and subsequent coalescence upon collision, rather than Ostwald ripening, can even dominate adlayer coarsening [8,9]. For deposited multilayer Cu/Cu(111) films, diffusion of clusters in higher layers to step edges opens an efficient pathway for downward mass transport, and thus

film smoothing [10]. The decay of single layer 2D islands [11,12], as well as of multilayer island stacks [12] and holes [5], has been monitored on Ag(111) and Au(111) surfaces to elucidate associated mass transport processes. All these are examples of dynamic behavior of metal surface even at room temperature. We note also that sufficiently rapid restructuring of nanostructures influences multilayer film growth [13].

In this Letter, we study the relaxation at 295 K of far-from-equilibrium step edge nanostructures created by the diffusion and subsequent "collision" and coalescence of 2D Ag clusters with other clusters, and with extended step edges, on an Ag(100) surface (i.e., 2D sintering processes). A comprehensive characterization is provided for varying size, and local geometry of the initial stages of rapid relaxation or restructuring just after collision, where the configuration has a simple geometrical structure due to the near-square shape of islands. Successful, consistent comparison with simulations of a model for adatom diffusion along step edges elucidates the atomistic processes controlling mass transport

The key experimental details can be described briefly [7,9]. We used an Omicron room temperature STM housed in a UHV chamber with base pressure of below 10^{-10} Torr. Initial film configurations were created by evaporative deposition of Ag onto a single Ag(100) crystal. Large area scans of post-deposition evolution were taken at intervals of 3-15 min., and various examples of cluster diffusion and collision with other clusters and step edges were observed. Rates of change of key dimensions were then monitored, consistently using the FWHM of scan profiles. The database presented here was obtained with various tunneling conditions, and on several single crystals. Its self-consistency indicates that STM tip effects do not significantly influence nanostructure evolution. We focus on four distinct types of events (Fig.1): collision of clusters with extended step edges of (a) [110], and (b)

[100] orientations (these step edge geometries are shown in Fig.2); (c) side-to-side, and (d) corner-to-corner collision of pairs of square clusters. [110] is the equilibrium orientation of steps, but metastable [100] (and other) orientations result from depositing 0.6-0.8ML of Ag.

Analysis of the relaxation dynamics rests on key assumptions about the underlying atomistic processes, and of their energetics. First, consider mass transport at step edges mediated by perimeter diffusion (PD), wherein atoms hop along the step edge, but do not detach and reattach from it [14,15]. The key processes shown in Fig.2a include: fast edge diffusion along straight [110] steps at rate h_e; kink escape at rate h_k; corner rounding at rate h_r; and slow "core breakup" at rate h_c. Corresponding activation barriers are denoted by E_i (i=e, k, r, or c), and we assume a common attempt frequency, ν. We model the system with effective nearest-neighbor (NN) pairwise adatom interactions of magnitude J. Then, the detailed-balance relationship between rates for forward and reverse processes [16] implies that $h_k/h_e=h_c/h_r=\exp[-J/(k_BT)]$. Semi-empirical energy calculations for metal(100) homoepitaxy suggest that [14,16] $h_r \approx h_k$, so we choose $E_r \approx E_k = E_e+J$, and $E_c \approx E_e+2J$.

A goal of this work is to assess the effective activation barrier, $E_{act}(PD)$, for step-edge restructuring. Consider the decay of the rectangular protrusion on a [110] step edge shown in Fig.2b. At various stages, it is necessary to disrupt the "rectangular core" of the protrusion, and this requires "core breakup". (The same requirement was noted previously for cluster diffusion [7,14].) However, reduction of the height of the protrusion also requires repeated implementation of the combined process of kink escape followed by corner rounding. See Fig.2b. If $\rho_{eq} \approx h_k/h_e = \exp[-J/(k_BT)]$ denotes the quasi-equilibrium density of atoms released from the kink site, then this combined process occurs at an effective rate $h_{eff} \approx \rho_{eq} h_r \approx \nu \exp[-(E_r+J)/(k_BT)]$. Thus, both core breakup and the combined process of height reduction yield

the same $E_{act}(PD) \approx E_e + 2J$. Similar analysis of the decay of a triangular protrusion on a [100] step edge shown in Fig.2c reveals that most of the decay is mediated by core breakup steps, so again $E_{act}(PD) \approx E_e + 2J$ ($=E_c$).

It is appropriate to consider the competing pathway for mass transport via terrace diffusion (TD), i.e., detachment and reattachment of atoms from the step edge. The effective barrier for evaporation, and thus for mass transport, is $E_{act}(TD) = E_d + 2J$, where E_d denotes the terrace diffusion barrier [17]. For metal(100) homoepitaxy, a reasonable expectation is that [14,16] $E_e \approx E_d/2$. Thus, for Ag/Ag(100) where [18] $E_d \approx 0.40$eV, one has $E_e \approx 0.2$eV, and an energetic advantage of 0.2eV for PD over TD. Thus PD should dominate, at least for small-size features, and low temperatures. Consequently, the simulation studies described below use a simple lattice-gas model for the PD mechanism incorporating the atomic hops mentioned above, together with a constraint to preserve connectivity of atoms.

We now discuss in detail our experimental observations, and corresponding simulation analyses, for the 2D coalescence or sintering processes in Fig.1a-d. Below, rates are quoted in terms of the surface lattice constant, a=2.89 Å, for Ag(100).

(a) Cluster + [110] step coalescence (Fig.1a)

Here, the initial configuration is a square protrusion attached edge-on to a straight step. Experimental data indicates a roughly linear variation of the initial rate of decay of the protrusion height with its inverse area, for larger sizes (Fig.3a). Simulations confirm the equality $E_{act} \approx E_e + 2J (= E_c)$, and match observed rates if $E_{act} = 0.75$eV (specifically, $E_e = 0.20$eV, $J = 0.275$eV, and $\nu = 10^{12}$/s). Both experiment and simulation also show that the decay of a

square protrusion does not significantly perturb a perfectly aligned equilibrium [110] step edge, but that steps slightly misaligned from [110] adjust rapidly in the vicinity of the protrusion to achieve the preferred [110] orientation.

(b) Cluster + [100] step coalescence (Fig.1b)

After contact of a cluster corner with the [100] step, both experiment and simulation reveal the rapid formation of a connecting meniscus-like neck, together with indentations into the metastable step edge (see Fig. 1b). The rapid neck growth is primarily due to mass flow from the indentations. Simulations reveal an initial fast rise in the neck width with time for about 1 min., followed by more sustained quasilinear growth. For a 50×50 atom cluster, simulations with the above parameters yield a rate of quasilinear growth of 3.1 a/min., and produce a neck width of $35a \approx 100$ Å after about 5 min. These results are entirely consistent with the experimental behavior for the case in Fig.2b.

Later, an intermediate configuration of a near perfect right-angled triangle protruding from [100] step develops, the sides selecting the preferred [110] orientations (Fig.1b). Finally, this triangular protrusion slowly decays. The experimental decay rate of the height at onset of this final stage is shown in Fig.3b for various triangle sizes. Substantial uncertainties are due to large fluctuations during decay, including wandering and splitting of the protrusion peak. Simulation predictions with the above parameters are consistent with experiment, and show that again $E_{act}=E_e+2J$ $(=E_c)$. Decay rates here are far slower than those for square protrusions of the same size at [110] steps. This indicates that mass transport is less efficient along [100] steps than along [110] steps. Presumably, this is because the former requires

repeated core breakup steps, whereas the latter requires merely straight edge hopping and kink escape (cf. Fig.2b-c).

(c) Side-to-side cluster pair coalescence (Fig.1c)

For unequal sized square clusters which collide side-on, rapid mass flow first occurs to fill in the missing corner. This results in significant perimeter length reduction, and some decrease of the long dimension. This mass flow quickly leads to the formation of a long-lived (metastable) near-rectangular shape. The final stage of evolution from the near-rectangular metastable to the near-square equilibrium shape is much slower, as seen in both simulation and experiment. The rate of decay of the length is small and difficult to quantify due to significant fluctuations, especially for aspect ratios below about 3/2 (i.e., close to the equilibrium value of unity).

(d) Corner-to-corner cluster pair coalescence (Fig.1d)

For this configuration, one sees a fairly rapid formation of a meniscus-like neck, analogous to case (b). Neck growth leads to evolution from a dumbbell-shaped to a convex cluster. Subsequent slower evolution produces a near-square equilibrium shape. We focus on neck growth for roughly equal cluster sizes. Simulations again reveal an initial fast rise in the neck width with time, followed by more sustained quasilinear growth. Experimental data in Fig.3c for this rate of quasilinear growth show a roughly linear variation with inverse area of the cluster, for the range of experimental sizes. This behavior is consistently matched by simulations with the above parameters. The rate of quasilinear neck growth of 0.3 a/min. for two 50×50 atom clusters is substantially below the rate of 3.1 a/min. for the 50×50 atom

cluster in case (b). Clearly, neck growth for dumbbell-shaped clusters via mass transfer from their extremities is less efficient than neck growth via the creation of indentations in a [100] step edge.

In discussing the above results, we first emphasize that our direct STM observations of restructuring for suitably selected far-from-equilibrium nanostructures yield immediate insight into the underlying mass transport processes. The dramatic difference between the rate of decay of protrusions on [110] and [100] step edges reveals a strong dependence of the efficiency of mass transport on step orientation, and thus provides clear evidence for PD-dominated mass transport (since TD should have comparable efficiency for different orientations). This conclusion is supported by our argument for an energetic advantage of PD over TD, by the consistency of our analysis of experimental data with a PD model for very different geometries and sizes, and by the recent demonstration [7] that PD dominates other mass transport mechanisms in controlling the diffusion of 2D Ag clusters on Ag(100). However, the TD and uncorrelated 2D evaporation-condensation (EC) mechanisms of mass transport [7-9] always operate to some degree, in addition to PD, and could dominate under different conditions (e.g., higher T, or larger sized structures).

Some aspects of restructuring of the metal surface above seem fluid-like. Hence, it is natural to treat them in a coarse-grained or continuum approach where step edge evolution is driven by minimization of the step free energy. Mass flow is proportional to the gradient of a step chemical potential, which scales with curvature and step free energy. Simple Mullins-type evolution equations [19] produce slower restructuring with increasing protrusion or cluster area, A, but with rates scaling like $A^{-3/2}$ rather than the observed A^{-1}, for larger A (cf. Fig.3). Furthermore, continuum treatments cannot assess competition between kinetic

pathways, which can strongly influence behavior on the small length scales relevant here. This is most apparent if one considers the complete relaxation process, rather than just the initial restructuring: introducing an "easy" pathway for atoms to round kinks to reach doubly-coordinated sites (by concerted exchange with the corner atom), or a lower barrier (below E_c) for single atom diffusion along [100] steps, could significantly influence the kinetics and geometry of the late stage decay of protrusions at step edges.

Another aspect of the modeling involves the adatom interactions, treated here as effective NN pairwise interactions of strength J=0.275eV. Significantly, using such effective interactions to describe the observed transition to reversible island formation during deposition yields a consistent estimate of J≈0.3eV [18]. However, a more complicated detailed form for the interactions is likely, so we note that introducing attractive many-body interactions results in a smaller NN dimer pair interaction to fit experimental data.

As natural extension of the above, we have succeeded in creating almost perfect "mirror-images" of the adatom structures in Fig.1 (i.e., vacancy protrusions into extended step edges, and dumbbell- and rectangular-shaped vacancy clusters), and examined their relaxation. Prolonged deposition on a stepped surface leads to the advance of steps across terraces incorporating islands in the process, and producing an irregular growth structure. These step edges smoothen after deposition stops, occasionally leaving square vacancy protrusions into [110]-like steps (Fig.4a), and triangular vacancy protrusions into [100]-like steps (Fig.4b). Analysis of limited data for the decay of the depth of protrusions suggests comparable or faster decay rates than for adatom protrusions of the same size, and much higher rates for [110] than [100] steps. Deposition of ~0.8ML of Ag on large terraces produces irregular gaps between growing islands. These restructure to form more compact

vacancies, often with rectangular (Fig.4c) or dumbbell (Fig.4d) shapes. Neck growth for the vacancy dumbbell in Fig.4d is comparable to that for an adatom dumbbell of the same size.

In summary, analysis of the restructuring of exotic far-from-equilibrium step edge nanostructures in the Ag/Ag(100) system provides direct insight into underlying mass transport processes (and an estimate of 0.75eV for E_c). The current broad interest in fabrication of far-from-equilibrium nanostructures in surface systems fosters a need for studies like ours to elucidate possible decay mechanisms for such structures. This work was supported by NSF Grant CHE-9700592, and performed at Ames Laboratory, which is operated for the USDOE by Iowa State University under Contract No. W-7405-Eng-82.

References

1. L. Onsager, Phys. Rev. **37**, 405 (1931); **38**, 2265 (1931).
2. See, e.g., MRS Bulletin **23**, No.2 (1998).
3. M. Giesen-Siebert, *et al.*, Phys. Rev. Lett. **71**, 3521 (1993).
4. Z. Zhang and M.G. Lagally, Science **276**, 377 (1997).
5. R.C. Jakevic and L. Elie, Phys. Rev. Lett. **60**, 120 (1988).
6. J. Li, *et al.*, Phys. Rev. Lett. **76**, 1888 (1996).
7. J.-M. Wen, *et al.*, Phys. Rev. Lett. **73**, 2591 (1994).
8. W.W. Pai, *et al.*, Phys. Rev. Lett. **79**, 3210 (1997).
9. J.-M. Wen, *et al.*, Phys. Rev. Lett. **76**, 652 (1996).
10. M. Giesen, *et al.*, Phys. Rev. Lett. **80**, 552 (1998).
11. B.H. Cooper, *et al.*, MRS Proc. **280**, 37 (1993).
12. K. Morgenstern, *et al.*, Phys. Rev. Lett. **76**, 2113 (1996).

13. M.C. Bartelt and J.W. Evans, Phys. Rev. Lett. **75**, 4250 (1995).

14. A.F. Voter, SPIE **821**, 6819 (1986).

15. H. Shao, S. Liu, and H. Metiu, Phys Rev. B **51**, 7827 (1995).

16. M. Langelaar, Ph.D. Thesis (1998); M. Breeman, *et al.*, Surf. Sci. **303**, 25 (1993).

17. If detachment (or bond-breaking) of atoms from [110] edges has rate h_b, and terrace hopping has rate h_d, then $h_b/h_d=\exp[-J/(k_BT)]$. The effective rate of detachment is $\rho_{eq}h_b$.

18. C.-M. Zhang, *et al.*, Surf. Sci. **406**, 178 (1998).

19. W.W. Mullins, J. Appl. Phys. **30**, 77 (1959).

Figure Captions

1. Coalescence of: (a) a cluster & [110] step, with collision at ~10 min. (image=35×35 nm^2); (b) a cluster & [100] step (58×58 nm^2); (c) a side-to-side cluster pair (35×35 nm^2); (d) a corner-to-corner cluster pair (38×38 nm^2).

2. (a) Key perimeter diffusion processes (see text). (b) Decay of protrusions at $[1\bar{1}0]$ (or equivalently [110]), and [100] step edges.

3. Decay rate, R, vs. 1/area for the height of: (a) square protrusions at [110] step edges; (b) triangular protrusions at [100] step edges. (c) Neck growth rate, G, vs. 1/(single cluster area) for corner-to-corner cluster coalescence. Right insets show simulated configurations.

4. Vacancy protrusion decay at: (a) a [110] step (image=20×20 nm^2); (b) a [100] step (50×50 nm^2). Vacancy cluster restructuring for: (c) a rectangular shape (45×45 nm^2); (d) a dumbbell shape (54×54 nm^2).

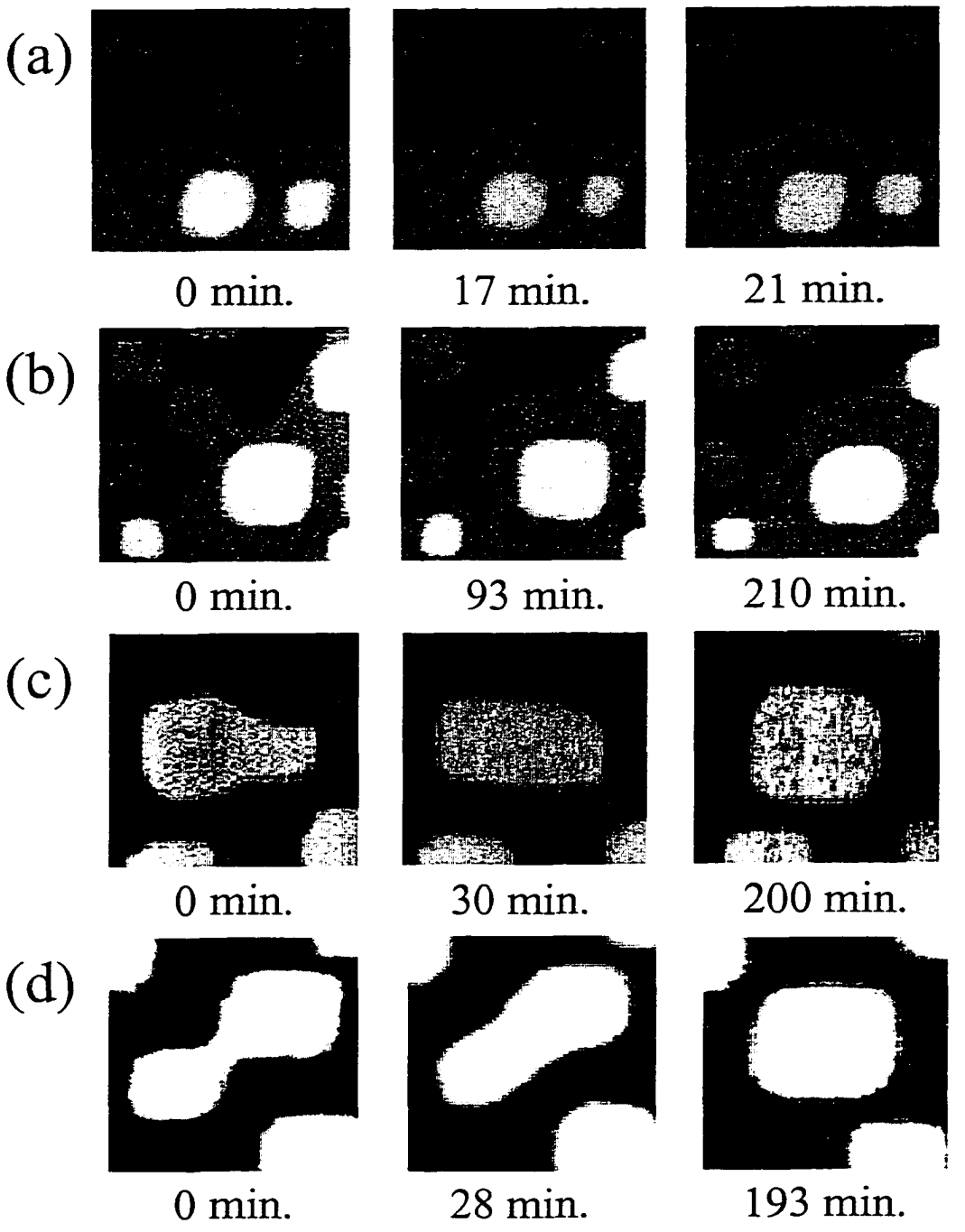
(a)
0 min.
17 min.
21 min.
(b)
0 min.
93 min.
210 min.
(c)
0 min.
30 min.
200 min.
(d)
0 min.
28 min.
193 min.

Figure 1

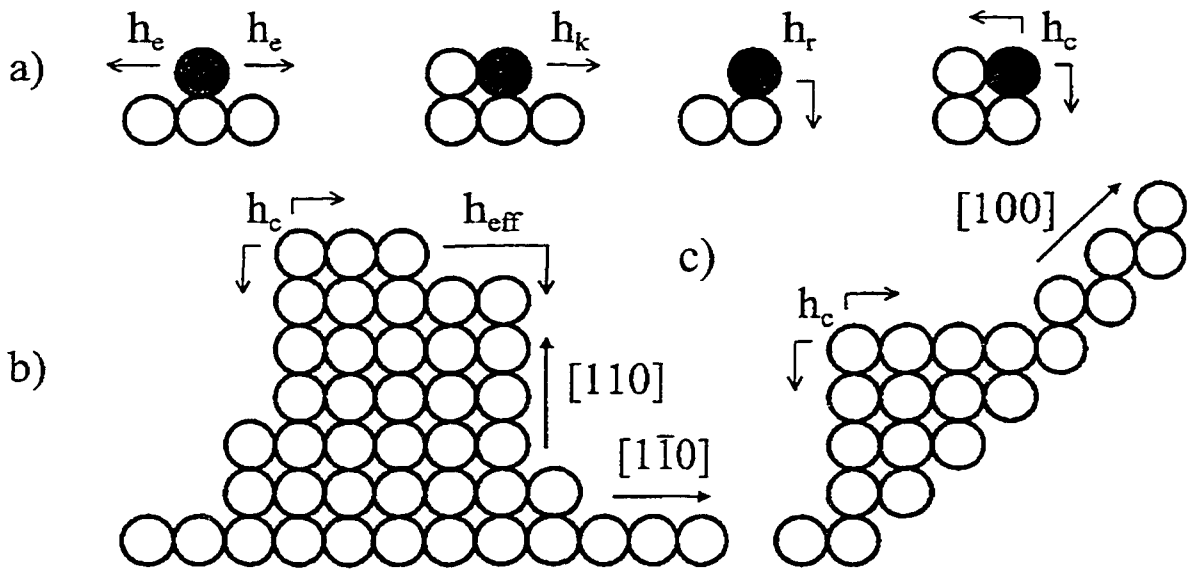

Figure 2

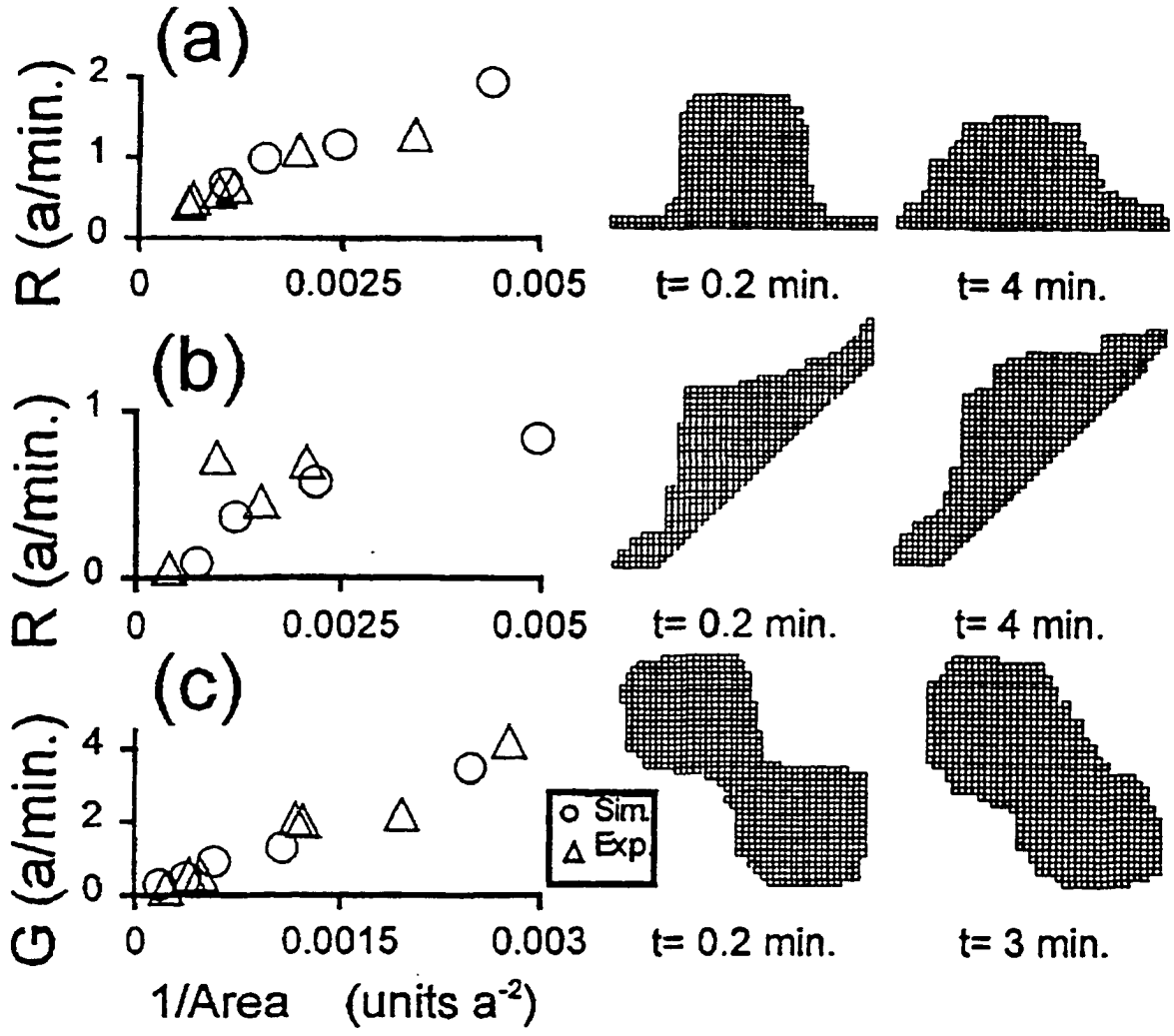
(a)
R (a/min.)
2
1
0
0
0.0025
0.005
t= 0.2 min.
t= 4 min.
(b)
R (a/min.)
1
0
0
0.0025
0.005
t= 0.2 min.
t= 4 min.
(c)
G (a/min.)
4
2
0
Sim.
Exp.
0
0.0015
0.003
t= 0.2 min.
t= 3 min.
1/Area (units a-2)

Figure 3

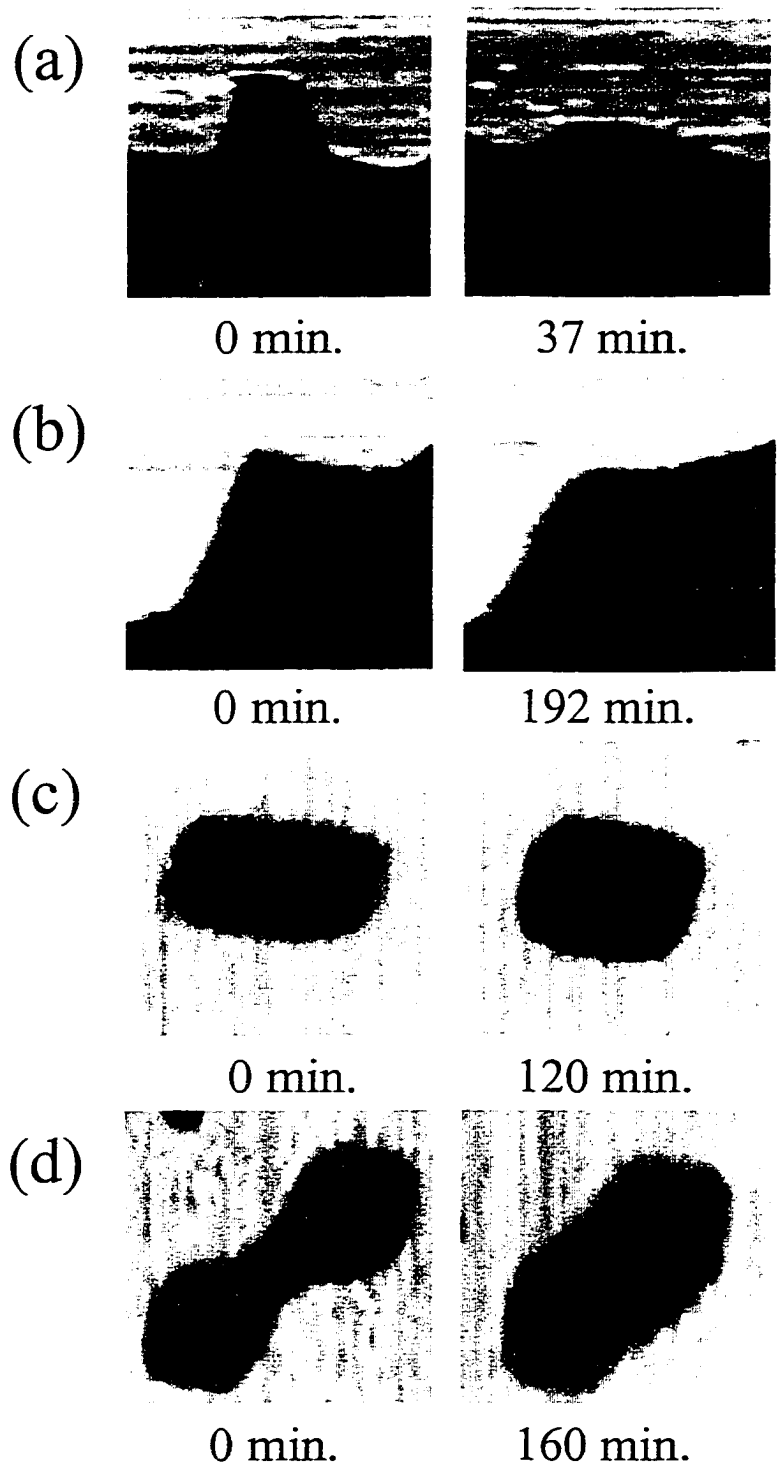

Figure 4

V. COMPLEX TEMPERATURE DEPENDENCE IN MULTILAYER FILM GROWTH

A paper to be submitted to the journal Science

C.R. Stoldt[1], K.J. Caspersen[1], M.C. Bartelt[2], C.J. Jenks[1], J.W. Evans[1], and P.A. Thiel[1]

[1]Departments of Chemistry and Mathematics, and Ames Laboratory,

Iowa State University, Ames, IA 50011

[2]Sandia National Laboratories, Livermore, CA 94550

Abstract

Ag/Ag(100) homoepitaxy constitutes one of the simplest multilayer growth systems. Yet, we find a variation of the roughness, W, with temperature, T, more complex than any observed previously in metal epitaxy. Scanning Tunneling Microscopy studies of 25ML films reveal an increase in W as T is lowered from 300K to 220K, then a decrease in W down to 140K, followed by another increase for lower T (at least to 50K). A transition from mound formation to self-affine growth occurs below ~160K. Suitable atomistic modeling reproduces this behavior and elucidates the underlying mechanisms.

PACS Numbers: 68.35.Bs, 68.35.Ct, 68.35.Fx, 68.55.-a, 68.55.Jk

The surface morphologies of films grown by deposition on perfect substrates reveal rough far-from-equilibrium configurations, particularly at low temperatures where equilibration is limited. Furthermore, important physical properties of such films depend sensitively on these morphologies, particularly on roughness. Obvious examples are magnetic properties of thin metal films[1], superconducting and localization transitions in quench condensed films[2], electrical conductivity of metal films on semiconductors[3], catalytic properties of bimetallic thin films, etc.. Thus, a fundamental and comprehensive understanding (and ultimately control) of the atomic-scale processes and mechanisms determining film morphology is a crucial goal.

This goal has yet to be achieved even for simple metal homoepitaxial systems, which provide a natural testing ground for ideas on kinetic roughening. Here, and in other systems, basic perceptions of film growth have been influenced by "rain model" for low T growth, where randomly deposited atoms irreversibly sticking at landing sites in an simple cubic (SC) geometry.[4] One finds very rough growth characterized by a Poisson height distribution. This behavior persists whenever interlayer diffusion inoperative (in an SC geometry). At high T, interlayer diffusion is operative producing smoothing. Thus, the expectation was that roughness increases monotonically with decreasing T (i.e., with enhanced kinetic barriers to equilibration). In reality, metal film deposition and growth is far more complex. Dramatic illustrations are provided by a non-monotonic variation of roughness with T for both the Pt/Pt(111)[5] and Rh/Rh(111)[6], a feature related to a transition between compact and fractal 2D island shapes. An earlier surprise in "simpler" metal(100) homoepitaxy (where there is no dramatic island shape transition) was the observation of smooth growth at 77K, as reflected

by persistent diffraction intensity oscillations[7]. More recently, roughness was observed to decrease from 200 to 160K for Cu/Cu(100)[8], but to increase from 300K to 200K for Ag/Ag(100)[9]. The discovery of such novel growth characteristics illustrates that studying the variation of film roughness and morphology with substrate temperature can be of key importance in revealing and understanding the microscopic processes which dictate film properties.

However, most of the recent intense interest and activity in multilayer growth has focussed on characterizing kinetic roughening at a specific T.[4] For metal homoepitaxy, one often observes the development of three-dimensional (3D), pyramid-like mounds on the surface.[5,6,8,10] This reflects the presence of an additional (Ehrlich-Schwoebel) potential barrier for downward diffusion at step edges suppressing interlayer diffusion.[4] Villain[11] noted that since diffusing atoms are deflected away from descending step edges, this enhances the rate of capture of diffusing atoms at ascending step edges, resulting in a net mass flow in the upwards direction. This unstable growth produces mounds. There is ongoing interest in the nature and mechanism of the coarsening of these mounds, and its relation to roughening, as well as in slope selection.[12-14] Another generic class of behavior is self-affine growth, as is observed in many more complex systems.[4,15] A distinction between these classes is provided by examination of height correlation functions which reflect a characteristic separation for mounding, versus a continuous spectrum of lengths for self-affine growth. A single system usually exhibits just one these two behaviors.

In this Report, we study the T-dependence of the growth of multilayer Ag films on the Ag(100) surface between 300K and 50K, using Variable-Temperature Scanning

Tunneling Microscopy (VT-STM). Despite the fact that this is perhaps the "simplest" growth system, we find a variation of roughness more exotic than any observed previously in metal epitaxy! Specifically, the roughness of 25 ML Ag films increases as T drops from 300K to 220K, then decreases as T drops further to 140K, and finally increases again for lower T (at least down to 50K). We also characterize the lateral film morphology revealing a transition from mound formation to self-affine growth, as T drops below about 150-160K. Also examined is the scaling behavior for the rough growth at 230 K, which corresponds to mound formation with "slow" slope selection. Successful comparison with suitable models for metal(100) epitaxy elucidate the atomistic processes controlling multilayer film structure: unstable growth due to a small step edge barrier of ~30meV at higher T; re-entrant smooth growth and a transition to self-affine growth due to downward funneling at more prevalent step edges for lower T; a transition to rough growth at very low T due to the breakdown of funneling on small steep microprotrusions.

Our experimental data are acquired using an Omicron VT-STM housed in a UHV chamber with base pressure below 10^{-10} Torr. The Ag(100) single crystal is prepared through repeated cycles of Ar ion sputtering and annealing to 750 K. Contamination is minimal, based on inspection of STM images and Auger spectroscopy. Typical terrace widths on the Ag(100) substrate are > 1000 Å. Ag films are formed by evaporative deposition of pure Ag from an Omicron EFM3 UHV evaporator. After deposition, the substrate T remains fixed (± 5 K) and all surface information is obtained from central portions of broad terraces in order to minimize the effect of step edges on data analysis.

In Fig.1, we begin by showing STM images of 25 ML Ag films grown on Ag(100) as a function of deposition T. In order to characterize the vertical morphology, we discretize the

continuous height distribution from STM (by peak fitting using multiple Gaussian functions with a separation equal to the interlayer spacing). The resulting rms surface roughness or interface width, W (in units of interlayer spacing) versus T is shown in Fig.2a for 25 ML Ag films deposited at F≈0.02ML/s. The remarkably complex T-variation is described above.

To characterize the lateral morphology in the STM images, we examine the height-height correlation function, H(**r**), which gives the mean-square height difference for a lateral separation of **r**. The typical form of H(**r**) at 230 K is plotted in the inset of Fig. 2b, where the first maxima and minima correspond roughly to the average mound radius (R_{av}), and separation (D_{av}), respectively. Figure 2b shows the T-dependence of R_{av} and D_{av} ($\approx 2R_{av}$), as determined from the STM images. The observed trend is consistent with the images of Fig. 1: D_{av} decreases rapidly with decreasing T to about 205 K, after which it remains roughly constant. The existence of oscillations in H(**r**) at 175 K and above reflects formation of somewhat ordered arrays of mounds. At 135 K and below, there are no well-defined oscillations in H(**r**), suggesting self-affine growth. This claim is supported by examining the roughness exponent, α, determined from the roughness, W_L, for a range of shorter STM scan lengths, L,[15] and using $W_L \sim L^{\alpha}$. Values of α (where $0<\alpha<1$) significantly below unity indicate a self-affine growth topography.[4] We find that $\alpha \approx 1$ above 135 K, while α decreases to less than ~0.5 below 135 K. We also determine the T-dependence of the average surface slope, and the slope of the sides of mounds (see Table I). These (and other) measures of slope increase monotonically with decreasing T.

We now discuss in more detail the behavior shown in Fig.s 1-2 with regard to the possible atomic processes responsible for the observed growth characteristics. The discussion

and analysis is naturally split into the two temperature regimes for mounding and self-affine growth.

Mounding Regime at Higher-T:

At 300 K (Fig.1a), and above, Ag/Ag(100) growth appears "quasi-layer-by-layer" due to slow development of flat mounds. (This contrasts systems with far larger E_{se}.[5,6]) As the deposition temperature is reduced from 300 K, mounds become more pronounced as interlayer diffusion becomes more inhibited, reflected in an increase in W (Fig. 2a). W peaks between 205 and 230 K (Fig 2a), where near square mounds with broad, flat summits are observed (Fig. 1d-f). X-ray scattering experiments also show a similar increase in W between 200 and 300 K for ~15 ML Ag films on Ag(100).[9] In the mounding regime between 175K and 300 K, we analyze the Arrhenius behavior of the mound separation, D_{av}. Using data from H(**r**) in Fig. 2b from 190–300 K yields an Arrhenius energy of $E \approx 0.07$eV. In this regime of irreversible island formation, the characteristic separation for both submonolayer islands and multilayer mounds should scale like the sixth power of the terrace diffusion rate.[4] This implies an activation barrier for terrace diffusion of $E_d = 6E \approx 0.45$ eV. This result is consistent with estimates of E_d for Ag/Ag(100) from submonolayer STM and HRLEED studies (0.38-0.42eV)[16], from ion scattering (0.4eV)[17], as well as from density functional theory calculations (0.45eV)[18].

Below ~200 K, terrace diffusion becomes severely inhibited due to the "high" E_d, leading to a high density of step edges. This morphological change is readily seen in the STM images of Fig. 1f-g, where feature size decreases significantly with decreasing T. There thus develops a significant "downhill" mass flow due to the downward funneling (DF) or deflection of atoms deposited at these step edges to lower fourfold hollow (4FH) adsorption

sites on the (100) surface.[20] This acts to smooth the surface, evidenced by the sharp decrease in W (Fig. 2a), and ultimately to stabilize growth inducing a transition out of the mounding regime.[20]

To describe behavior between roughly 300 and 150K, we employ a kinetic Monte Carlo (KMC) simulation model for metal(100) homoepitaxial film growth that incorporates the irreversible formation of square islands mediated by terrace diffusion, and downward funneling. Thermal interlayer diffusion occurs at a reduced rate due to the presence of an additional step edge barrier, E_{se}. For a more detailed description of this simulation model, see Ref. 20. We assign E_d=0.4eV based on previous studies, while E_{se} is estimated as 30 ± 5 meV from a fit to the experimental data at 230 K. All attempt frequencies are set to 10^{13}/s. As shown in Fig.3a, this kinetic model reproduces the observed T dependence of W between 300 and 135 K. The model also reproduces the monotonic increase in slope with decreasing T.

Self-Affine Growth Regime at Lower-T:

Below 135 K, W increases again. Why? Molecular Dynamics (MD) simulations of metal(100) homoepitaxy indicate that downward funneling can "fail" on steep microprotrusions, i.e., deposited atoms sometimes "get stuck" on the sides rather than reaching lower 4FH sites.[21] For lower T, the increase in local slope of the surface enhances this effect, producing films with overhangs, internal defects, and larger W.[21] But what is the origin of the T-dependence in this regime where (100) terrace diffusion is inoperative? The key point is that there are many other thermally activated hopping processes, with lower barriers, E_{act}, which can be operative and affect film morphology. For example, atoms adsorbed at 3FH sites on the sides of {111} microfacets are mobile above 40K,[22] leading to novel downward transport processes.

Our modeling of low-T film growth, between 0 and 150K, is described as follows. We first develop and analyze a "restricted downward funneling" (RDF) model for growth at 0 K. Specifically, deposited atoms funnel down until they reach a site with: at least three supporting atoms in the layer beneath; or two such atoms beneath and at least one in-layer neighbor; or one atom beneath and at least two in-layer neighbors. In this RDF model, the roughness increases much more quickly than for the standard DF model, with $W^{RDF} = 1.41$ versus $W^{DF} = 0.74$ for a 25 ML film. Only the former is consistent with experimental observations at around 50K.

To describe (observed) film growth up to around 150K, we augment the above RDF model by incorporating various hopping processes for atoms with low coordination number, m, as follows: hopping is instantaneous for $m<3$; $E_{act}=0.10$eV for $m=3$ (or 0.15eV for three supporting atoms); $E_{act}=0.25$eV for interlayer hops with $m=4$ (and $m=5$). Attempt frequencies are set to 10^{12} s^{-1}. These choices are motivated by the known terrace diffusion barrier of 0.10eV for Ag/Ag(111),[22] and by semi-empirical studies of energetics. As T is increased, these processes become operative, leading to a variation in W for a 25 ML film shown in Fig. 3b. This is consistent with experimental observations. Film growth models with internal defects should ultimately achieve KPZ-scaling,[23] but this does not apply in our experimental regime.

Kinetic Roughening at 230K:

Finally, we examine the evolution of mounds as a function of film thickness, θ, at 230K, motivated by the still considerable uncertainty as to the relation between atomistic processes controlling growth, and mesoscopic evolution. In Fig. 4a-d, we display STM images of multilayer Ag films of varying thickness deposited at 230 K. Fig. 4a shows the

quasi-layer-by-layer growth morphology of a 5ML film with small 2D islands and vacancies, where mounds are only beginning to develop. Above 10 ML, well-defined mounds have formed. Table II reports the evolution of $W \sim \theta^{\beta}$. A fit of the data between 10 and 100 ML yields a growth exponent, $\beta \approx 0.32$. This reasonably matches both $\beta \approx 0.37$ from KMC simulations at 230K, and $\beta \approx 0.28$ from X-ray scattering[9] at 200K. Mound coarsening as quantified by D_{av} (or R_{av}) $\sim \theta^{n}$ is described by a much lower exponent of $n \approx 0.18$. The θ-dependence of local slope indicates a rather slow slope selection with saturation above 50 ML. See Table II. Behavior is reminiscent of continuum theories for mound evolution without slope selection in the regime of irreversible island formation, which predict small $n \approx 1/6$ and large $\beta \approx 1/2$.[12] Interestingly, behavior follows more closely recent predictions[13] based on analyses of noise- or step-edge-restructuring-[24] induced mound coalescence that the ratio $\theta^{1/2}/(WD_{av})$ is constant [≈ 0.1 for our data, with D_{av} (W) in units of the horizontal (vertical) lattice spacing], so $\beta+n=1/2$ for simple scaling. This relation reveals an interplay between roughening and mound coarsening: faster roughening inhibits coarsening.

In summary, we have shown that the simple system, Ag/Ag(100), exhibits the most exotic variation of W vs. T of any metal multilayer system yet observed. Characterization and atomistic modeling of the vertical and horizontal morphologies of deposited films provides direct insight into the deposition and diffusion processes controlling observed behavior. This work was supported by NSF Grant CHE-9700592, and performed at Ames Laboratory, which is operated for the USDOE by Iowa State University under Contract No. W-7405-Eng-82. MCB was supported by the USDOE (BES) under Contract No. DE-AC04-94AL85000.

References

1 See, e.g. MRS Bulletin, **21**, no. 9 (1996).

2 K.L. Ekinci and J.M. Valles, Phys. Rev. B **58**, 7347 (1998).

3 M. Horn-von Hoegen *et al.*, in *Morphological Organization in Epitaxial Growth & Removal*, Z. Zhang and M.G. Lagally, Ed.s (World Sci., Singapore, 1998).

4 A.-L. Barabasi and H.E. Stanley, *Fractal Concepts in Surface Growth* (University Press, Cambridge, 1995).

5 R. Kunkel *et al.*, Phys. Rev. Lett. **65**, 733 (1990).

6 F. Tsui *et al.*, Phys. Rev. Lett. **76**, 3164 (1996).

7 W.F. Egelhoff and I. Jacob, Phys. Rev. Lett. **62**, 921 (1989).

8 H.-J. Ernst *et al.*, Phys. Rev. Lett. **72**, 112 (1994).

9 W.C. Elliot *et al.*, Phys. Rev. B **54**, 17938 (1996).

10 J.A. Stroscio *et al.*, Phys. Rev. Lett. **75**, 4246 (1995); K. Thurmer *et al.*, *ibid*, **75**, 1767 (1995); J.-K. Zuo and J.F. Wendelken, *ibid*, **78**, 2791 (1997); M. Kalff *et al.*, Surf. Sci. Lett. **426**, L447 (1999).

11 J. Villain, J. Phys. I (France) **1**, 19 (1991).

12 L. Golubovic, Phys. Rev. Lett. **78**, 90 (1997).

13 L.-H. Tang, P. Smilauer, and D.D. Vvedensky, Euro. Phys. J. B **2**, 409 (1998).

14 M. Siegert, Phys. Rev. Lett. **73**, 5481 (1998); M.V. Ramana Murty and B.H. Cooper, *ibid*, **83**, 352 (1999); J.G. Amar, Phys. Rev. B **60**, R11317 (1999).

15 J. Krim *et al.*, Phys. Rev. Lett. **70**, 57 (1993).

16 C.-M. Zhang *et al.*, Surf. Sci. **406**, 178 (1998); L. Bardotti *et al.*, Phys. Rev. **B** 57, 12544 (1998).

17 M.H. Langelaar *et al.*, Surf. Sci. **352-354**, 597 (1996).

19 B.D. Yu and M. Scheffler, Phys. Rev. Lett. **77**, 1095 (1996).

20 M.C. Bartelt and J.W. Evans, Phys. Rev. Lett. **75**, 4250 (1995); Surf. Sci. **423**, 189 (1999).

21 C.L. Kelchner and A.E. DePristo, Surf. Sci. **393**, 72 (1997).

22 K. Bromann *et al.*, Phys. Rev. Lett. **75**, 677 (1995).

23 M. Schimschak and J. Krug, Phys. Rev. B **52**, 8550 (1995).

24 C.R. Stoldt *et al.*, Phys. Rev. Lett. **81**, 2950 (1998).

Figure Captions:

1. Differentiated STM images of 25 ML Ag films deposited on Ag(100) with F≈0.02ML/s as a function of substrate T: (a-h) 300 K, 280 K, 262 K, 230 K, 205 K, 190 K, 134 K, 54 K, resp.. All images are 100 nm x 100 nm. Error bars indicate only statistical uncertainty.
2. Properties of 25 ML Ag/Ag(100) films deposited at 300K and below: (a) interface width, W (solid circles); (b) characteristic lateral lengths: average mound separation, D_{av} (solid circles); average mound radius, R_{av} (solid squares). Solid curves guides the eye. Inset in 2b): typical form for $H(\mathbf{r})$ at 230K; arrows indicate the first maximum (R_{av}) and minimum (D_{av}).
3. MC simulation results for: (a) multilayer irreversible formation of square islands between 135 and 300K (solid circles fit with a smooth curve); experimental data as open squares; (b) RDF with low barrier hops up to 135 K (solid curve); experimental data as open squares.
4. Kinetic roughening at 230 K. (a)-(d) differentiated STM images of 5, 10, 25 and 100 ML Ag/Ag(100) films, respectively. All images are 75 nm x 75 nm.

Table I.

Variation with T of the local slope (in degrees) of 25ML Ag/Ag(100) film surfaces: (i) averaged over the entire surface (ϕ_{av}); (ii) over the "sides of mounds", defined as regions where the slope has a negative lateral curvature (ϕ_{md}); (iii) from $\tan^{-1}(W/R_c)$, where $H(R_c)=2W^2$ (ϕ_H). See Ref.10.

T	54K	135K	175K	230K	280K
ϕ_{av}	14.0	10.6	10.4	8.4	2.7
ϕ_{md}	16.0	12.0	12.2	9.6	3.2
ϕ_H	---	---	17.3	13.4	4.0

Table II.

Variation with θ of the interface width, W, the mound separation (D_{av}) in nm, and three measures of average local slope (cf. Table I) in degrees, for an Ag/Ag(100) film deposited at 230K.

θ	5ML	10ML	25ML	100ML
W	0.61	0.89	1.44	1.90
D_{av}	9.6	10.4	13.1	15.7
ϕ_{av}	3.7	5.7	8.2	11.2
ϕ_{md}	4.1	6.5	9.3	12.7
ϕ_{H}	8.3	10.8	13.4	15.1

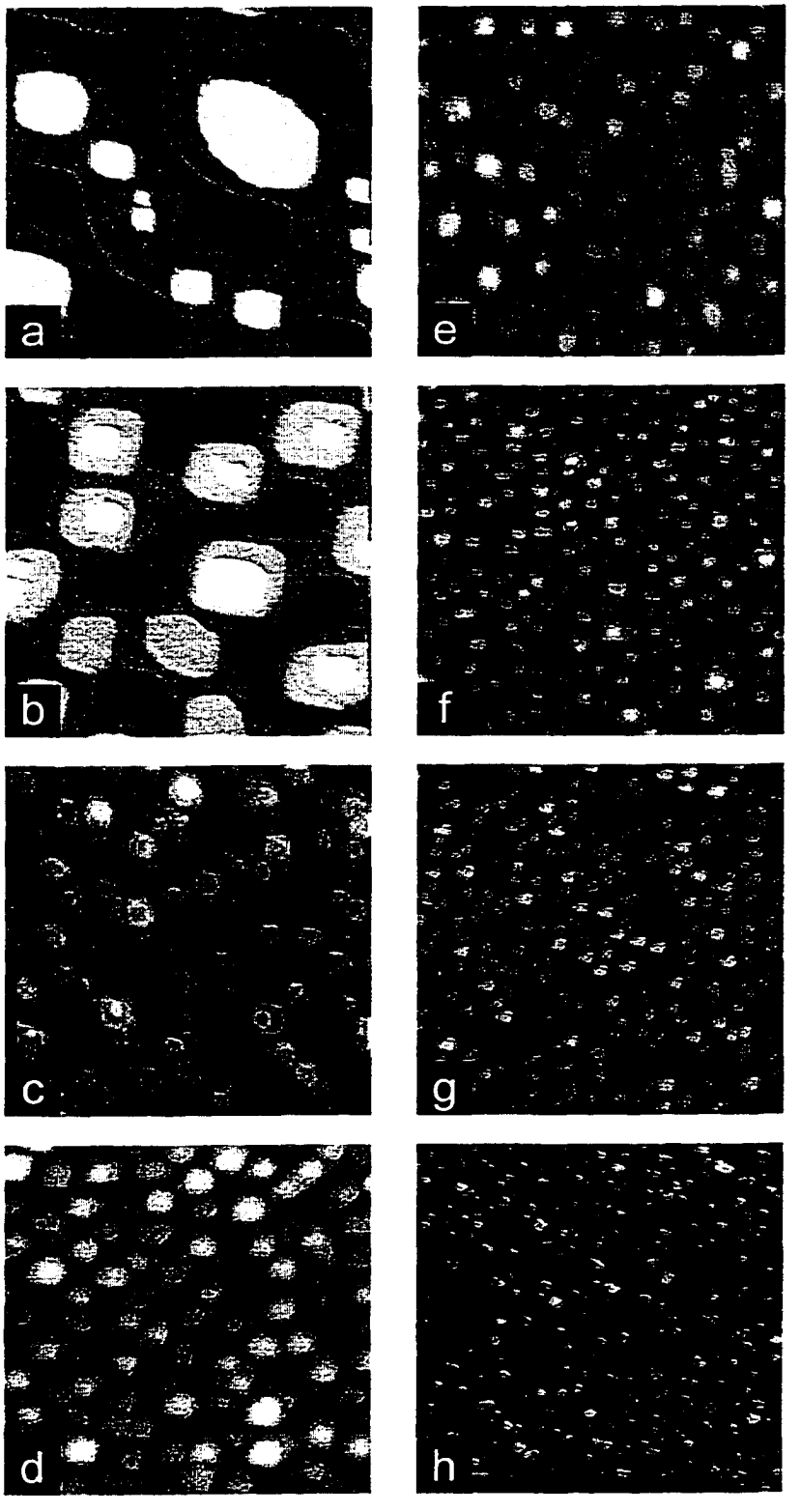

Figure 1

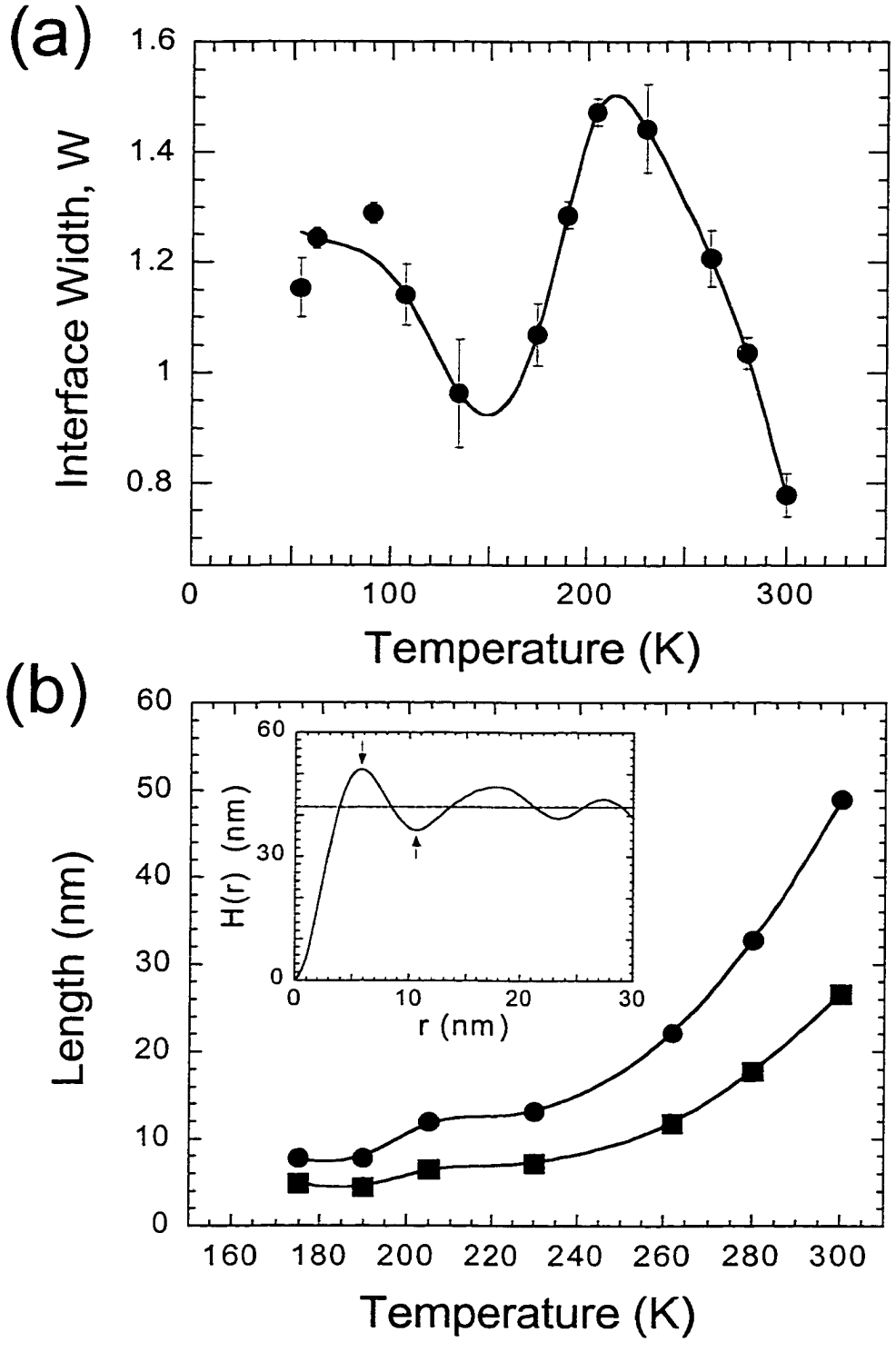
(a)
Interface Width, W
1.6
1.4
1.2
1
0.8
0
100
200
300
Temperature (K)
(b)
Length (nm)
60
50
40
30
20
10
0
160
180
200
220
240
260
280
300
Temperature (K)
H(r) (nm)
60
30
0
0
10
20
30
r (nm)

Figure 2

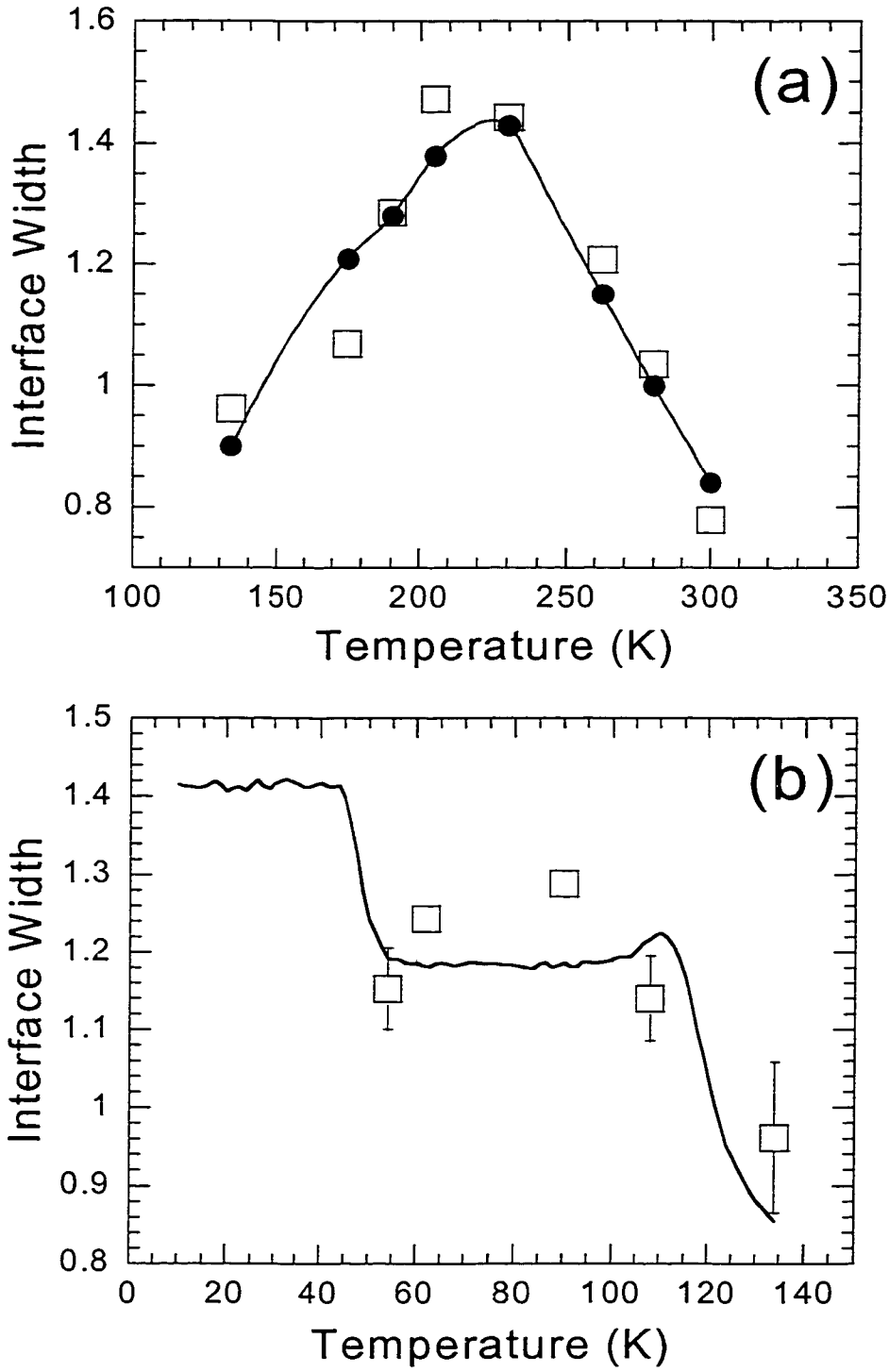
(a)
Interface Width
1.6
1.4
1.2
1
0.8
100
150
200
250
300
350
Temperature (K)
(b)
Interface Width
1.5
1.4
1.3
1.2
1.1
1
0.9
0.8
0
20
40
60
80
100
120
140
Temperature (K)

Figure 3

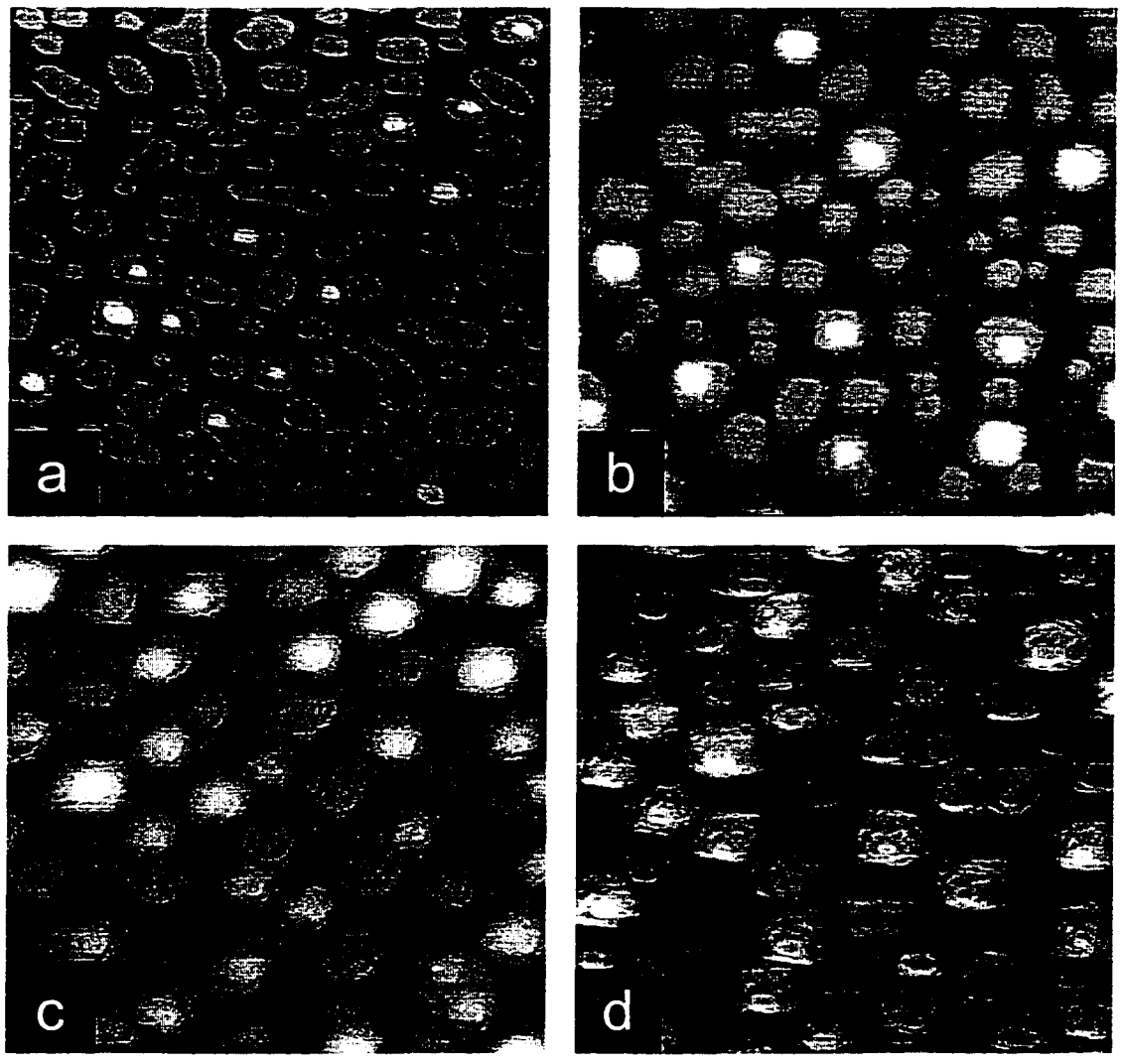

Figure 4

VI. GENERAL CONCLUSIONS

The application of a combination of Scanning Tunneling Microscopy (STM) experiments, together with mean-field rate equation and kinetic Monte Carlo (MC) simulations, leads to fundamental advances in our understanding of metal film growth processes, including the determination of key system parameters. The basic phenomena and concepts discussed in this dissertation will certainly apply more generally to metal(100) homoepitaxy, and will often be relevant for a variety of other thin-film systems. The main conclusions that can be drawn from this work are given below.

A comprehensive study of the coarsening of 2D Ag islands on Ag(100) has been performed at 295 K.

a) Experimental coarsening curves explicitly show that the island diffusion coefficient is size dependent for islands having between 40 and 530 atoms.
b) Simulations with an appropriate mean-field rate equation give reasonable agreement between theory and experiment.
c) The theory predicts a value of $\alpha = 1.5$, consistent with simple predictions of α if periphery diffusion is the dominant mechanism in island diffusion.
d) Monitoring coarsening kinetics with STM provides a new means of measuring the island diffusion coefficient.
e) Surface strain on the Ag(100) substrate significantly enhances island diffusion and coarsening rates.

STM experiments show important examples of nanostructure reshaping during Ag/Ag(100) homoepitaxy at 295 K.

a) Nanostructure reshaping occurs during all stages of film growth and equilibration.

b) The reshaping process is shown by STM to occur on times scales that are significant to the overall growth process.

c) MC simulations of a simple perimeter diffusion, nearest-neighbor interactions model captures relevant morphological details as seen with the STM.

d) Coalescence kinetics is modeled quantitatively, yielding an effective activation barrier for step edge restructuring of 0.75 eV.

Variable-temperature STM experiments reveal novel temperature dependence of morphology during the deposition of multilayer Ag films on Ag(100).

a) Doubly non-monotonic variation of roughness with deposition temperature is shown for 25 ML Ag films between 54 and 300 K.

b) Suitable models for metal(100) epitaxy accurately reproduce observed behavior and elucidate the atomistic processes and activation barriers controlling multilayer film structure.

c) Smaller lateral mound dimensions and increased steepness of mound sides are observed at lower T, consistent with theoretical predictions of multilayer film morphology.

d) At 230 K, roughness increases with a power-law dependence on film thickness, giving a growth exponent, $\beta \approx 0.32$.

APPENDIX I. ESTIMATION OF THE TERRACE DIFFUSION BARRIER FOR THE Ag ADATOM ON Ag(100)

In submonolayer and multilayer metal film growth, the activation barrier to terrace diffusion (E_d) plays a pivotal role in determining thin film characteristics. On a (100) surface, E_d is the barrier that a diffusing adatom must overcome when hopping from one four-fold hollow site to another. In submonolayer nucleation and growth, there are two competing processes which determine the time scale of growth: *deposition* and *diffusion* (1). The *deposition* rate, or flux (F), is the rate at which atoms impinge and adsorb onto the surface. Once the atoms adsorb, they begin to *diffuse* or hop at a rate (h) determined by the substrate temperature (T). If F is low, atoms will have a long period of time to diffuse, sampling many sites across the surface before encountering another deposited atom. Conversely, a high F will result in the deposition of atoms in the vicinity of diffusing atoms, enhancing the probability of island nucleation and reducing the overall diffusion time for adatoms. Due to the competition between *deposition* and *diffusion*, the ratio of h/F should impact all physical processes during thin film growth.

As noted in Chapter I, the average island density (N_{av}) for irreversible island formation (i = 1) is expressed as (2, 3)

$$N_{av} \sim \left(\frac{F}{\nu}\right)^{1/3} \exp\left[\beta \frac{E_d}{3}\right] \sim \left(\frac{h}{F}\right)^{-1/3}, \qquad [1]$$

where $\beta = (\kappa T)^{-1}$. The hopping rate (h) for an adatom is defined as

$$h = \nu \cdot \exp(-\beta \cdot E_d) \qquad [2]$$

using Arrhenius Law. In film growth, the deposited coverage, θ (in monolayers, ML), is determined by both the deposition F and deposition time (t), and is expressed as $\theta = Ft$. In order to assess the value of E_d, we choose to hold F constant. By doing so, N_{av} in equation 1 becomes a function of T only, allowing for the estimation of E_d from an Arrhenius plot. Figure 1 shows a series of STM images of submonolayer Ag island distributions on Ag(100) deposited at varying T (4). In these experiments, both F and θ are held constant, while T is decreased from 300 to 140 K. As T is decreased, N_{av} is seen to increase significantly, manifested in decreases in the island size and inter-island distance. A decrease in T results in a decrease in h, as seen in equation 2. By holding F fixed, the ratio of h/F decreases with decreasing T, causing an increase in N_{av}, as predicted by (1) and observed in Figure 1. An Arrhenius plot of N_{av} is given in Figure 2; the corresponding data is shown in Tables I and II. Using Arrhenius data from the range 180-300 K, one obtains

$$N_{av} \approx 4.58 \times 10^{-5} \exp\left[\beta \frac{E_d}{3}\right] \text{ nm}^{-2}$$

with $E_d \approx 0.37 \pm 0.XX$ eV. Instead, using only data from 200-300 K, one obtains

$$N_{av} \approx 2.43 \times 10^{-5} \exp\left[\beta \frac{E_d}{3}\right] \text{ nm}^{-2}$$

with $E_d \approx 0.42 \pm 0.XX$ eV. The latter choice is provoked by the possibility that classical scaling begins to break down below 200 K (5, 6), as discussed in Chapter V. These results are similar to E_d values estimated experimentally for Ag/Ag(100) using HRLEED (5) and LEIS (7), which give 0.38-0.42 and 0.40 eV, respectively.

References

1. A.-L. Barabasi, H. E. Stanley, *Fractal Concepts in Surface Growth* (University Press, Cambridge, ed. 1, 1995).

2. J. A. Venables, *Philosophical Magazine* 27, 697-738 (1973).

3. R. Kaishev, S. Stoyanov, *Izv. Otd. Khim. Nauki, Bulg. Akad. Nauk.* 2, 127-132 (1969).

4. C. R. Stoldt, S. Frank, J. W. Evans, P. A. Thiel, R. J. Behm, . (1997).

5. L. Bardotti, et al., *Physical Review B* 57, 12544-12549 (1998).

6. H.-J. Ernst, F. Fabre, J. Lapujoulade, *Physical Review B* 46, 1929-1932 (1992).

7. M. H. Langelaar, D. O. Boerma, in *Surface Diffusion: Atomistic and Collective Processes* M. C. Tringides, Ed. (Plenum Press, New York, 1997), vol. 360, pp. 67-74.

Table Captions

I. Arrhenius data for submonolayer Ag island distributions on Ag(100) acquired between 125 and 180 K using low-temperature Scanning Tunneling Microscopy at the University of Ulm, Germany.

II. Arrhenius data for submonolayer Ag island distributions on Ag(100) acquired between 200 and 300 K.

Figure Captions

1. A series of STM images showing the temperature dependence of the average initial island density for 0.10 ML of Ag deposited on Ag(100). The flux is 0.006 ML/s. All images are 250 x 250 Å.

2. Arrhenius behavior of the average initial island density, N_{av}. The solid line is a linear fit to data between 180 and 300 K producing $E_d \approx 0.37$ eV. The dashed line is a linear fit to data between 200 and 300 K producing $E_d \approx 0.42$ eV.

T (K)	# of islands/image	image area (nm^2)	total # of islands	total area (nm^2)	N_{av} (nm^{-2})
125	86	260.61			
125	400	903			
125	74	134.79			
125	52	110.64			
125	82	216			
			694	1625.04	0.427066411
140	252	1856			
140	241	1575			
			493	3431	0.143689886
150	204	1162.06			
150	72	504.89			
150	160	961.7			
150	119	749.33			
150	125	729.29			
150	106	769.36			
150	166	1175.42			
			952	6052.05	0.157302071
165	216	1984			
165	71	602			
165	95	918			
165	137	1400			
165	110	1054			
165	205	1800			
165	85	850			
165	398	3444			
165	123	1338.75			
165	224	2100			
165	232	2303			
165	381	4004			
			2277	21797.75	0.104460323
180	345	3060			
180	409	4200			
180	99	756			
180	223	1568			
180	158	1312			
180	191	1344			
			1425	12240	0.116421569

Table I

T (K)	# of islands/image	image area (nm^2)	total # of islands	total area (nm^2)	N_{av} (nm^{-2})
200	252	4725			
200	207	3629.5			
200	376	6354.4			
200	112	1861.9			
200	60	940.33			
200	100	1542.73			
200	180	2613			
200	66	1135.35			
200	141	2220			
200	206	3412.11			
200	175	2697.3			
200	155	2646			
			2030	33777.62	0.060098965
225	57	1450			
225	109	2537			
225	71	1600			
225	120	2604			
225	198	4556			
225	91	2067			
225	75	1650			
225	132	2800			
225	77	1856			
			930	21120	0.044034091
250	75	4366			
250	64	3388			
250	42	2278			
250	48	2590			
250	53	3330			
250	57	2998.8			
250	37	2100			
			376	21050.8	0.017861554
284	24	4178.07			
284	20	3006.25			
284	33	5210.57			
284	19	2973.05			
284	8	1266.32			
			104	16634.26	0.006252157
300	85	17311			
			85	17311	0.004910173

Table II

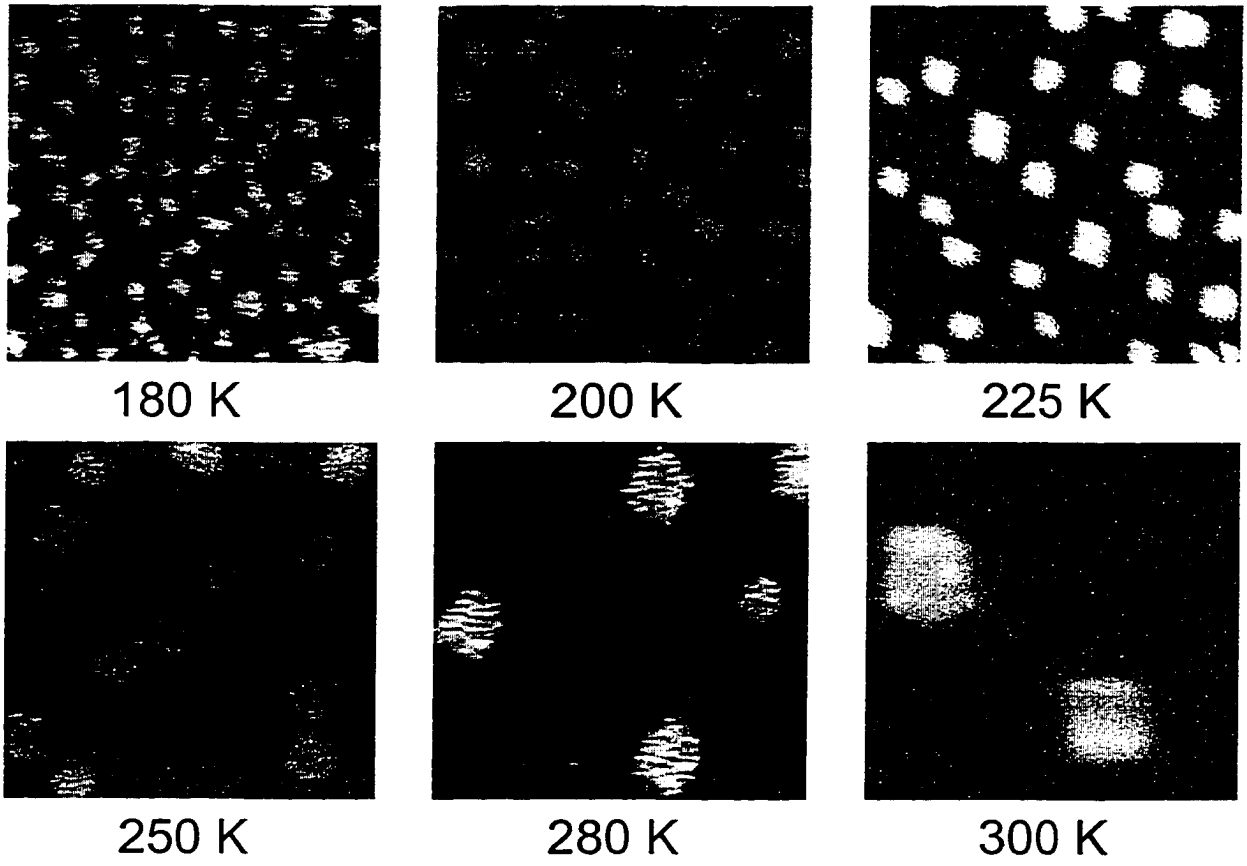

Figure 1

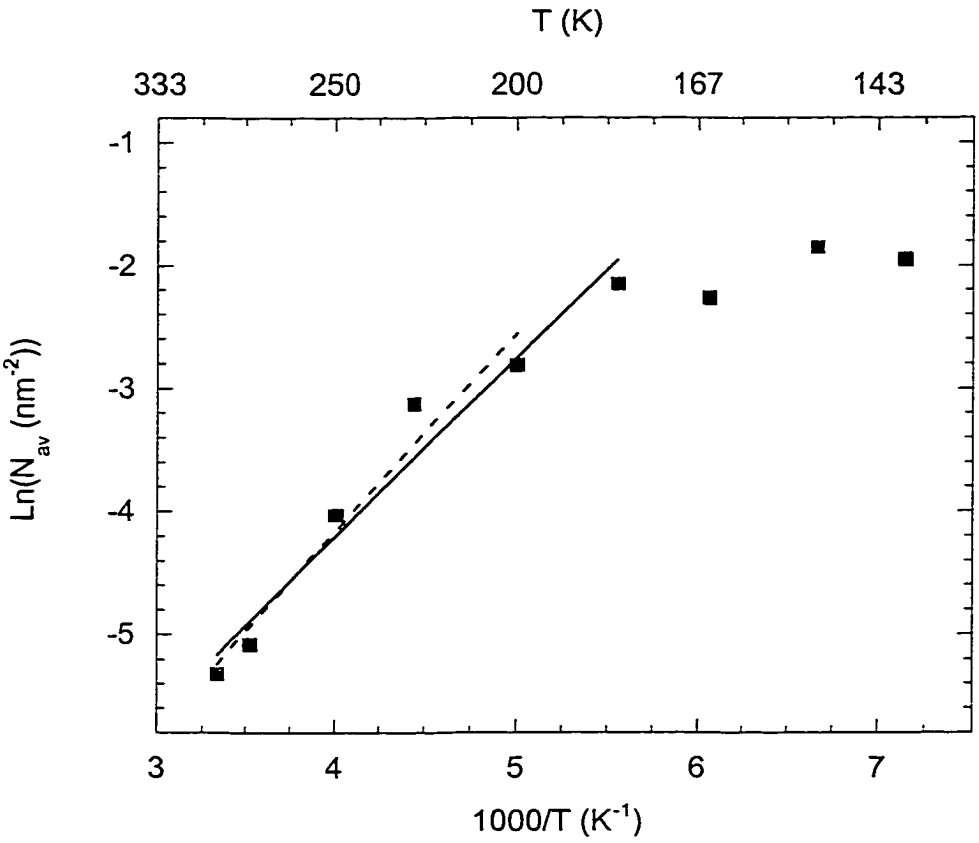

Figure 2

APPENDIX II. ESTIMATION OF THE ROUGHNESS EXPONENT FROM STM IMAGES

A surface is termed self-affine if the interface width, W, increases with the horizontal length, L, according to $W \propto L^{\alpha}$, where the roughness exponent $0 < \alpha < 1$ is indicative of the texture of the surface (1). Specifically, α is a parameter that reflects the degree of height-height correlation at the interface. Small values of α are associated with uncorrelated, jagged surfaces, while large values are associated with well-correlated surfaces (2). In Chapter V, we showed that 25 ML Ag films deposited on Ag(100) display a characteristic length scale D_{av}, which is determined from a height-height correlation function, H(**r**). A well-defined D_{av} is the result of diffusion processes on the surface. Deposited atoms travel across the surface, searching for the most energetically favorable location to bond. This 'selectivity' in surface bonding results in correlated surface features, such as in the mounding regime for Ag/Ag(100). Between 190 and 230 K, where mounds form with a well-defined D_{av}, one would expect these surfaces to yield $\alpha \approx 1$. At very low deposition temperatures where thermally activated diffusion is inoperative, one would expect α to deviate substantially from a value of 1.

In Fig. 1(a-h), log-log plots of W as a function of STM image length, L are shown for 25 ML Ag films deposited between 54 and 230 K, where mounds are observed to form. A power-law fit to the data up to the saturation of W (W_{sat}) gives the roughness exponent α, using $W \propto L^{\alpha}$. This technique for determining α is fully described in Appendix A of reference 3. This method is particularly useful for the Ag/Ag(100) system since D_{av} is very

small, less than 20 nm for temperatures below 250 K. Therefore, the length scale prior to W_{sat} is well within the scanning capabilities of the STM. Studies of Ag/Ag(111) at 298 K, on the other hand, could not reach W_{sat} due to the limited scanning range of their STM (4). Between 175 and 230 K, a power-law fit of the experimental data yields $\alpha \approx 1$, which is consistent with results from $H(\mathbf{r})$ and theoretical results which predict that diffusion is active on the surface. Below 135 K, α decreases to approximately 0.5, consistent with theoretical predictions that thermally activated diffusion becomes severely inhibited or inoperative, resulting in self-affine film growth.

We also use this method to estimate α for 25-300 ML Ag films deposited on Ag(100) at 230 K, shown in Figures 8-10. At 25 and 100 ML, α is approximately 1, indicating non-self-affine growth and correlated mound formation. At 300 ML, $\alpha \sim 0.5$, a surprising indication of self-affine growth with larger film thicknesses. Currently, we do not know the origin of this deviation from correlated film growth.

References

1. B. B. Mandelbrot, *The fractal geometry of nature* (W.H. Freeman, New York, ed. 2, 1983).

2. R. Chiarello, V. Panella, J. Krim, C. Thompson, *Physical Review Letters* **67**, 3408-3411 (1991).

3. A.-L. Barabasi, H. E. Stanley, *Fractal Concepts in Surface Growth* (University Press, Cambridge, ed. 1, 1995).

4. I. Heyvaert, J. Krim, C. Van Haesendonck, Y. Bruynseraede, *Physical Review E* **54**, 349-353 (1996).

Figure Captions

1. $Log_{10}(W)$ vs. $log_{10}(L)$ plots for the growth of 25 ML Ag films deposited on Ag(100) at: (a) 230 K, $\alpha \approx 1.07$; (b) 205 K, $\alpha \approx 1.08$; (c) 190 K, $\alpha \approx 0.98$; (d) 175 K, $\alpha \approx 1.05$; (e) 135 K, $\alpha \approx 0.93$; (f) 107 K, $\alpha \approx 0.57$; (g) 62 K, $\alpha \approx 0.55$; and (h) 54 K, $\alpha \approx 0.50$. L is the STM scan length in nm and W is the interface width in nm. The values of the roughness exponent, α, are determined from a power-law fit restricted to the observed linear regime.
2. $Log_{10}(W)$ vs. $log_{10}(L)$ plots for the growth of varying Ag film thicknesses on Ag(100) at 230 K: (a) 25 ML, , $\alpha \approx 1.07$; (b) 100 ML, $\alpha \approx 0.99$; (c) 300 ML, $\alpha \approx 0.54$. L is the STM scan length in nm and W is the interface width in nm. The values of the roughness exponent, α, are determined from a power-law fit restricted to the observed linear regime.

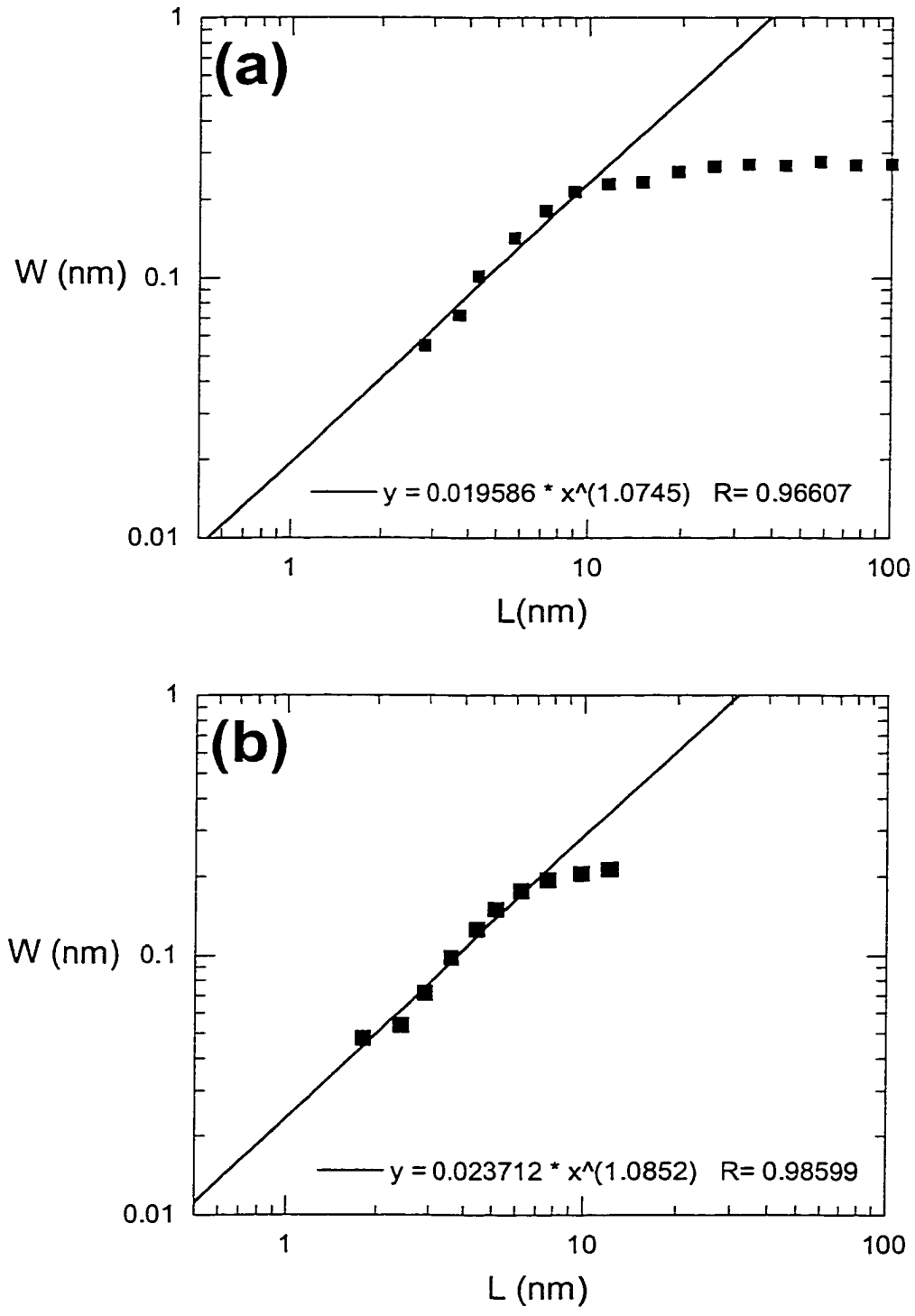
(a)
W (nm)
1
0.1
0.01
y = 0.019586 * x^(1.0745) R= 0.96607
1
10
100
L(nm)
(b)
W (nm)
1
0.1
0.01
y = 0.023712 * x^(1.0852) R= 0.98599
1
10
100
L (nm)

Figure 1

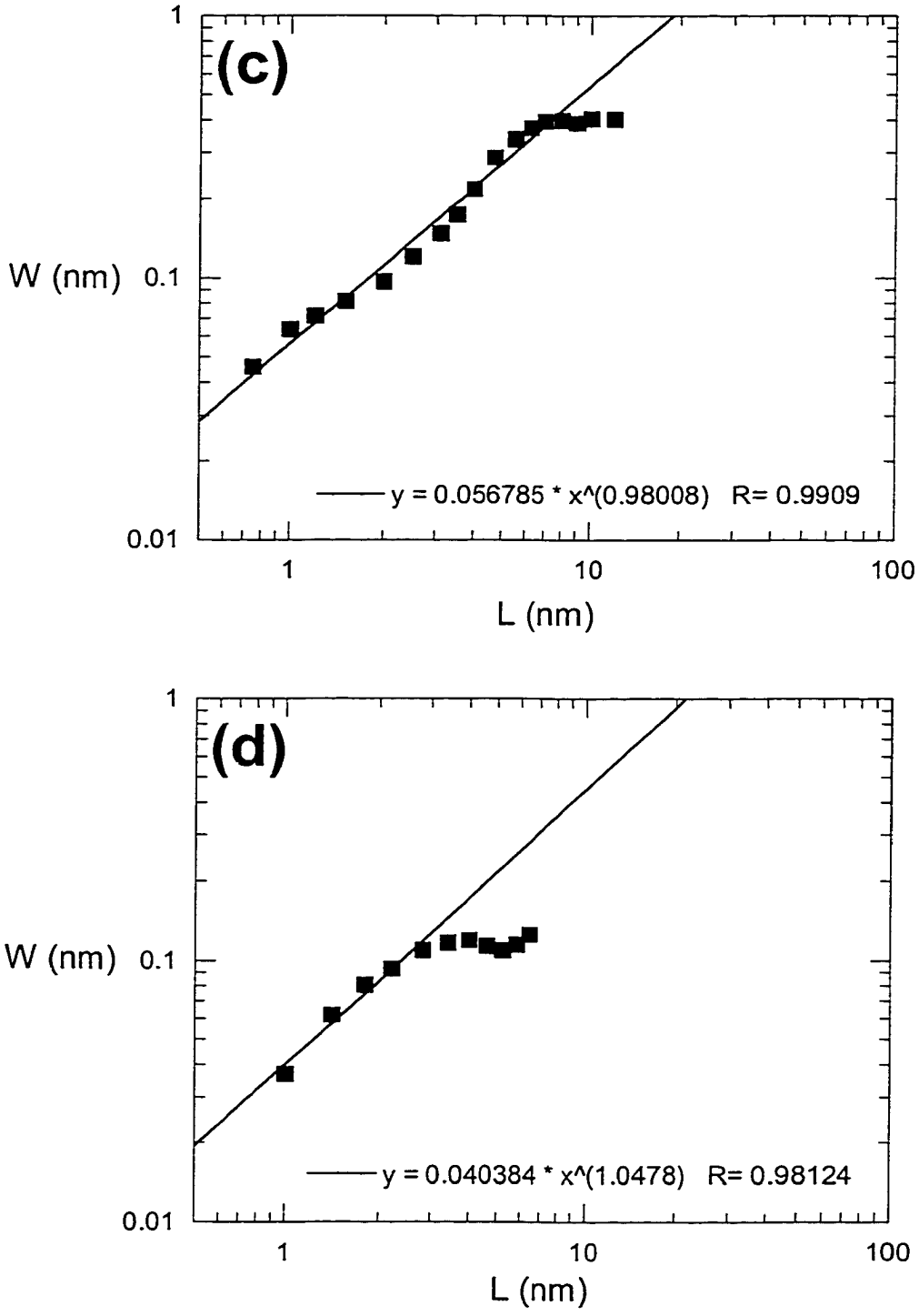
(c)
W (nm)
1
0.1
0.01
1
10
100
L (nm)
y = 0.056785 * x^(0.98008) R= 0.9909
(d)
W (nm)
1
0.1
0.01
1
10
100
L (nm)
y = 0.040384 * x^(1.0478) R= 0.98124

Figure 1

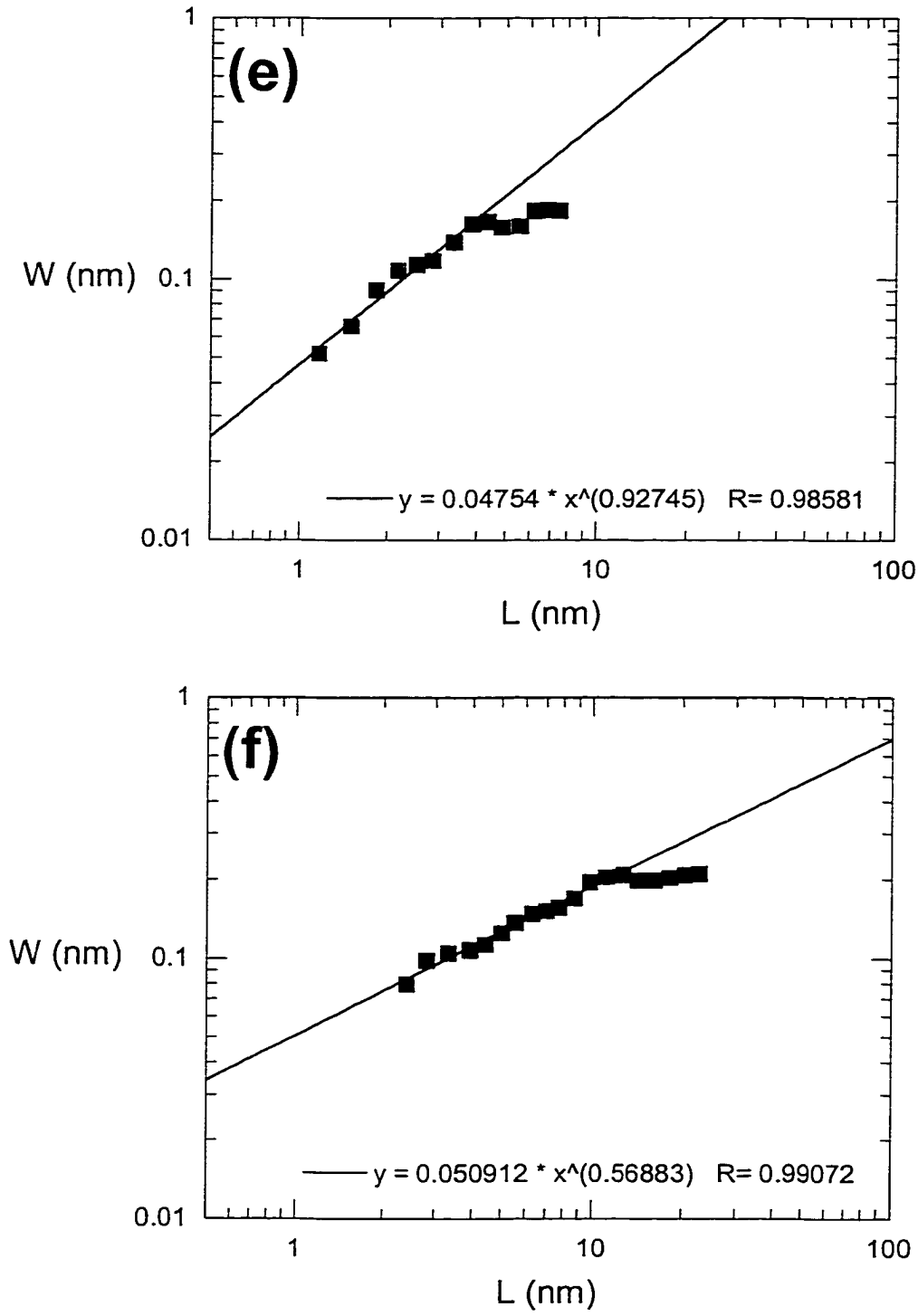
(e)
W (nm)
1
0.1
0.01
1
10
100
L (nm)
y = 0.04754 * x^(0.92745) R= 0.98581
(f)
W (nm)
1
0.1
0.01
1
10
100
L (nm)
y = 0.050912 * x^(0.56883) R= 0.99072

Figure 1

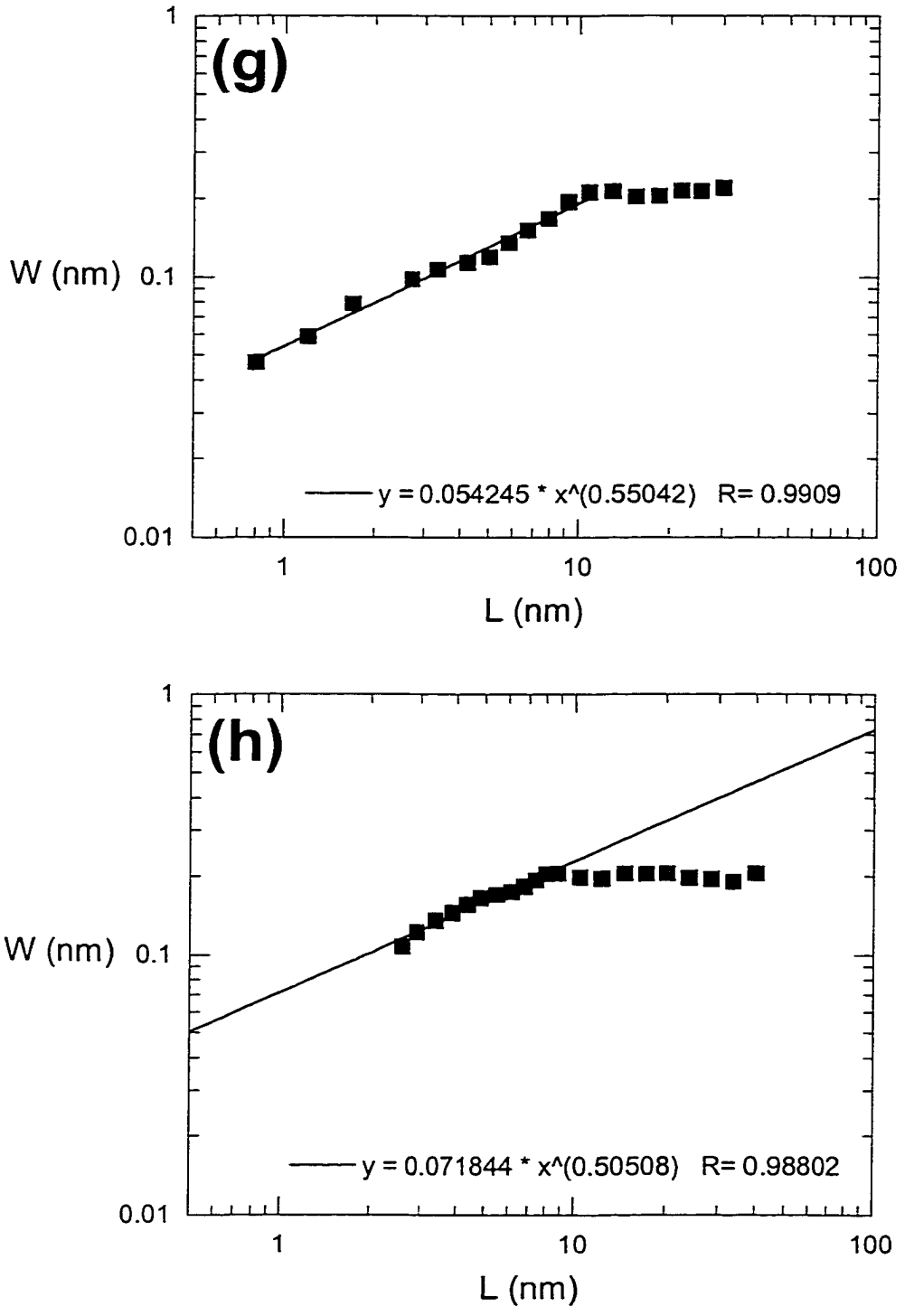
(g)
W (nm)
1
0.1
0.01
y = 0.054245 * x^(0.55042) R= 0.9909
1
10
100
L (nm)
(h)
W (nm)
1
0.1
0.01
y = 0.071844 * x^(0.50508) R= 0.98802
1
10
100
L (nm)

Figure 1

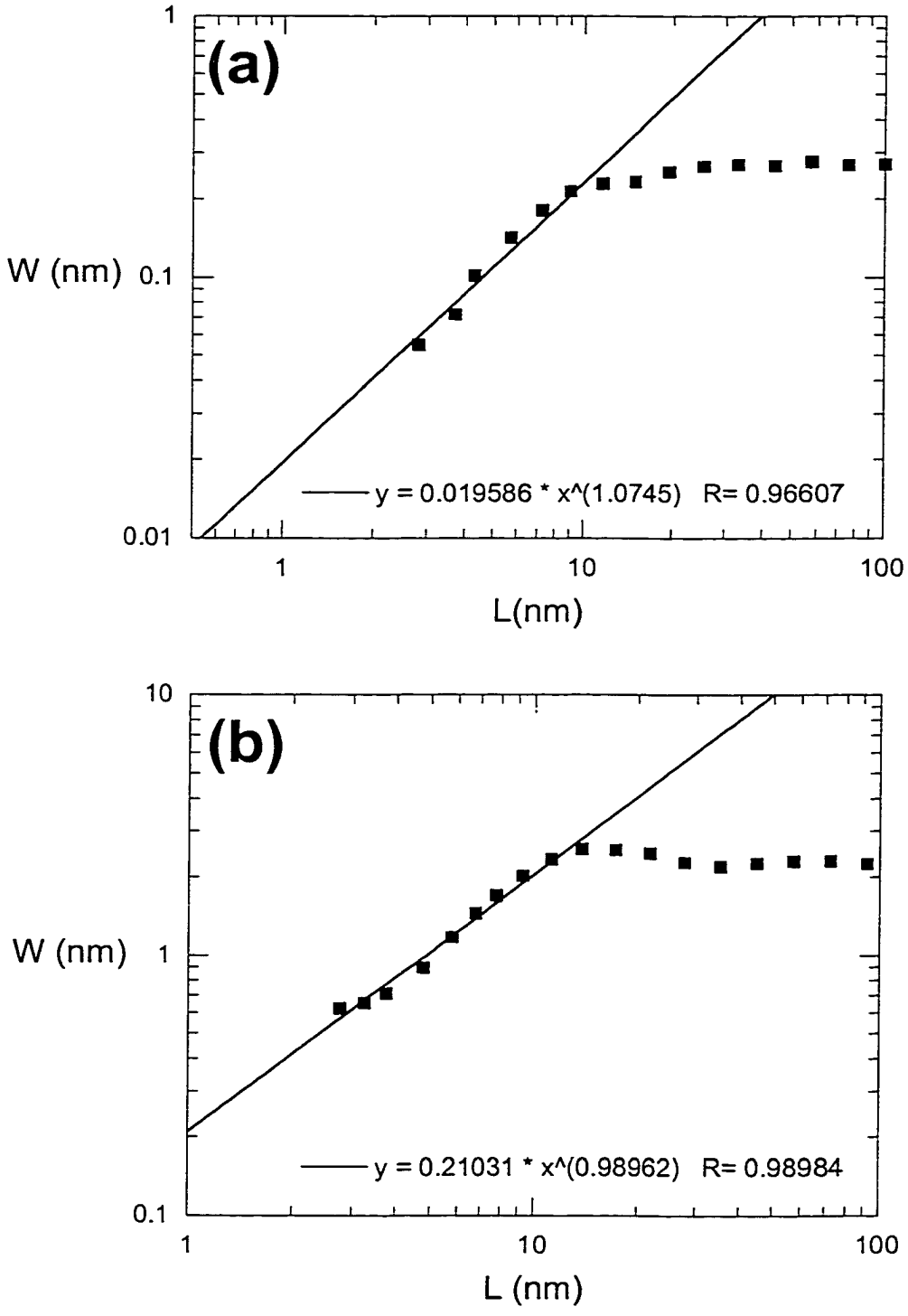
(a)
W (nm)
1
0.1
0.01
y = 0.019586 * x^(1.0745) R= 0.96607
1
10
100
L(nm)
(b)
W (nm)
10
1
0.1
y = 0.21031 * x^(0.98962) R= 0.98984
1
10
100
L (nm)

Figure 2

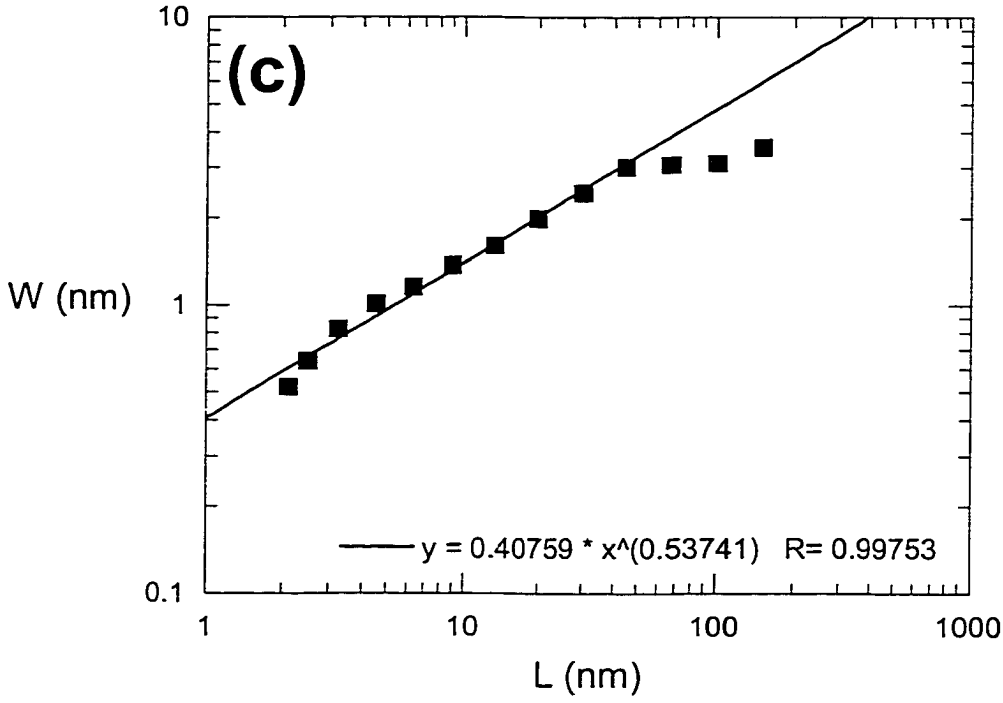

Figure 2

APPENDIX III. ESTIMATION OF MOUND DENSITIES IN MULTILAYER Ag/Ag(100) HOMOEPITAXY

Table Caption

I. (a) Mound densities for 25 ML Ag films deposited on Ag(100) determined using the height-height correlation function, H(**r**), described in Chapter V. (b) Densities estimated by hand counting individual mounds between 230 and 205 K, where mounds are easily distinguished with the eye.

(a)

T (K)	D_{av} (nm)	total # mounds	total area (nm^2)	N (nm^{-2})
230	8.877	385	30336	1.269E-02
225	7.604	683	39493	1.729E-02
205	8.351	545	38009	1.434E-02
190	4.742	896	20148	4.447E-02
175	4.766	896	7291	4.403E-02
134	4.506	1122	22778	4.926E-02
107	3.940	824	12790	6.442E-02

(b)

T (K)	total # mounds	total area (nm^2)	N (nm^{-2})	D_{av} (nm)
230	155	20883	7.422E-03	11.607
225	475	64132	7.407E-03	11.620
205	622	60398	1.030E-02	9.854
190				
175				
134				
107				

Table I

APPENDIX IV. THE VTSTM UHV CHAMBER

1. The vacuum chamber itself

I finished constructing the new ultra-high vacuum (UHV) chamber built to house the Omicron Variable-Temperature Scanning Tunneling Microscope (VTSTM) during the 1998 Fall semester. The completed vacuum chamber was then used for the multilayer growth studies described in Chapter V. This vacuum chamber is horizontally configured (see Figure 1), a design I first encountered when performing experiments in Professor R. J. Behm's group at the University of Ulm in Germany. This design allows for easy sample manipulation, translation, and transfer within the vacuum chamber. I also found it important to design the chamber with the most massive instruments (ie, ion pump, manual gate valve) as close to the floor as possible. This lowers the vacuum chamber's overall center of mass, resulting in greater stability and reduced vibrations caused by a "top heavy" chamber supported on air legs. By designing the vacuum chamber low to the ground, the experimenter also has easy access to all chamber ports and the wobble stick/screwdriver on the VTSTM. Finally, the atmosphere-vacuum sample transfer system (load lock) is designed to position the sample or STM tip near the VTSTM chamber. The experimenter can directly grasp the sample or STM tip with the VTSTM wobble stick, thereby avoiding both transfer first to the manipulator and excessive manipulation once in vacuum. This greatly expedites atmosphere-vacuum transfers and reduces the risk of dropping the sample or STM tip in the vacuum chamber. See Figures 2 and 3 for detailed dimensions of the sample prep chamber.

The VTSTM UHV chamber features:

a) Omicron model 25 RH VTSTM with a scanning temperature range of 25-750 K

b) Thermionics XYZ manipulator with 10" of Z travel and 1" of X-Y travel

c) Omicron EFM 3 thin film evaporator, 5-20 mm^2 deposition area

d) Varian 400 L/s ion pump

e) Pfeiffer-Balzers 170 L/s turbo pump (main), 53 L/s turbo pump (load lock)

f) PHI model 10-180 LEED-Auger electron optics system

g) Dycor LC-series residual gas analyzer, 1-100 amu range

h) PHI model 04-161 sputter ion gun

i) Kinetic Systems 36" tall vibration isolation table legs

j) atmosphere-vacuum sample transfer system (load lock)

k) home-built gas handling line

DO NOT attempt to use the VTSTM UHV chamber (1) before being trained by an *experienced* Thiel group member and (2) before reading the Standard Operating Procedures (SOP) for the VTSTM UHV chamber in 331 Spedding Hall.

2. The Omicron VTSTM

Before operating the VTSTM, one must read *all* supporting documentation provided by Omicron. This includes "The Variable Temperature STM User's Guide" and "The SPM SO V2.2 Software Manual." Furthermore, one should only attempt to operate the VTSTM after being trained by an *experienced* Thiel group member or Omicron technician.

Figure Captions

1. Side view of the VTSTM UHV chamber showing analytical instruments and structural components. (Not drawn to scale)
2. Side view of the sample prep chamber showing key structural dimensions. (Scale: 1"=2")
3. Sample prep chamber viewed from the VTSTM flange showing rotational clearance of the Omicron sample holder affixed to the XYZ manipulator. (Scale: 1"=2") Prep chamber flange sizes: (a) 2.75" and (b) 6".

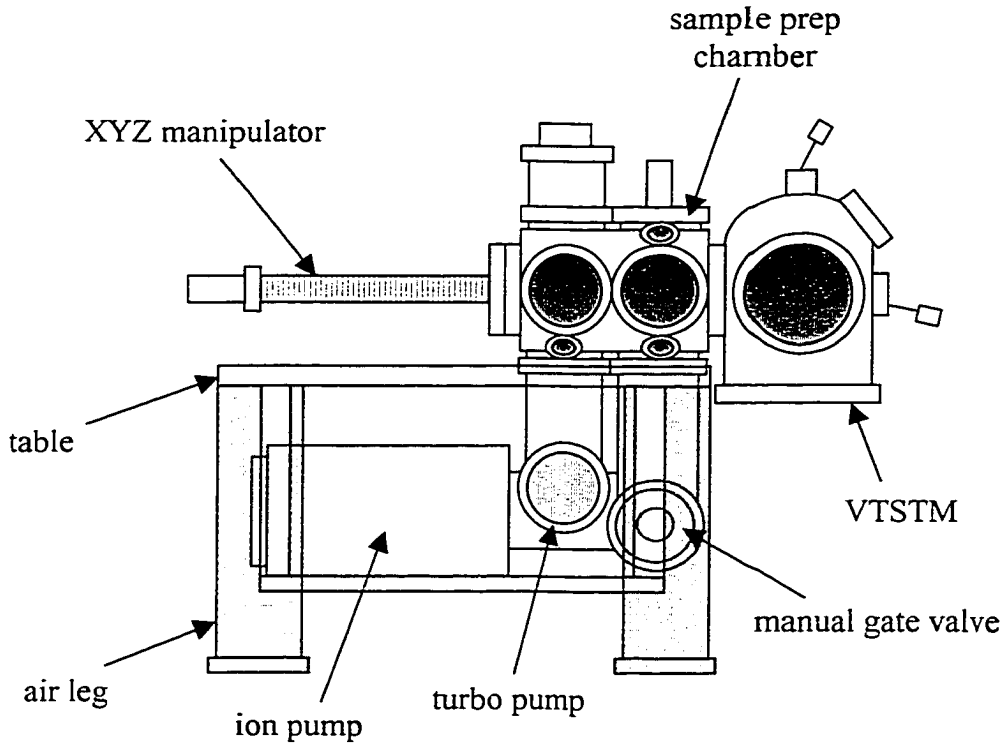
sample prep
chamber
XYZ manipulator
table
VTSTM
manual gate valve
air leg
ion pump
turbo pump

Figure 1

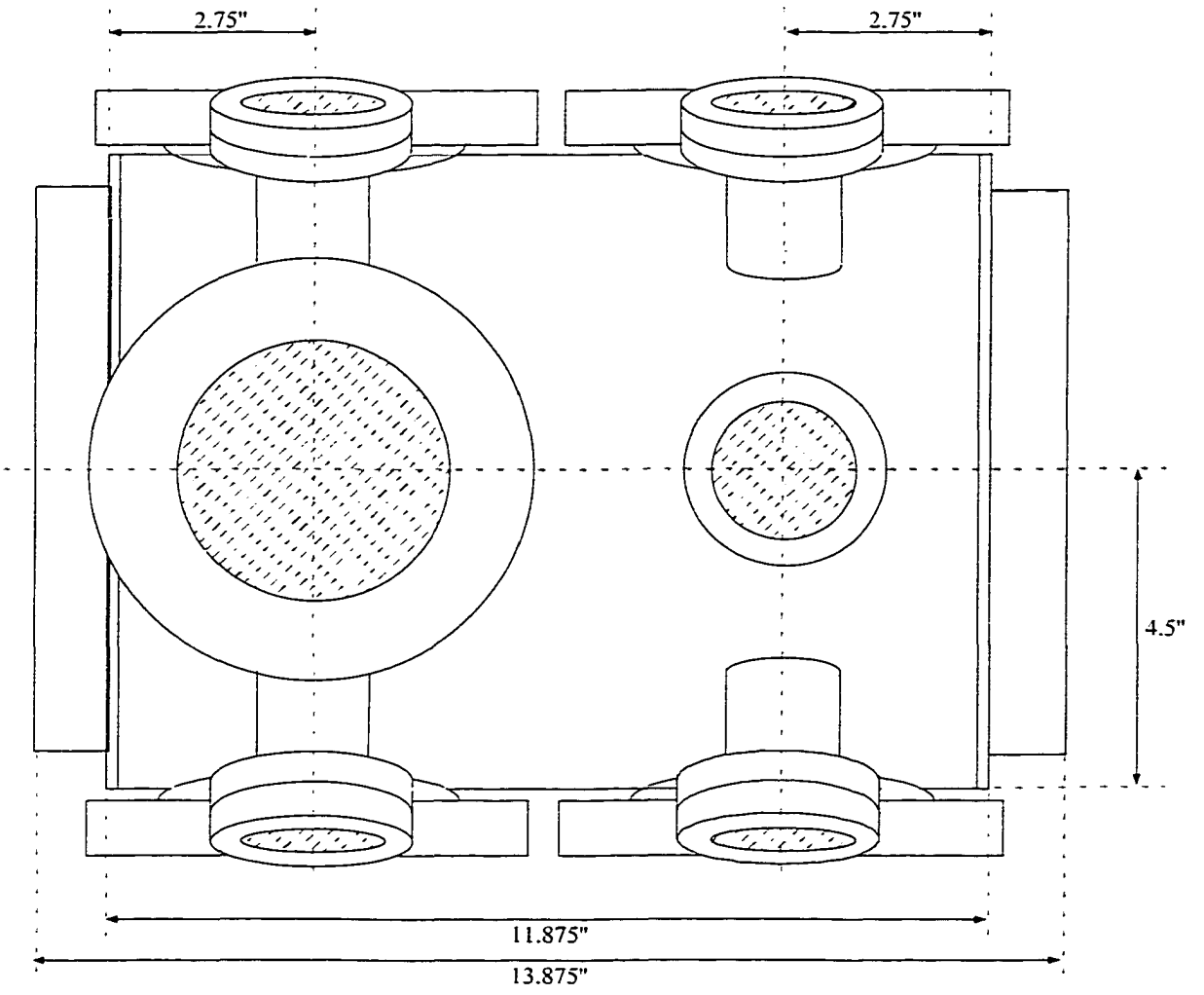

Figure 2

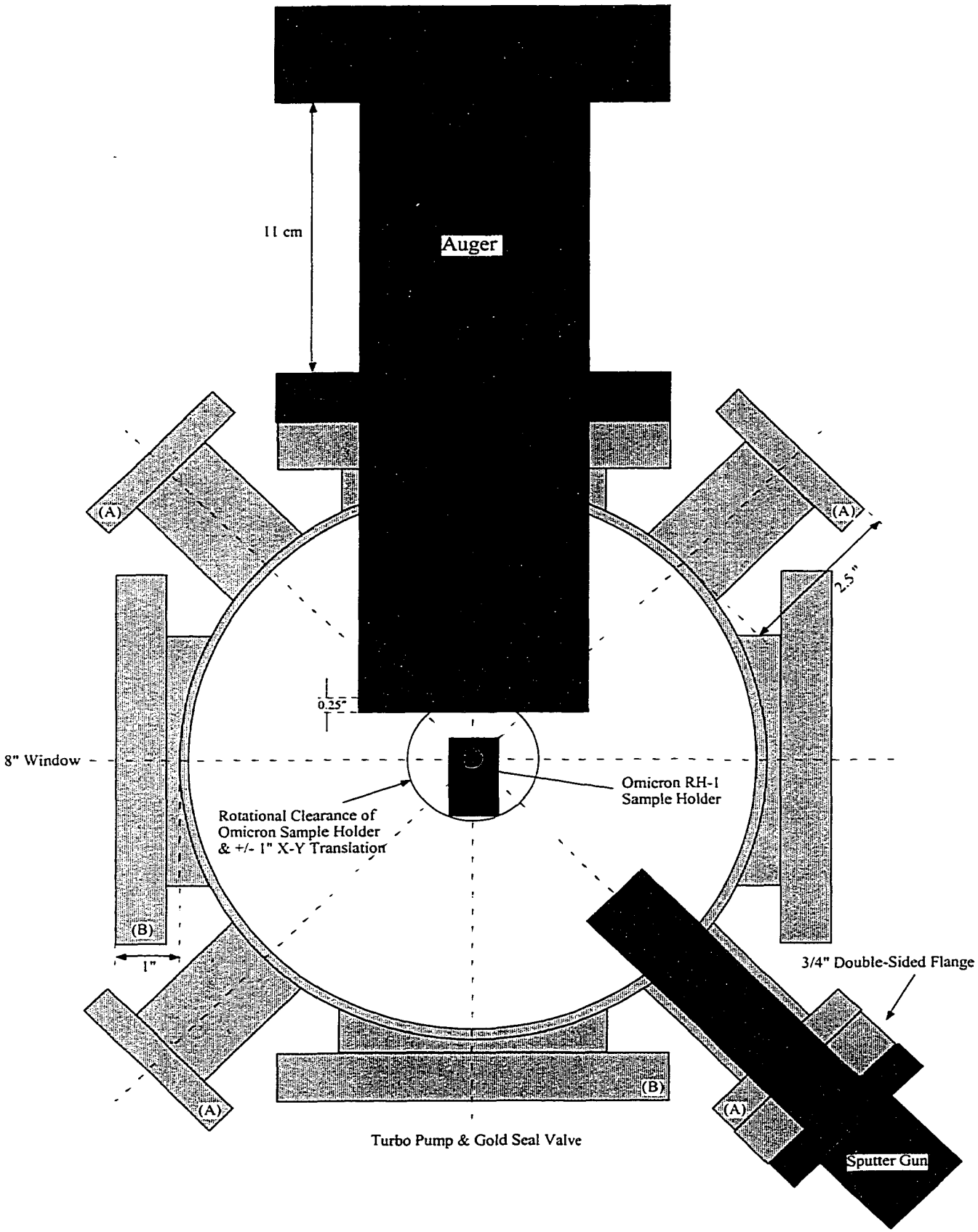
11 cm
Auger
(A)
(A)
2.5"
0.25"
8" Window
Omicron RH-1
Sample Holder
Rotational Clearance of
Omicron Sample Holder
& +/- 1" X-Y Translation
(B)
1"
3/4" Double-Sided Flange
(B)
(A)
(A)
Turbo Pump & Gold Seal Valve
Sputter Gun

Figure 3

APPENDIX V. STM DATABASE

Table Captions

I. STM database of Ag/Ag(100) coarsening experiments.

II. STM database of Ag/Ag(100) coalescence experiments. Columns denoted with a X indicate that an example of: corner to corner island coalescence (C-C), side to side island coalescence (S-S), island coalescence with a [001] step edge ([001]), island coalescence with a [011] step edge ([011]) is present within the particular file of experimental images.

III. VTSTM database of multilayer Ag/Ag(100) experiments.

File Name	Flux (ML/s)	Coverage (ML)	$N_0 \times 10^{-5}$ ($Å^{-2}$)	S_{av} (atoms/island)	* Time/image #	Experiment Notes
01.08.98	0.0036	0.200	7.4	600	21/1	two separate terraces
01.10.98	0.0039	0.110	5.4	244	87/7	
01.22.98	0.0039	0.100	6.4	187	30/1	only 4 images
02.26.98	0.0007	0.040	2.5	190	35/1	Sav too small
02.28.98	0.0009	0.055			46/1	
03.01.98	0.0005	0.080			72/7	bad tip
03.02.98	0.0014	0.080			39/2	Sav too small
04.16.98	0.0100	0.250	5.5	550	15/25	
04.18.98	0.0110	0.140	8.1	205	23/2	Fig. 2(a) in J.Chem.Phys.
04.19.98	0.0110	0.040	7.3	65	21/1	Fig. 2(a) in J.Chem.Phys.
04.20.98	0.0110	0.250	5.7	530	31/3	Fig. 2(a) in J.Chem.Phys.
04.29.98	0.0060	0.050	5.2	115	27/1	Fig. 2(b) in J.Chem.Phys.
04.30.98	0.0060	0.120	5.4	300	45/1	Fig. 2(b) in J.Chem.Phys.
05.01.98	0.0060	0.200		500	34/3	strange results
05.02.98	0.0060	0.210	4.9	510	25/1	Fig. 2(b) in J.Chem.Phys.
05.03.98	0.0050	0.160	4.9	440	51/2	small strained region
05.06.98	0.0120	0.047	5.9	95	18/2	tip changed island density
05.08.98	0.0030	0.010	3.1	40	28/2	Fig. 2(c) in J.Chem.Phys.
05.18.98	0.0030	0.050	4.2	140	48/3	Fig. 2(c) in J.Chem.Phys.
05.19.98	0.0030	0.080	3.5	270	19/1	Fig. 2(c) in J.Chem.Phys.
05.20.98	0.0030	0.020	4.0	60	42/3	Fig. 2(c) in J.Chem.Phys.
05.22.98	0.0030	0.180	4.4	490	36/5	strained, Fig. 7, 8 in J.Chem.Phys.

* Denotes time in min. between deposition and the first STM image in series and the corresponding image #.

Table I

File Name	Flux (ML/s)	Coverage (ML)	C-C	S-S	[001]	[011]	Experiment Notes
12.08.97	0.0029	0.29	X	X	X		good data set
12.09.97	0.0032	0.32		X		X	only 3 examples
12.11.97	0.004	0.36	X		X		
12.13.97	0.004	0.85	X	X	X	X	vacancy examples including worms
12.16.97	0.004	0.3	X				
06.08.98	0.0097	0.69					good broad view vacancy images
06.22.98	0.035	0.35				X	two cluster-[011] step edge examples

Table II

File Name	Deposition Temp (K):	Flux (ML/s):	Coverage (ML):
08.13.99	350	0.029	25
07.21.99	320	0.029	25
04.14.99	300	0.014	25
04.16.99	280	0.018	25
03.30.99	262	0.018	25
03.25.99	225	0.018	25
05.17.99	230	0.035	25
03.31.99	205	0.018	25
04.18.99	190	0.018	25
04.15.99	189	0.014	25
03.28.99	175	0.018	25
03.26.99	134	0.018	25
06.08.99	135	0.018	25
08.09.99	107	0.029	25
05.21.99	90	0.035	25
07.22.99	62	0.029	25
05.19.99	54	0.035	25
05.20.99	54	0.035	25
08.31.99	230	0.032	5
03.24.99	230	0.018	10
09.20.99	230	0.032	10
08.17.99	230	0.032	100
10.04.99	230	0.032	300
04.20.99	190	0.018	10
03.22.99	135	0.018	10
03.21.99	300	0.018	10
03.22.99	135	0.018	20
03.21.99	300	0.018	20

Table III

ACKNOWLEDGEMENTS

I would like to express my sincere appreciation to Professors Pat Thiel and Jim Evans for their support, guidance, and encouragement throughout my graduate study and during Iowa's long winters. I must also thank them for the opportunity to study in Germany, where I gained invaluable experience, as well as spent my birthday in München at Oktoberfest.

My thanks also go out to everyone, past and present, in the Thiel and Evans research groups, including but not limited to Dr. Cynthia Jenks, Tony Layson (my bald friend), Kyle Caspersen, Dr. Antonio Cadilhe, Dr. Maria Bartelt, Dr. Laurent Bardotti (wherever you are), and Dr. Zhouxin Shen (the goldenboy).

My gratitude to Stefan Frank, Martin Ruff, and Professor R.J. Behm at the University of Ulm in Germany, who played a vital role in starting my career as an experimentalist in UHV.

I thank Jim Anderegg for his technical assistance and intriguing conversations over coffee. And how can I forget Charlie Burg, welder and cranky old man, who gave me hell every time I needed to have a leak fixed. The work of these two men is second to none.

Last but not least, I want to thank everyone who played a part in my life while in Ames. Andrew, for suffering right along with me through this ordeal. AJ, for giving pet names to all the People's waitresses. Dale, for the numerous nights of Canadian style drinking. Jamie, for making my final year in Ames very special. And finally, to my family and friends elsewhere in North America, I love you all.